Computational Chemistry Studies of Organometallic Energy Landscapes

By

Ian M. Pendleton

A dissertation submitted in partial fulfillment
of the requirements for the degree of
Doctor of Philosophy
(Chemistry)
in the University of Michigan
2018

Doctoral Committee:

Professor Melanie Sanford, Co-Chair
Assistant Professor Paul Zimmerman, Co-Chair
Professor Charles Brooks III
Professor Suljo Linic
Associate Professor Pavel Nagorny

Ian M. Pendleton

ipendlet@umich.edu

ORCID iD: 0000-0002-4394-3223

To my mentors, past and present. Thank you.

Acknowledgements

I would like to first express gratitude to my graduate school mentors, Paul Zimmerman and Melanie Sanford. Paul took the time to explain chemistry, computer science, pedagogy and philosophy (now my favorite hobby). Those conversations were highly meaningful and thought provoking. For that, I will be eternally grateful for his guidance during this part of my career. Melanie was one of the most honest, witty, and intelligent people I have ever had the pleasure of working with. I hope to bring her level of focus and poise to handling challenging problems in the future. I would also like to thank my committee members for reading my dissertation and taking the time to offer helpful feedback.

I feel that I was truly one of the luckiest people in the chemistry program. I had the privilege of meeting and discussing chemistry with two unique groups of highly talented individuals. Throughout my time in the Zimmerman and Sanford lab I have had many thoughtful conversations, interactions, and developed enough memories to fill a lifetime with reflection. In particular I want to thank Joshua Kammeraad and Andrew Molina for their emotional support and worldly insight. Josh and Andrew: I will not forget our meaningful conversations about chemistry, philosophy and the meaning of existence.

My fellow cohorts: Alan, Andrew, Jordan, Nomaan, Sydonie, Pablo, and Nicole, I want to thank them for all of their help, patience and support. Thank you also to the individuals who guided and collaborated with me while they were post-docs: James Suttil, Doug Genna, Megan Cismesia, Christo Sevov, Sarah Ryan, Eric Walker and especially Mónica Pérez-Temprano and Hyungjun Kim. Finally, while there are too many people to list I want to thank everyone from the Zimmerman and Sanford lab for their scientific support, companionship and humor.

Finally, to my friends and family. Thank you for all of the fun times climbing, hiking and relaxing. To my parents, for instilling in me a deep appreciation for knowledge and learning. Finally, to Tiffiny Micyus, the love of my life. I couldn't have done any of this without you.

Table of Contents

Dedication ii
Acknowledgements iii
List of Figures vi
List of Tables xi
List of Equations xii
List of Appendices xiii
Abstract xiv
Chapter 1: Introduction 1
1.1 Exploring Reaction Landscapes with Computational Chemistry 1
1.1.1 Potential Energy Surfaces and Reaction Pathways 2
1.1.2 Relating Potential Energy Surfaces to Experimental Chemistry 3
1.2 Automated Reaction Path Finding Using ZStruct 4
1.2.1 Transition State Finding for Connecting Intermediates 5
1.2.2 Overview of ZStruct - an Automated Reaction Discovery Tool 7
1.3 Application of ZStruct to CO_2 and NH_3BH_3 reactivity 9
1.4 Constructing the Reaction Landscape 13
1.5 Dissertation Outline 14
1.6 References 16
Chapter 2: Reactivity and Mechanism for C(sp^3)-N Bond-Forming Reductive Elimination from Palladium(IV) 23
2.1 Abstract 23
2.2 Introduction 24
2.3 Results and Discussion 26
2.3.1 Possible Mechanisms for C–N Reductive Elimination from Pd^{IV} Complexes 26
2.3.2 Previous Studies of 1_{Ts} 28
2.4 Experimental Studies of C(sp^3)-N Coupling 29
2.4.1 Initial Screen of Sulfonamide Nucleophiles 29
2.4.2 C(sp^3)-N Reductive Elimination from 1_{Tf}, 1_{Ms} and 1_{TsNMe} 31
2.4.3 Lability of the sulfonamide ligand in 1_{Tf}, 1_{Ms} and 1_{TsNMe} 34
2.4.4 1-a/1-b Isomerization Process 34
2.4.5 Summary and Conclusions from Experimental Studies 36
2.5 Identification of Isomerization Mechanism Using Computational Combinatorial Reaction Finding 37
2.5.1 Reaction Path Identification 37
2.5.2 Computational details 38
2.5.3 Overview of ZStruct Results 40
2.5.4 ZStruct Pathways for Isomerization 40

2.6 ZStruct Evaluation of C(sp^3)–N Bond-Forming Reductive Elimination 42
2.6.1 Pathway IV 43
2.6.2 Pathway V 44
2.7 Computational Sulfonamide Screen and Experimental Verification 46
2.8 Additional predictions based on thermodynamic considerations 48
2.9 Conclusions 50
2.10 References 51
Chapter 3: The Thermodynamic Landscape and Descriptors of Cobalt catalyzed CO2 Reduction 56
3.1 Introduction 56
3.2 Computational Benchmarking 58
3.2.1 Bisphosphine Library and Thermodynamic Landscape 59
3.3 Qualitative assessment of the thermodynamic landscape 61
3.4 Exploring Molecular Feature Based Descriptions of the Thermodynamic Landscape 64
3.5 Selection of the Best Catalyst Using QM Calculations 70
3.6 Conclusions 74
3.7 Computational Details 74
3.8 References 75
Chapter 4 Final Remarks 83
4.1 Research Summary 83
4.2 Constructing Reasonable Models 84
4.1 Final Thoughts 87
4.1 References 88
Appendices 89

List of Figures

Figure 1.1 Example potential energy surface showing global minimum (A), local minimums (B,C,D), and transition state ($AB^{\ddagger}$) 2

Figure 1.2 Simple reaction schematic mirroring minimum energy path from Figure 1.1 3

Figure 1.3 Overview of double-ended GSM transition state finding approach with the final transition state adjustment outlined in red 6

Figure 1.4 Simulated potential energy surface showing four low energy wells corresponding to hypothetical intermediates (A, B, C, and D) 7

Figure 1.5 Examples of connectivity rules implemented in ZStruct 8

Figure 1.6 Two-step synthesis of BCN 9

Figure 1.7 Automated reaction finding (ZStruct) iterative logic including addition of reagents . 10

Figure 1.8 Energy profile for 3b and 4 formation (ΔG at 373K) 11

Figure 1.9 Summary of Cy-BCN formation pathways 11

Figure 1.10 Cy-BCN precursor formation from 4 and NH_2BH_2. The blue and black paths indicate the most favorable paths for 5 and 6 formation, respectively 12

Figure 1.11 Illustration of QSER for five example SN_2 leaving groups and the effect on the free energy of reaction 14

Figure 2.1 C(sp^3)–N Bond-Forming Reductive Elimination from 1_{Ts} 24

Figure 2.2 ZStruct mediated mechanism discovery incorporates known and non-intuitive chemical pathways 25

Figure 2.3 New Pathway for C(sp^3)–N Reductive Elimination of Sulfonamide Substrates Discovered by ZStruct..... 26

Figure 2.4 Pathway I: Direct Nucleophilic Attack..... 27

Figure 2.5 Pathway II: Bipyridine Ligand Dissociation 27

Figure 2.6 Pathway III: Concerted Reductive Elimination 28

Figure 2.7 Pathway IV: S_N2 Pathway 29

Figure 2.8 Ligand Effects on the Rate of C(sp^3)–N Reductive Elimination 32

Figure 2.9 Eyring plot for determination of $\Delta H^{\ddagger}$ and $\Delta S^{\ddagger}$ for the $C(sp^3)$–N reductive elimination from 1_{Ms} 33

Figure 2.10 1_R-a/1_R-b isomerization 35

Figure 2.11 1_{Ms}-a/1_{Ms}-b isomerization process at 45 ºC. Solid lines are the best fit using GEPASI 36

Figure 2.12 Possible unobserved Pd^{IV} isomers 37

Figure 2.13 Overview of the ZStruct Combinatorial Reaction Finding Tool 38

Figure 2.14 Screening and activation energy cutoffs ($\Delta G^{\ddagger}$) used for finding the lowest energy pathways from 1_{Ms}. *Improved density functional incorporating long-range and dispersion corrections 39

Figure 2.15 Overview of ZStruct search of the reactivity of 1_{Ms}-a involving multiple unproductive search paths as well as known and unknown chemical reactivity. Shown in blue are expected chemical reactivity while red highlights the non-intuitive reaction paths 40

Figure 2.16 Two pathways for isomerization of 1_{Ms}-a to 1_{Ms}-b 41

Figure 2.17 Energy barriers for pathways leading to the formation of 1_{Ms} isomers 42

Figure 2.18 Pathway IV. $C(sp^3)$–N reductive elimination pathway from 1_{Ms}-a. 43

Figure 2.19 (a) $C(sp^3)$–N reductive elimination transition state $TS11_{Ms}$ from 1_{Ms}-a (in Pathway IV). (b) $C(sp^3)$–N reductive elimination transition state $TS12_{Ms}$ from 1_{Ms}-b (in Pathway V) 44

Figure 2.20 Pathway V from 1_{Ms}-b 45

Figure 2.21 Pathway V. $C(sp^3)$–N reductive elimination from 1_{Ms}-b. All energies are referenced to 1_{Ms}-a. 45

Figure 2.22 Comparison between computational and experimental $\Delta G^{\ddagger}$ for $C(sp^3)$–N reductive elimination. The point computation predicted prior to experiment is highlighted in red 46

Figure 2.23 $C(sp^3)$–N versus $C(sp^3)$-$C(sp^2)$ reductive elimination from common pentacoordinate intermediate 4_{BisTf}. All energies referenced to 1_{BisTf}-a 49

Figure 2.24 Thermolysis of 3 in the presence of NMe_4NTf_2 50

Figure 3.1 a) Catalytic cycle for CO2 reduction by cobalt bis(diphosphine) metal complexes b) Free energy diagram for $Co(dmpe)_2H$ catalyzed CO2 reduction using Verkade's base 56

Figure 3.2 Experimental and calculated hydricity values using ωB97X-D/Def2-SVP level of theory comparing SMD-$PCM_{acetonitrile}$ and $PCM_{acetonitrile}$ 60

Figure 3.3 Outline of the bis(diphosphine) ligand library approach used for this study 61

Figure 3.4 ωB97X-D/Def2-SVP/PCM$_{acetonitrile}$ thermodynamic landscape shown in color with ωB97X-D/Def2-SVP/PCM$_{THF}$ shown as a background in grey (a) Hydricity (kcal·mol^{-1}) versus pK_a with H_2 binding (kcal·mol^{-1}) on the Z-axis (b) Hydricity (kcal·mol^{-1}) versus H_2 binding (kcal·mol^{-1}) with pK_a on the Z-axis 62

Figure 3.5 Quantitative analysis of ligand population for the (a) most-acidic and (b) least-acidic regions of the thermodynamic landscape 63

Figure 3.6 Quantitative analysis of ligand population in the (a) most hydridic and (b) least hydridic regions of the thermodynamic landscape 64

Figure 3.7 Features considered in constructing a molecular representation for pK_a and hydricity.. 66

Figure 3.8 QM calculated (a) pK_a and (b) hydricity versus Co—H NLMO energy (eV) 68

Figure 3.9 Illustration of effects on pKa B and hydricity C caused by modulation of Co—H NLMO energies 69

Figure 3.10 Stepwise reduction of the thermodynamic landscape toward the selection of best-case catalysts 71

Figure A.1 Detailed outline of computational filtration tiers. Each box contains a summary of the level of theory and the energy cutoff used. Structures passing the threshold proceed to the next level filter. 90

Figure A.2 Overlays of B3LYP/LANL2DZ and ωB97X-D/LANL2TZ(f)/PCM-SMD geometry optimizations for (a) 1$_{Ms}$-a and (b) 1$_{Ms}$-b. 92

Figure A.3 C(sp^3)-N reductive elimination from 1$_{Ms}$-a with explicit solvent (a) forced in every step (b) not present in any step and (c) used only where necessary in the calculations 93

Figure A.4 (a) C(sp^3)–N reductive elimination transition state TS11$_{Ms}$ from 1$_{Ms}$-a (in Pathway IV), reference for labels shown in Table S37. (b) Pd^{IV} reductive elimination transition state TS12$_{Ms}$ resulting from 1$_{Ms}$-b (in Pathway V), reference for labels shown in Table S37..... 95

Figure A.5 (a) Calculated $\Delta G^{\ddagger}$ for pathway IV versus sulfonamide conjugate acid pK_a (b) Calculated $\Delta G^{\ddagger}$ for pathway V versus sulfonamide conjugate acid pK_a 96

Figure A.6 Comparison of distances between sulfonamide N-R group and fluorine for TsNMe$^-$ and TsNH$^-$ substrates 98

Figure A.7 Summary of **1$_{Ms}$** pathways 99

Figure A.8 Summary of **1$_{Tf}$** pathways 100

Figure A.9 Summary of **1$_{Ts}$** pathways 101

Figure A.10 Summary of **1$_{TsNMe}$** pathways 102

Figure A.11 Summary of $\mathbf{1_{CF2H}}$ pathways 103

Figure A.12 Summary of C(sp^3)-N reductive elimination 1_{BisTf} pathways 104

Figure A.12 Summary of C(sp^3)-C(sp^2) reductive elimination from penta-coordinate palladium complex 106

Figure A.14 Isomerization of 1_{Ms}-a to 1_{Ms}-b (a-b) 106

Figure A.15 Isomerization of 1_{Ms}-a to 1_{Ms}-b (a-b) 107

Figure A.16 Isomerization of 1_{Ms}-a to 1_{Ms}-c and 1_{Ms}-d (a-b) 108

Figure A.17 Isomerization of 1_{Ms}-a to 1_{Ms}-e (a-b) 108

Figure A.18 Summary of results for pathway V 109

Figure A.19 Summary of results for pathway IV (a-b) 109

Figure A.20 Direct C-N reductive elimination from 1_{Ms}-b (energies relative to 1_{Ms}-a) 110

Figure A.21 Comparison of lowest energy pathways for bipyridine dissociation (a-d) 111

Figure A.22 Bipyridine dissociation from 1_{Ms}-a: alternatives to Pathways II (a-c) 112

Figure A.23 Additional acetonitrile exchange pathways from 1_{Ms}-a (a-e) 114

Figure A.24 Pathways from 1_{Ms}-b (a-d) 115

Figure B.1 Overview of this article and relevant methods for each section 118

Figure B.2 Overview of ligands used in benchmark calculations and thermodynamic landscape 119

Figure B.3 Comparison of experimental and calculated pK_a values using gas phase, solvation SMD-PCM in acetonitrile, and SMD-PCM$_{(acetonitrile)}$ plus vibrational zero point energy corrections at the B3LYP/LANL2DZ level of theory 122

Figure B.4 Comparison of experimental and calculated pK_a values using various functionals in combination with the LANL2DZ basis set and SMD-PCM solvation model with acetonitrile .. 122

Figure B.5 Comparison of experimental and calculated pK_a values using ωB97X-D functional in combination with the various basis sets and the SMD-PCM solvation model with acetonitrile .. 123

Figure B.6 Experimental and calculated pK_a values using ωB97X-D/Def2-SVP level of theory comparing SMD-PCM and PCM solvation models with acetonitrile 124

Figure B.7 Comparison of the gas phase relative acidity for the reaction of MH → M at CCSD(T) and ωB97X-D density functionals 124

Figure B.8 Comparison of experimental and calculated hydricity values using gas phase, solvation SMD-PCM in acetonitrile, and SMD-PCM$_{acetonitrile}$ plus vibrational zero point energy corrections at the B3LYP/LANL2DZ level of theory 127

Figure B.9 Comparison of experimental and calculated hydricity values using various functionals in combination with the LANL2DZ basis set and SMD-PCM solvation model with acetonitrile 128

Figure B.10 Comparison of experimental and calculated hydricity values using ωB97X-D functional in combination with the various basis sets and the SMD-PCM solvation model with acetonitrile 128

Figure B.11 Comparison of the gas phase relative acidity for the reaction of MH → M at CCSD(T) and ωB97X-D density functionals 129

Figure B.12 Experimental and calculated hydricities using ωB97X-D and CCSD(T) with Def2-SVP/PCM$_{acetonitrile}$ 129

Figure B.13 Overview of catalyst construction using a modified version of ZStruct and the growing string method (GSM) to generate all possible catalyst-ligand combinations 130

Figure B.14 Instances of failure throughout H_2 binding assessment denoted by ligand label 131

Figure B.15 QM calculated pK_a versus the equation B4 model shown for the full thermodynamic landscape including all complexes 132

Figure B.16 QM calculated pK_a versus the equation B4 model shown for the full thermodynamic landscape including all complexes 133

Figure B.17 Single term model shown in equation B5 versus QM calculated pK$_a$ using NLMO 134

Figure B.18 12 term model shown in Equation B7 versus QM calculated pK$_a$ 135

Figure B.19 LASSO derived molecular feature model for pK_a versus QM calculated pK_a. 136

List of Tables

Table 2.1 Reductive elimination reaction rate constant for C(sp^3)–N coupling using different sulfonamides 31

Table 2.2 Activation parameters for the C(sp^3)–N bond forming reaction 33

Table 2.3 Thermodynamic and activation parameters for the isomerization process using different sulfonamide substrates 36

Table 2.4 Comparison of lowest barrier calculated C(sp^3)–N reductive elimination and experimentally measured $\Delta G^{\ddagger}$ values for various sulfonamides 47

Table 3.1 Entries 1-10 show the top thermodynamically relevant Co(L)(L')H2 complexes from the landscape while entries 11-13 highlight catalytically competent homoleptic catalysts 72

Table A.1 Comparison of energetics for key intermediates at various levels of theory 91

Table A.2 C-N Reductive Elimination Summary 94

Table A.3 Geometry comparison for $TS11_{Ms}$ and $TS12_{Ms}$ for various sulfonamides 95

Table B.1 Overview of calculated values for pK_a. Red represents the highest values while blue shows the lowest values 121

Table B.2 Overview of calculated values for hydricity. Red represents the highest values while blue shows the lowest values 126

List of Equations

Equation 1.1 Expression for the equilibrium constant of reaction example shown in Figure 1.2 .. 4

Equation 1.2 Eyring equation relating the reaction rate, *r*, to $\Delta G^{\ddagger}$ 4

Equation 1.3 Evans-Polanyi principle relating the activation barrier of a reaction to the difference in enthalpy of reaction 13

Equation 3.1 Equation relating the ε_{NLMO} energy with pK_a shown in figure 3.8a 68

Equation 3.2 Equation relating the ε_{NLMO} energy with hydricity shown in figure 3.8b 68

Equation B.1 Reference calculation for pK_a 120

Equation B.2 Overview of experimental derivation of hydricity values for benchmark calculations 126

Equation B.3 Overview of second method for experimental derivation of hydricity values for benchmark calculations 127

Equation B.4 Multiterm QSAR model describing entire thermodynamic landscape describing pK_a 132

Equation B.5 Multiterm QSAR model describing entire thermodynamic landscape targeting hydricity 133

Equation B.6 Single term equation represented by the NLMO describing the thermodynamic landscape 134

Equation B.7 12 term QSAR model describing reduced thermodynamic landscape targeting pK_a 135

Equation B.8 7 term QSAR model in the absence of NBO and NLMO features describing reduced thermodynamic landscape targeting pK_a 136

List of Appendices

Appendix A: Supporting Data for Chapter 2 89

Appendix B: Supporting Data for Chapter 3 118

Abstract

Computational chemistry is becoming a widely used tool to investigate the kinetics and thermodynamics of chemical transformations. These investigations are often heavily guided by experiment and require significant mechanistic insight prior to meaningful model development. Recent advances in reaction path finding and automated potential energy surface assessment have enabled faster and easier exploration of complex chemical mechanisms. In combination with mechanistic information, structure energy correspondence provides information which describes how a particular reaction mechanism energetically varies as structure is modulated. Together, the relevant reaction pathways and the structure energy relationships describe the reaction landscape for a given class of reactivity.

Chapter 1 introduces the core chemical concepts needed to understand reaction landscapes. The tools and information needed to perform detailed mechanistic exploration via computation are presented and competing methods are summarized. Further discussion of reaction path finding tools is provided through an example involving the reactivity of ammonia borane and carbon dioxide. A discussion of the characteristics which connect potential energy surfaces to quantitative structure activity relationships is used to conclude this chapter.

Chapter 2 details the application of an automated reaction path finding tool for the investigation of intuitive and non-intuitive pathways for C(sp^3)-N reductive elimination from palladium(IV). This work demonstrates that detailed computational studies using automated reaction path investigation can be used to assess unexpected reaction pathways. These simulations predicted the relative reaction rates with various sulfonamides through consideration of both intuitive and non-intuitive reaction mechanisms. Overall, this chapter demonstrates that combinations of experimental studies and computational tools can provide fundamental mechanistic insights into complex organometallic reaction pathways. This work begins to explore relevant molecular features which appear to trend well with the experimentally observed reactivity.

Chapter 3 continues the development of molecular feature based investigation. This chapter was inspired by the possibility of using computational investigations of complex

organometallic reaction landscapes to describe structure energy correspondence. This section discusses the development of a thermodynamic landscape to investigate CO_2 reduction from cobalt bis(diphosphine) complexes. The construction of a dataset of Co(L)(L')H_2 type complexes from set of commercially available of bis(diphosphines) covering a thermodynamic landscape of over 50 orders of magnitude acidity and hydricity is discussed. These data suggest that relationships between common steric and electronic molecular features are poorly correlated with catalyst thermodynamics. However, a strong correlation between the thermodynamics and Co—H NLMO energy is observed. The landscape provides a clear example of careful electronic balance required for catalytic relevance. The best catalyst identified for future experimental investigations was Co(dCype)H, which is expected to be more acidic and hydridic than previously reported Co(dmpe)$_2$H.

While there is still significant work remaining in the development of robust and automated computational chemistry tools, this work outlines some potential applications and details the relevant findings. The final chapter discusses the current limitations and challenges associated with computational reaction discovery. Particular attention is paid to the development of reasonable organometallic computational models for use in reaction landscape investigation.

Chapter 1: Introduction

1.1 Exploring Reaction Landscapes with Computational Chemistry

Mechanistic understanding at an atomistic level is a fundamental building block of chemical intuition. Computational chemistry has become increasingly popular as a fast and accurate tool to supplement experimental mechanistic studies. Computational methods that offer a high accuracy with low cost, such as density functional theory (DFT), have been increasingly used for the resolution of complex chemical mechanisms. The average citation count for papers incorporating DFT has increased from below 100 per year in the early 1990's to well over 10,000 per year in 2017.[1,2] In spite of the widespread success of DFT in mechanistic studies, studying reactivity through simulation is still quite challenging. While experimental chemistry is able to quickly assess the success or failure of a reaction, computational chemistry requires a detailed map of the reaction landscape before making the same assessment. Thoroughly understanding chemistry from a simulation first perspective relies upon two types of investigations: assessment of the potential energy surface associated with a single reaction and quantitative structure activity relationships, or mathematical descriptions of how the potential energy surface changes as a function of atomistic modifications to the structure. Computationally resolving the reaction landscape requires identification of all intermediates, transition states, and products resulting from a single reactant molecule as well as the effects of varying atomistic composition. This work details the application of DFT, automated reaction path finding, and statistical analysis of molecular environment to the resolution of reaction landscapes.

The first half of this dissertation discusses the application of ZStruct, an automated reaction path finding tool, to the elucidation of $C(sp^3)$-N, $C(sp^3)$-$C(sp^2)$, and $C(sp^3)$-F reductive elimination from Pd(IV). The second half utilizes an array of DFT and modeling tools in combination with statistical analysis to uncover the structure energy relationship for cobalt bis(diphosphine) catalyzed reduction of CO_2. In the following sections a summary of background material necessary for understanding computational mechanistic investigations will be discussed. Related material has been covered extensively in previous reviews.[3–5] The interested reader is encourage

to explore these reviews if a deeper understanding is desired. We continue this introduction with a background on the theory and methods for resolving potential energy surfaces in Section 1.1.1.

1.1.1 Potential Energy Surfaces and Reaction Pathways

Ab initio simulations provide a computation first perspective on how reactant molecules, and sometimes catalysts, proceed through chemical reactions. A chemical reaction pathway is one of the many available free energy paths leading from starting materials to products on a potential energy surface (PES). The PES is a high dimensionality surface consisting of approximately 3N dimensions (where N represents the number of atoms in the molecule of interest). The field of computational chemistry is largely focused on application of quantum chemistry, especially density functional theory, to discover the most accessible and relevant pathways for navigating the PES.

The surface can be roughly divided into two main categories: stable local minima which resolve thermodynamics and first order saddle points, or transition states, which provide information about the kinetics of a chemical reaction. In the search of local minima, discrete chemical structures are geometrically optimized to the lowest point of the potential energy surface (PES). A variety of structural optimization techniques are available in most modern quantum mechanics simulation packages, but most use a set of standard optimization methods.[6,7] The reference state for a chemical reaction should ideally correspond to the global minimum, or the lowest possible point on the PES (Figure 1, **A**). Local minima sometimes correspond to chemical intermediates along the reaction path (Figure 1.1, **B,C,D**) which are connected by transition states (Figure 1.1, $[AB]^{\ddagger}$).

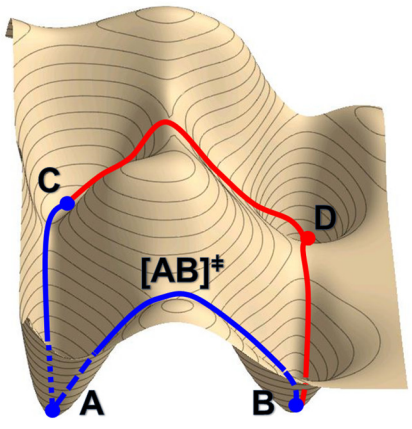

Figure 1.1 Example potential energy surface showing global minimum (**A**), local minimums (**B,C,D**), and transition state ($\mathbf{AB}^{\ddagger}$).

The minima and transition states are often referred to as stationary points on the PES. The minimum energy path connects the stationary points which proceed through the lowest transition states leading to a stable product (Figure 1.1, pathway connecting A, B and D). These reaction profiles are often viewed from a side-on perspective to better visualize the energetic differences between the stationary points (Figure 1.2).

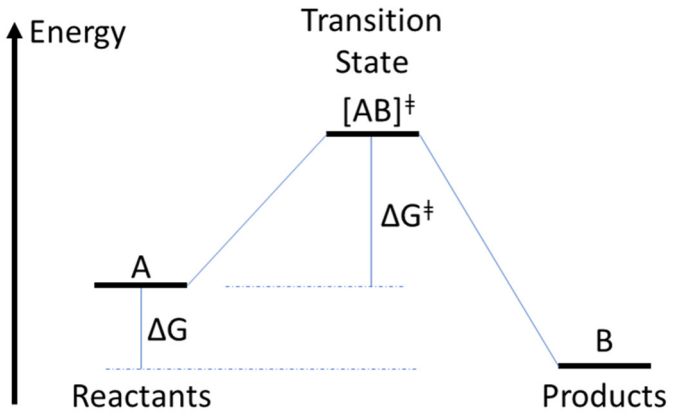

Figure 1.2 Simple reaction schematic mirroring minimum energy path from Figure 1.1

Figure 1.2 illustrates a side on view of the potential energy surface shown in Figure 1.1. Taken together, the stationary points and minimum energy path are often the most relevant portions of the PES.[5]

1.1.2 Relating Potential Energy Surfaces to Experimental Chemistry

Models of potential energy surfaces have been fundamental in unifying understanding regarding quantum principles to the macroscale behavior of molecular reactivity. The utility of reaction pathways results from the close relationship between the model molecular system used to construct the PES, experimental chemistry and chemical intuition. The minima are molecular structures which are often experimentally stable and physically observable species. Ground state species often exist in chemical equilibrium with one another. The ratio of species at equilibrium can be used to calculate K_{eq}. The equilibrium in the ratio of products in experiment is described by the simple equilibrium expression for K_{eq} (equation 1.1):

$$K_{eq} = e^{-\frac{\Delta G}{RT}} = \frac{[A]^{\sigma}}{[B]^{\rho}}$$

Equation 1.1 Expression for the equilibrium constant of reaction example shown in figure 1.2

In equation 1.1 K_{eq} is the equilibrium constant for the reaction, ΔG is the difference in energy (similar to that shown in figure 1.2), *R* is the universal gas constant, and *T* is the temperature in Kelvin. The second half of the equation shows the approximate relationship between K_{eq} and the ratio of molar concentration of reactants and products, *A* and *B*, and the order of those species in the equilibrium, σ and ρ, respectively. This example, while simplified, demonstrates the close correspondence between experimentally observable equilibrium phenomena and the energy values obtained through calculations.

Computational models of transition states are related to experimentally observable reactions rates by transition state theory. Equation 1.2 shows the Eyring equation which relates $\Delta G^{\ddagger}$ to the rate of reaction.

$$r_{\{A \rightarrow B\}} = \kappa \left(\frac{k_B T}{h}\right) e^{-\left(\frac{\Delta G^{\ddagger}}{RT}\right)}$$

Equation 1.2 Eyring equation relating the reaction rate, *r*, to $\Delta G^{\ddagger}$

In equation 1.2, *r* is the rate of the reaction of *A* to *B*, κ is the transmission coefficient, k_B is Boltzman's constant, T is temperature in Kelvin, *h* is Planck's constant, R is the universal gas constant and $\Delta G^{\ddagger}$ is the transition state energy. This relationship provides the necessary framework to connect atomic structure at the transition state to macroscale observable phenomena in experimental chemistry. The equations relating the computationally calculated free energies of the potential energy surface to experimentally observable rates and concentrations provide the necessary framework to interrogate molecular reactivity through computational chemistry.

1.2 Automated Reaction Path Finding Using ZStruct

The close relationship between the models developed in computational chemistry and experimentally observable phenomena has motivated faster and more automated methods to assess potential energy surfaces. The ability to quickly and automatically assess a potential energy surface

holds the potential to enable reaction prediction in silico.[8–10] However, resolving relevant local minima and saddles points on potential energy surfaces has proven to be a considerable challenge for computational chemistry. A number of methods have been developed which provide a means to navigate these surfaces with increasing reliability while attempting to minimize user interaction. Reaction discovery by computation based on PES analysis can be divided into four main classifications: (1) Expert encoded,[11–26] (2) Transition state centric,[27–42] (3) Stringing together intermediates,[43–50] and (4) reaction coordinates to find reaction paths.[51–58] This work demonstrates the application of computational tools relating to primarily the third class of reaction path exploration. The following sections provide the background information to understand automated transition state finding and reaction path discovery as it relates to exploring PESs by stringing together intermediates.

1.2.1 Transition State Finding for Connecting Intermediates

Due to the high computational cost, exhaustive exploration of the PES is currently infeasible. One solution is instead to focus on chemically meaningful intermediates which relate to breaking and forming select chemical bonds and analyzing the resulting reaction pathways. PES search techniques which string together intermediates must be able to generate the relevant intermediate molecular structures and subsequently connect them using transition state search techniques. As such, selection of accurate, automated methods for transition state finding is vital to successful PES investigations.

Transition state finding can be divided into three main classes: (1) methods requiring IRC confirmation[59–72] (2) double ended string methods,[73–77] and (3) single ended string methods.[78] For general purpose investigation of discrete reaction paths, computational chemistry largely used method 1.[5,79] This method searches for the exact molecular structure of the transition state as it relates to the start and end point by approximating the structure using chemical intuition or by software which interpolates between the starting and ending structures of the reaction path.[61–72] For any guess-structure driven transition state search, the final step of analysis requires an intrinsic reaction coordinate scan to confirm that the isolated transition state is connected to the desired starting and end points of the reaction path.[80,81] These methods are typically user intensive, requiring multiple iterations to successfully locate and confirm a single transition state.

Automated double-ended string methods provide the same results as IRC confirmation methods, but with significantly less user interaction. String methods[75–77] and nudged elastic band[59,62,82,83] are the among the most commonly employed double ended methods when the two endpoints of a reaction path are known. More recently developed methods have improved upon the speed and accuracy of string method including double ended growing string method (GSM)[73,74] and single ended string method (SEM).[78] The double ended GSM is primarily used throughout this document. The GSM operates through iterative structure optimization of the reaction path connecting two points on the potential energy surface (Figure 1.3).

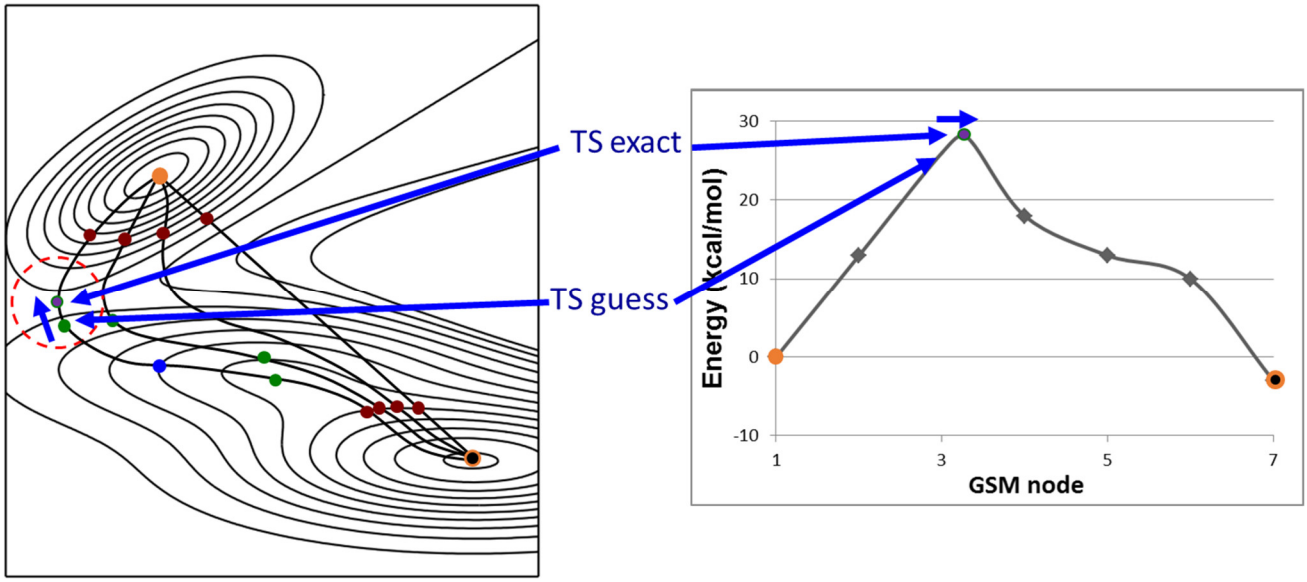

Figure 1.3 Overview of double-ended GSM transition state finding approach with the final transition state adjustment outlined in red

The program interpolates between the starting point (shown in figure 1.3 as an orange circle) and the end point (figure 1.3 black circle orange outline) to generate the first set of node structures. These nodes are then geometrically optimized orthogonal to the guess reaction path. The process is repeated until a saddle point is detected. The gradient information of the reaction path is then used to optimize the transition state structure. All of these steps occur automatically after the initial starting and endpoints are provided.

1.2.2 Overview of ZStruct - an Automated Reaction Discovery Tool

Advances in automated transition state finding have provided the groundwork for targeting bulk assessment of stationary points on single PES, even for complex reactivity. In combination with fast DFT implementation, advances in transition state finding has enabled tractable resolution of even complex PESs provided guess structures for the starting and endpoints are provided systematically. One method that systematically explores intermediates is ZStruct, a program put forth by the Zimmerman lab to enable broader computational exploration of PESs.

ZStruct provides a set of tools to investigate reaction mechanisms by searching through individual elementary reaction steps, similar to a true chemical reaction sequence. By iteratively discovering plausible elementary steps, characterization of complete multi-step, multi-pathway reaction mechanisms become possible (**Figure 1.4**) even in systems where the reaction mechanism is not known to chemical intuition. While ZStruct can be employed with any level of quantum chemical theory (i.e. any functional, basis set, and solvent model can be used) to describe the atomistic reaction processes, herein we use density functional theory and implicit solvation models due to their low cost to accuracy ratio.

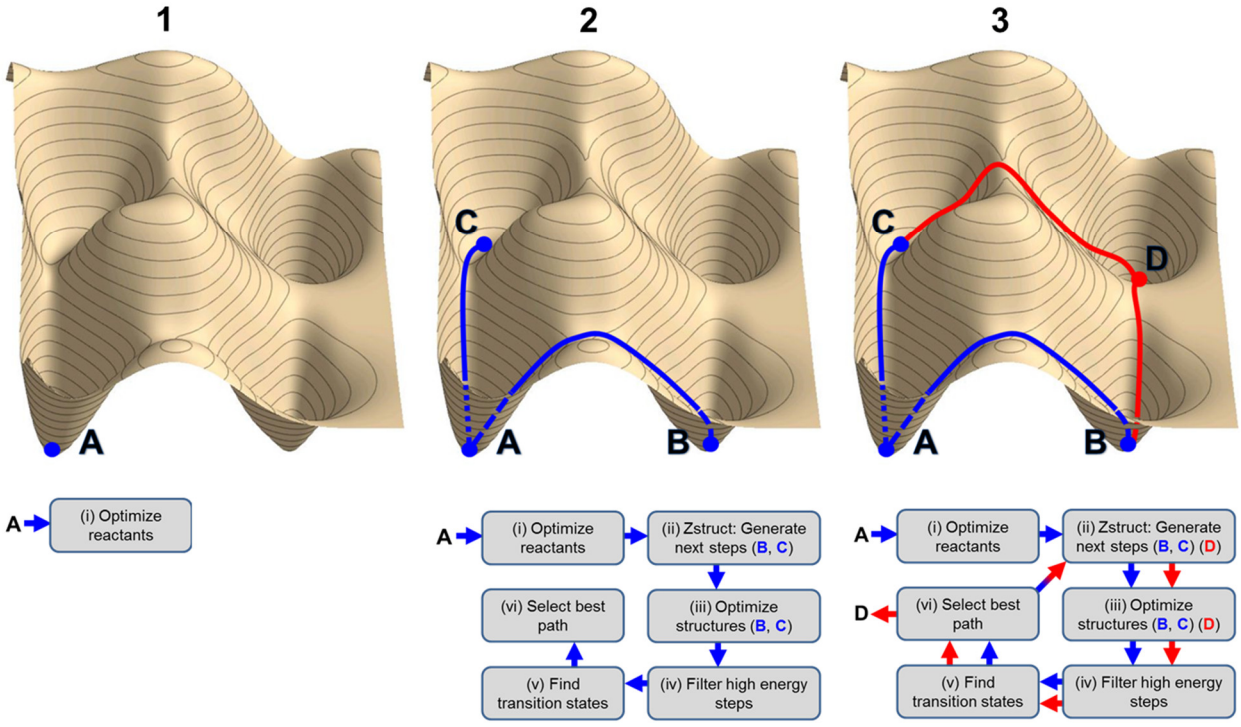

Figure 1.4. Simulated potential energy surface showing four low energy wells corresponding to hypothetical intermediates (A, B, C, and D).

To begin reaction discovery, ZStruct requires input of the optimized starting material, A (see **Figure 1.4**, step i). Intermediates B and C (step ii) are created through software application of connectivity rules describing possible elementary reactions (**Figure 1.5**).

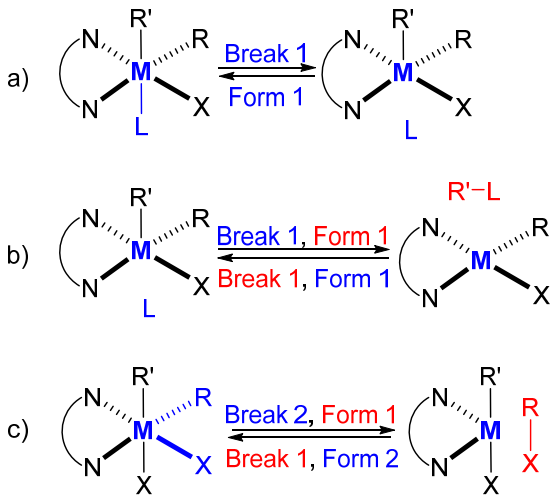

Figure 1.5 Examples of connectivity rules implemented in ZStruct.

Examples of these elementary reactions (applied to an octahedral metal center in this example) include: (a) Break 1 results in the M—L bond breaking. M—L formation is generated through a Form 1 operation. (b) Combinations of "Break 1" and "Form 1" enables the generation of more complex single elementary steps. In this case the "Break 1, Form 1" breaks the M—R bond, and forms R-L. This process is similar to what one might expect for an S_N2-like reductive elimination. (c) Break and form combinations provide other important chemical processes such as direct reductive elimination from octahedral complexes. In this case the M—R and M—X bonds break and the R-X bond is formed in a concerted fashion.

These intermediates are optimized (step iii, **Figure 1.4**) by DFT, thereby obtaining the thermodynamic plausibility of the reaction. High-energy structures which are considered to be unstable or unobtainable under the reaction conditions are removed from subsequent analysis through energy filters. GSM then performs a double-ended reaction path search to connect the initial structure to thermodynamically plausible intermediates (e.g. B,C of **Figure 1.4**). Importantly, GSM provides the minimum energy path and exact transition state simultaneously. The activation barrier from GSM is used to identify the most kinetically relevant reaction steps (step v).

1.3 Application of ZStruct to CO_2 and NH_3BH_3 reactivity

This section based upon published work: Li, M. W.; Pendleton, I. M.; Nett, A. J.; Zimmerman, P. M. Mechanism for Forming B,C,N,O Rings from NH_3BH_3 and CO_2 via Reaction Discovery Computations. *J. Phys. Chem. A* **2016**, *120* (8), 1135–1144.

One of the first applications of ZStruct was toward the discovery of plausible mechanism for BCN formation from ammonia borane, NH_3BH_3, and CO_2 Figure 1.6.

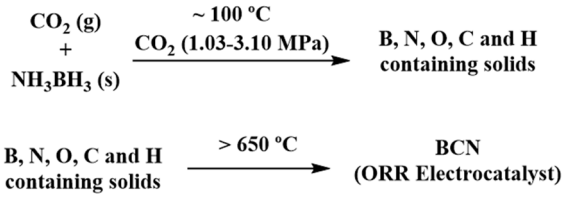

Figure 1.6 Two-step synthesis of BCN.[84–86]

The anticipated complexity and unknown nature of reactions involving CO_2 and AB provided a prime target for application of ZStruct and the growing string method. A unique aspect of this project was the incorporation of additional reagents throughout the ZStruct analysis. For each set of reactants, a complete investigation of the accessible reaction pathways was performed. Once the complete set of favorable elementary steps are found, additional reagents like AB or CO_2 were added to the simulation and the process is repeated. An outline of reagent addition process is shown in Figure 1.7. The outer ring is associated with the typical ZStruct operation (identical to steps ii-vi, Figure 1.4), while reagent addition was incorporated specifically for the study of $CO_2$and AB reactivity.

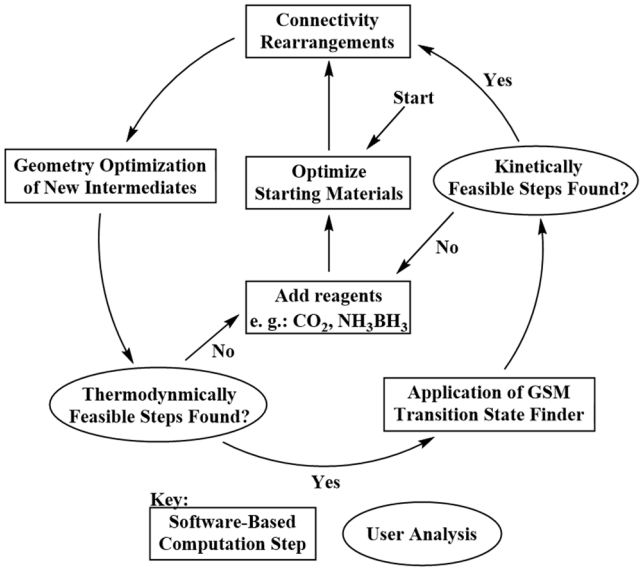

Figure 1.7 Automated reaction finding (ZStruct) iterative logic including addition of reagents.

Using the reactants AB and CO_2 (1) as a starting point, ZStruct located the paths shown in Figure 1.8. TS **I** effects simultaneous two-hydrogen transfer from AB to CO_2, forming FA and NH_2BH_2 (**2**) with a barrier of 27.8 kcal/mol above 1.[87,88] The energy profile for this reactivity (Figure 1.8) highlights the favorable covalent B-O bond formation step (reaction **II**) compared to the higher barrier two-hydrogen transfer steps in reactions **I** and **III**. The comparatively large downhill free energy of reaction for **II** also emphasizes the stability of FAB and its derivative **4**, which is especially important due to the observed production of carbon-containing compounds under relatively high temperatures of around 100 C.[84–86] ZStruct elucidation of these reaction pathways was crucial to the identification of B-O bond formation as a thermodynamic driving force associated with AB/CO_2 reactivity.

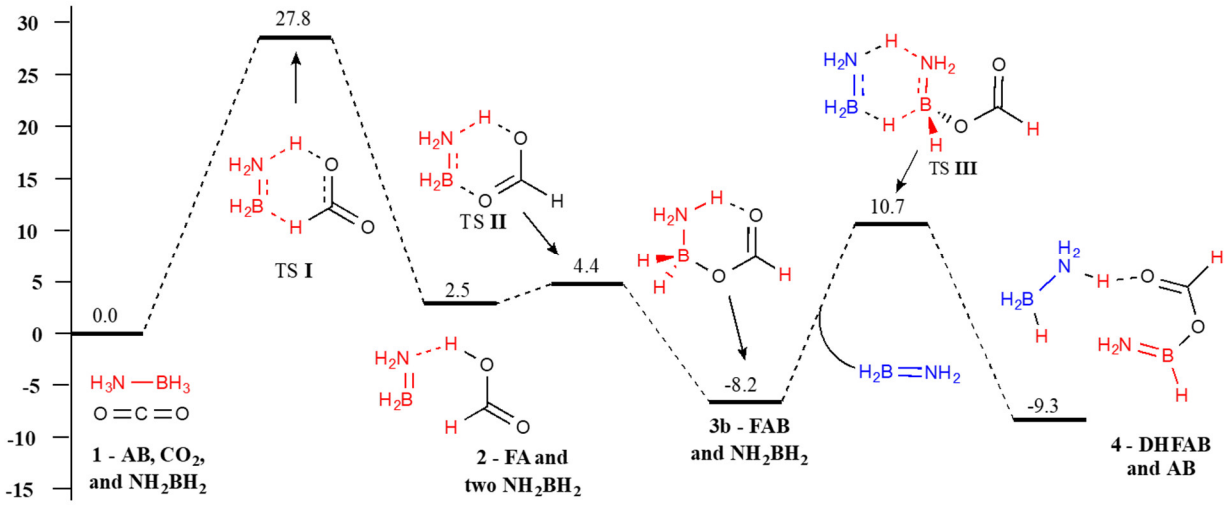

Figure 1.8 Energy profile for **3b** and **4** formation (ΔG at 373K).

Subsequent analysis revealed a number of competing reaction pathways, elucidated entirely through systematic analysis using ZStruct. A summary of these pathways is included in Figure 1.9.

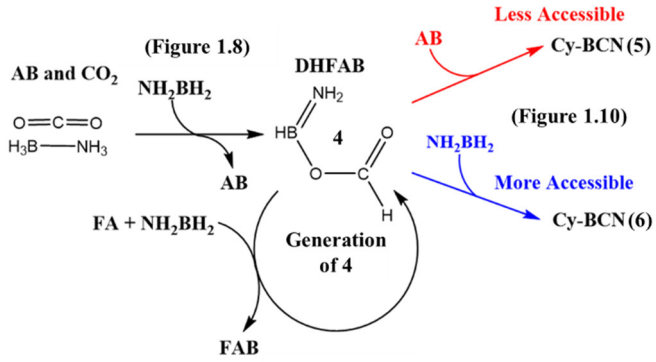

Figure 1.9. Summary of Cy-BCN formation pathways.

ZStruct analysis provided a large scope of reactivity eventually leading to the identification of competitive ring forming events. Starting from only two reagents, CO_2, and NH_2BH_2, accessible reaction paths leading to the formation of stable ring-like structures comprised of up to three additional reagents were identified. Based on past findings, these ring-like structures, Cy-BCN (**5** and **6**) were identified as potential products of experimental reactions of CO_2 and NH_3BH_3.[84–86] Figure 1.10 overviews the detailed reaction pathways generated via ZStruct driven reaction path finding. The rate-limiting step for **5** formation is reaction VII, the hydroboration step which has a transition state energy of 16.9 kcal/mol above **4**. Comparatively, concomitant proton

transfer to carbon and N-B dative bond formation in reaction XVI has a limiting transition state energy of 19.1 kcal/mol (referenced to **4**) along the lowest energy path for **6** formation. The comparison between rate limiting barriers suggests that the less stable form of Cy-BCN, **5**, is kinetically favored despite being less thermodynamically stable. The transformation of **5** to **6**, however, is possible through decomposition of **5** followed by paths X through XVI (shown in black, Figure 1.10).

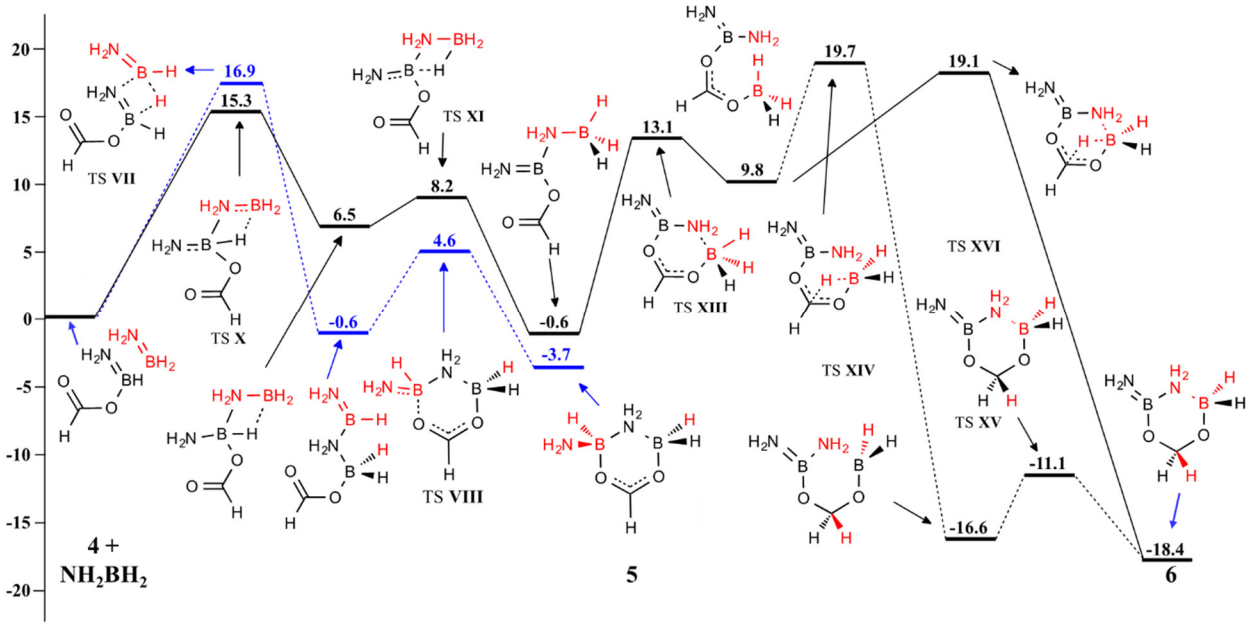

Figure 1.10. Cy-BCN precursor formation from **4** and NH_2BH_2. The blue and black paths indicate the most favorable paths for **5** and **6** formation, respectively.

ZStruct enabled the identification of two specific six-membered ring (Cy-BCN) structures from AB and CO_2 by detailing key elementary reactions. These reactions comprise part of the potential energy surface for the AB/CO_2 reaction network and form a foundation for the eventual formation of BCN from AB and CO_2. Furthermore, reactivity patterns, such as the importance of B-O bond formation were extracted from the thermodynamic and kinetic reaction data, providing an overview of trends in reactivity for AB and CO_2. This work outlines the broad scope of reactivity sampled by ZStruct and provides a starting point for application of ZStruct to more structurally complex transition metal complexes. Chapter 2 details applications of the ZStruct program to the resolution of reaction networks for reductive elimination from palladium (IV).

In general, reaction path finding using automated transition state searches provides a means to computationally resolve chemical mechanisms. These mechanisms provide the relevant features of the potential energy surface that correspond to reaction prediction. This information provides the crucial first step to resolving the computational reaction landscape. The next section introduces the relevant background on addressing how the potential energy surface changes as a function of atomistic changes to the molecules of interest.

1.4 Constructing the Reaction Landscape

Once a mechanism is known, computational tools can also probe the effects of steric and electronic contributions to the reactivity, often more easily than experimental investigations. Stepwise structural modification is trivial, allowing data mining approaches obtained from analysis of stationary points to develop a quantitative structure activity relationship (QSAR). The reaction path for a particular process often varies predictably as stereoelectronic contributions to the reactive atoms are modulated. The prototypical example of this is an Evans-Polanyi principle. In Evans-Polanyi, the reaction barriers for similar chemical reaction can be estimated, and often quantified, based on measuring differences in the enthalpy of reaction (Equation 1.3).

$$E_a = E_0 + \alpha \Delta H$$

Equation 1.3 Evans-Polanyi principle relating the activation barrier of a reaction to the difference in enthalpy of reaction.

In equation 1.3 E_a is the activation barrier of a reaction from the same class of reactivity, (i.e. both are examples of a particular named reaction), ΔH is the enthalpy of reaction, and α characterize the position of the transition state (early to late). Even though the relationship is a generalization, the ability to cluster similar types of reactivity has been fundamental in expert encoded PES investigation tools mentioned previously.[11–26]

More generally, human intuition has proven to be a powerful tool in the design of new types of reactivity. Interpreting the structure-energy correspondence between similar types of reactivity often improves human understanding in the process. To accomplish this, discrete reactions, varied by molecular structure modifications, can be related through a descriptive model equation (Figure 1.11).

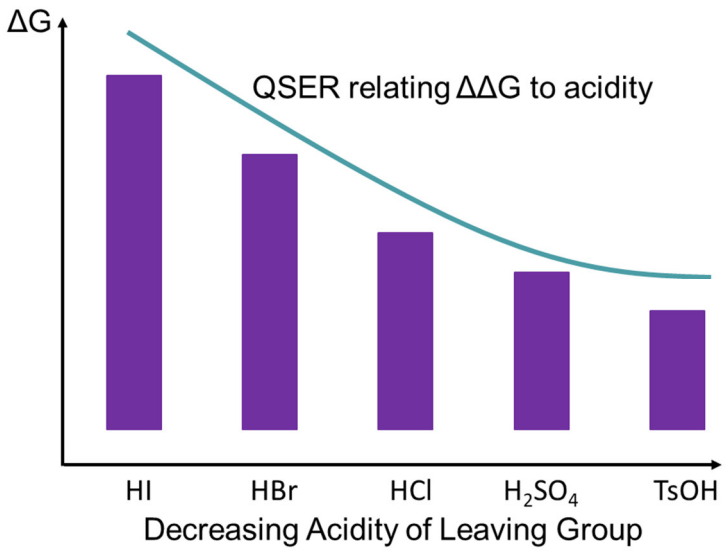

Figure 1.11 Illustration of QSER for five example SN_2 leaving groups and the effect on the free energy of reaction.

Functions can be developed to describe Evans-Polanyi-like relationships targeting activation barriers, or more broadly to predict other thermodynamic or kinetic properties from systematic structural changes. Automated structure generation can be used to generate libraries of test reactions which can aid in the development of QSAR to generalize a single potential energy surface to include entire classes of reactivity. Toward this goal, chapter 3 discuss development of thermodynamic landscapes and the structure-energy descriptors of cobalt catalyzed CO_2 reduction.

The background concepts required to explain reaction landscapes has been reviewed. The following provides a brief outline of the rest of this dissertation, Chapters discussing the application of computational tools toward the resolution of reaction landscapes will be presented.

1.4 Dissertation Outline

In Chapter 1, a brief background on the necessary tools for investigating PESs and reaction landscapes was presented. The following chapters will apply these tools to main group and organometallic chemistry targeting the systematic evaluation of PESs and QSAR.

Chapter 2 demonstrates the application of ZStruct to a combined experimental and computational investigation of reductive elimination from palladium(IV). Development of non-intuitive reaction pathways for $C(sp^3)$-N reductive elimination will be covered as well as specific substrates which favor $C(sp^2)$-$C(sp^3)$ reductive elimination.

Chapter 3 will cover the development of a thermodynamic landscape using modified versions of the ZStruct program to design catalyst libraries. Discussion of statistical modeling techniques for QSAR and reaction landscape development.

Chapter 4 will include Final Remarks, in which the findings from previous studies are reviewed as well as the scope and limitations of these works.

1.6 References

(1) Becke, A. D. Perspective: Fifty Years of Density-Functional Theory in Chemical Physics. *J. Chem. Phys.* **2014**, *140* (18), 18A301.

(2) Burke, K. Perspective on Density Functional Theory. *J. Chem. Phys.* **2012**, *136* (15), 150901.

(3) Schlegel, H. B. Exploring Potential Energy Surfaces for Chemical Reactions: An Overview of Some Practical Methods. *J. Comput. Chem.* **2003**, *24*, 1514–1527.

(4) Wales, D. J. Energy Landscapes: Calculating Pathways and Rates. *Int. Rev. Phys. Chem.* **2006**, *25* (1–2), 237–282.

(5) Schlegel, H. B. Geometry Optimization. *Wiley Interdiscip. Rev. Comput. Mol. Sci.* **2011**, *1* (5), 790–809.

(6) Schlegel, H. B. Geometry Optimization. *Wiley Interdiscip. Rev. Comput. Mol. Sci.* **2011**, *1* (5), 790–809.

(7) Schlegel, H. B. Exploring Potential Energy Surfaces for Chemical Reactions: An Overview of Some Practical Methods. *J. Comput. Chem.* **2003**, *24* (12), 1514–1527.

(8) Jackson, K.; Jaffar, S. K.; Paton, R. S. Computational Organic Chemistry. *Annu. Reports Sect. "B" (Organic Chem.* **2013**, *109*, 235.

(9) Sperger, T.; Sanhueza, I. A.; Kalvet, I.; Schoenebeck, F. Computational Studies of Synthetically Relevant Homogeneous Organometallic Catalysis Involving Ni, Pd, Ir, and Rh: An Overview of Commonly Employed DFT Methods and Mechanistic Insights. *Chem. Rev.* **2015**, *115* (17), 9532–9586.

(10) Bell, A. T.; Head-Gordon, M. Quantum Mechanical Modeling of Catalytic Processes. *Annu. Rev. Chem. Biomol. Eng.* **2011**, *2* (1), 453–477.

(11) Van Geem, K. M.; Reyniers, M.-F.; Marin, G. B.; Song, J.; Green, W. H.; Matheu, D. M. Automatic Reaction Network Generation Using RMG for Steam Cracking of N-Hexane. *AIChE J.* **2006**, *52* (2), 718–730.

(12) Rappoport, D.; Galvin, C. J.; Zubarev, D. Y.; Aspuru-Guzik, A. Complex Chemical Reaction Networks from Heuristics-Aided Quantum Chemistry. *J. Chem. Theory Comput.* **2014**, *10* (3), 897–907.

(13) Harper, M. R.; Van Geem, K. M.; Pyl, S. P.; Marin, G. B.; Green, W. H. Comprehensive Reaction Mechanism for N-Butanol Pyrolysis and Combustion. *Combust. Flame* **2011**, *158* (1), 16–41.

(14) Broadbelt, L. J.; Stark, S. M.; Klein, M. T. Computer Generated Pyrolysis Modeling: On-the-Fly Generation of Species, Reactions, and Rates. *Ind. Eng. Chem. Res.* **1994**, *33* (4), 790–799.

(15) Broadbelt, L. J.; Stark, S. M.; Klein, M. T. Computer Generated Reaction Modelling:

Decomposition and Encoding Algorithms for Determining Species Uniqueness. *Comput. Chem. Eng.* **1996**, *20* (2), 113–129.

(16) Klinke II, D. J.; Broadbelt, L. J. Construction of a Mechanistic Model of Fischer–Tropsch Synthesis on Ni(1 1 1) and Co(0 0 0 1) Surfaces. *Chem. Eng. Sci.* **1999**, *54* (15–16), 3379–3389.

(17) Appayee, C.; Breslow, R. Deuterium Studies Reveal a New Mechanism for the Formose Reaction Involving Hydride Shifts. *J. Am. Chem. Soc.* **2014**, *136* (10), 3720–3723.

(18) Seyedzadeh Khanshan, F.; West, R. H. Developing Detailed Kinetic Models of Syngas Production from Bio-Oil Gasification Using Reaction Mechanism Generator (RMG). *Fuel* **2016**, *163*, 25–33.

(19) Slakman, B. L.; Simka, H.; Reddy, H.; West, R. H. Extending Reaction Mechanism Generator to Silicon Hydride Chemistry. *Ind. Eng. Chem. Res.* **2016**, *55* (49), 12507–12515.

(20) Broadbelt, L. J.; Pfaendtner, J. Lexicography of Kinetic Modeling of Complex Reaction Networks. *AIChE J.* **2005**, *51* (8), 2112–2121.

(21) Petway, S. V.; Ismail, H.; Green, W. H.; Estupiñán, E. G.; Jusinski, L. E.; Taatjes, C. A. Measurements and Automated Mechanism Generation Modeling of OH Production in Photolytically Initiated Oxidation of the Neopentyl Radical ǁ. *J. Phys. Chem. A* **2007**, *111* (19), 3891–3900.

(22) Matheu, D. M.; Dean, A. M.; Grenda, J. M.; Green, W. H. Mechanism Generation with Integrated Pressure Dependence: A New Model for Methane Pyrolysis. *J. Phys. Chem. A* **2003**, *107* (41), 8552–8565.

(23) Gao, C. W.; Allen, J. W.; Green, W. H.; West, R. H. Reaction Mechanism Generator: Automatic Construction of Chemical Kinetic Mechanisms. *Comput. Phys. Commun.* **2016**, *203*, 212–225.

(24) Mizuno, T.; Weiss, A. H. Synthesis and Utilization of Formose Sugars; 1974; pp 173–227.

(25) Broadbelt, L. J.; Stark, S. M.; Klein, M. T. Termination of Computer-Generated Reaction Mechanisms: Species Rank-Based Convergence Criterion. *Ind. Eng. Chem. Res.* **1995**, *34* (8), 2566–2573.

(26) Hansen, N.; Merchant, S. S.; Harper, M. R.; Green, W. H. The Predictive Capability of an Automatically Generated Combustion Chemistry Mechanism: Chemical Structures of Premixed Iso-Butanol Flames. *Combust. Flame* **2013**, *160* (11), 2343–2351.

(27) Varela, J. A.; Vázquez, S. A.; Martínez-Núñez, E. An Automated Method to Find Reaction Mechanisms and Solve the Kinetics in Organometallic Catalysis. *Chem. Sci.* **2017**, *8* (5), 3843–3851.

(28) Martínez-Núñez, E. An Automated Method to Find Transition States Using Chemical Dynamics Simulations. *J. Comput. Chem.* **2015**, *36* (4), 222–234.

(29) Martínez-Núñez, E. An Automated Transition State Search Using Classical Trajectories Initialized at Multiple Minima. *Phys. Chem. Chem. Phys.* **2015**, *17* (22), 14912–14921.

(30) Maeda, S.; Harabuchi, Y.; Takagi, M.; Taketsugu, T.; Morokuma, K. Artificial Force Induced Reaction (AFIR) Method for Exploring Quantum Chemical Potential Energy Surfaces. *Chem. Rec.* **2016**, *16* (5), 2232–2248.

(31) Bhoorasingh, P. L.; Slakman, B. L.; Seyedzadeh Khanshan, F.; Cain, J. Y.; West, R. H. Automated Transition State Theory Calculations for High-Throughput Kinetics. *J. Phys. Chem. A* **2017**, *121* (37), 6896–6904.

(32) Cohen, A. J.; Mori-Sánchez, P.; Yang, W. Challenges for Density Functional Theory. *Chem. Rev.* **2012**, *112* (1), 289–320.

(33) Hebrard, F.; Kalck, P. Cobalt-Catalyzed Hydroformylation of Alkenes: Generation and Recycling of the Carbonyl Species, and Catalytic Cycle. *Chem. Rev.* **2009**, *109* (9), 4272–4282.

(34) Maeda, S.; Morokuma, K. Communications: A Systematic Method for Locating Transition Structures of A+B→X Type Reactions. *J. Chem. Phys.* **2010**, *132* (24), 241102.

(35) Maeda, S.; Taketsugu, T.; Morokuma, K. Exploring Transition State Structures for Intramolecular Pathways by the Artificial Force Induced Reaction Method. *J. Comput. Chem.* **2014**, *35* (2), 166–173.

(36) Maeda, S.; Morokuma, K. Finding Reaction Pathways of Type A + B → X: Toward Systematic Prediction of Reaction Mechanisms. *J. Chem. Theory Comput.* **2011**, *7* (8), 2335–2345.

(37) Maeda, S.; Ohno, K. Global Mapping of Equilibrium and Transition Structures on Potential Energy Surfaces by the Scaled Hypersphere Search Method: Applications to Ab Initio Surfaces of Formaldehyde and Propyne Molecules. *J. Phys. Chem. A* **2005**, *109* (25), 5742–5753.

(38) Ohno, K.; Maeda, S. Global Reaction Route Mapping on Potential Energy Surfaces of Formaldehyde, Formic Acid, and Their Metal-Substituted Analogues. *J. Phys. Chem. A* **2006**, *110* (28), 8933–8941.

(39) Vázquez, S. A.; Martínez-Núñez, E. HCN Elimination from Vinyl Cyanide: Product Energy Partitioning, the Role of Hydrogen–deuterium Exchange Reactions and a New Pathway. *Phys. Chem. Chem. Phys.* **2015**, *17* (10), 6948–6955.

(40) Maeda, S.; Ohno, K.; Morokuma, K. Systematic Exploration of the Mechanism of Chemical Reactions: The Global Reaction Route Mapping (GRRM) Strategy Using the ADDF and AFIR Methods. *Phys. Chem. Chem. Phys.* **2013**, *15* (11), 3683.

(41) Puripat, M.; Ramozzi, R.; Hatanaka, M.; Parasuk, W.; Parasuk, V.; Morokuma, K. The Biginelli Reaction Is a Urea-Catalyzed Organocatalytic Multicomponent Reaction. *J. Org. Chem.* **2015**, *80* (14), 6959–6967.

(42) Bhoorasingh, P. L.; West, R. H. Transition State Geometry Prediction Using Molecular Group Contributions. *Phys. Chem. Chem. Phys.* **2015**, *17* (48), 32173–32182.

(43) Zimmerman, P. M. Automated Discovery of Chemically Reasonable Elementary Reaction Steps. *J. Comput. Chem.* **2013**, *34* (16), 1385–1392.

(44) Suleimanov, Y. V.; Green, W. H. Automated Discovery of Elementary Chemical Reaction Steps Using Freezing String and Berny Optimization Methods. *J. Chem. Theory Comput.* **2015**, *11* (9), 4248–4259.

(45) Habershon, S. Automated Prediction of Catalytic Mechanism and Rate Law Using Graph-Based Reaction Path Sampling. *J. Chem. Theory Comput.* **2016**, *12* (4), 1786–1798.

(46) Wang, L.-P.; Titov, A.; McGibbon, R.; Liu, F.; Pande, V. S.; Martínez, T. J. Discovering Chemistry with an Ab Initio Nanoreactor. *Nat. Chem.* **2014**, *6* (12), 1044–1048.

(47) Bergeler, M.; Simm, G. N.; Proppe, J.; Reiher, M. Heuristics-Guided Exploration of Reaction Mechanisms. *J. Chem. Theory Comput.* **2015**, *11* (12), 5712–5722.

(48) Nett, A. J.; Zhao, W.; Zimmerman, P. M.; Montgomery, J. Highly Active Nickel Catalysts for C–H Functionalization Identified through Analysis of Off-Cycle Intermediates. *J. Am. Chem. Soc.* **2015**, *137* (24), 7636–7639.

(49) Zimmerman, P. M. Navigating Molecular Space for Reaction Mechanisms: An Efficient, Automated Procedure. *Mol. Simul.* **2015**, *41* (1–3), 43–54.

(50) Habershon, S. Sampling Reactive Pathways with Random Walks in Chemical Space: Applications to Molecular Dissociation and Catalysis. *J. Chem. Phys.* **2015**, *143* (9), 94106.

(51) Ellington, B. R.; Paul, B.; Das, D.; Vitek, A. K.; Zimmerman, P. M.; Marsh, E. N. G. An Unusual Iron-Dependent Oxidative Deformylation Reaction Providing Insight into Hydrocarbon Biosynthesis in Nature. *ACS Catal.* **2016**, *6* (5), 3293–3300.

(52) Yang, M.; Zou, J.; Wang, G.; Li, S. Automatic Reaction Pathway Search via Combined Molecular Dynamics and Coordinate Driving Method. *J. Phys. Chem. A* **2017**, *121* (6), 1351–1361.

(53) Dewyer, A. L.; Zimmerman, P. M. Finding Reaction Mechanisms, Intuitive or Otherwise. *Org. Biomol. Chem.* **2017**, *15* (3), 501–504.

(54) Smith, M. L.; Leone, A. K.; Zimmerman, P. M.; McNeil, A. J. Impact of Preferential π-Binding in Catalyst-Transfer Polycondensation of Thiazole Derivatives. *ACS Macro Lett.* **2016**, *5* (12), 1411–1415.

(55) Ludwig, J. R.; Zimmerman, P. M.; Gianino, J. B.; Schindler, C. S. Iron(III)-Catalysed Carbonyl–olefin Metathesis. *Nature* **2016**, *533* (7603), 374–379.

(56) Ludwig, J. R.; Phan, S.; McAtee, C. C.; Zimmerman, P. M.; Devery, J. J.; Schindler, C. S. Mechanistic Investigations of the Iron(III)-Catalyzed Carbonyl-Olefin Metathesis

Reaction. *J. Am. Chem. Soc.* **2017**, *139* (31), 10832–10842.

(57) Dewyer, A. L.; Zimmerman, P. M. Simulated Mechanism for Palladium-Catalyzed, Directed γ-Arylation of Piperidine. *ACS Catal.* **2017**, *7* (8), 5466–5477.

(58) Hale, L. V. A.; Malakar, T.; Tseng, K.-N. T.; Zimmerman, P. M.; Paul, A.; Szymczak, N. K. The Mechanism of Acceptorless Amine Double Dehydrogenation by N,N,N -Amide Ruthenium(II) Hydrides: A Combined Experimental and Computational Study. *ACS Catal.* **2016**, *6* (8), 4799–4813.

(59) Maragakis, P.; Andreev, S. A.; Brumer, Y.; Reichman, D. R.; Kaxiras, E. Adaptive Nudged Elastic Band Approach for Transition State Calculation. *J. Chem. Phys.* **2002**, *117* (10), 4651–4658.

(60) Ayala, P. Y.; Schlegel, H. B. A Combined Method for Determining Reaction Paths, Minima, and Transition State Geometries. *J. Chem. Phys.* **1997**, *107* (2), 375–384.

(61) Fischer, S.; Karplus, M. Conjugate Peak Refinement: An Algorithm for Finding Reaction Paths and Accurate Transition States in Systems with Many Degrees of Freedom. *Chem. Phys. Lett.* **1992**, *194* (3), 252–261.

(62) Henkelman, G.; Jónsson, H. Improved Tangent Estimate in the Nudged Elastic Band Method for Finding Minimum Energy Paths and Saddle Points. *J. Chem. Phys.* **2000**, *113* (22), 9978–9985.

(63) Dellago, C.; Bolhuis, P. G.; Geissler, P. L. Transition Path Sampling. In *Advances in Chemical Physics*; John Wiley & Sons, Inc.: Hoboken, NJ, USA; pp 1–78.

(64) Henkelman, G.; Jónsson, H. A Dimer Method for Finding Saddle Points on High Dimensional Potential Surfaces Using Only First Derivatives. *J. Chem. Phys.* **1999**, *111* (15), 7010–7022.

(65) Baker, J. An Algorithm for the Location of Transition States. *J. Comput. Chem.* **1986**, *7* (4), 385–395.

(66) Banerjee, A.; Adams, N.; Simons, J.; Shepard, R. Search for Stationary Points on Surfaces. *J. Phys. Chem.* **1985**, *89* (1), 52–57.

(67) Cerjan, C. J.; Miller, W. H. On Finding Transition States. *J. Chem. Phys.* **1981**, *75* (6), 2800–2806.

(68) Ionova, I. V.; Carter, E. A. Ridge Method for Finding Saddle Points on Potential Energy Surfaces. *J. Chem. Phys.* **1993**, *98* (8), 6377–6386.

(69) Elber, R.; Karplus, M. A Method for Determining Reaction Paths in Large Molecules: Application to Myoglobin. *Chem. Phys. Lett.* **1987**, *139* (5), 375–380.

(70) Dewar, M. J. S.; Healy, E. F.; Stewart, J. J. P. Location of Transition States in Reaction Mechanisms. *J. Chem. Soc. Faraday Trans. 2* **1984**, *80* (3), 227.

(71) Muller, K.; Brown, L. D. Location of Saddle Points and Minimum Energy Paths by a Constrained Simplex Optimization Procedure. *Theor. Chim. Acta* **1979**, *53* (1), 75–93.

(72) Halgren, T. A.; Lipscomb, W. N. The Synchronous-Transit Method for Determining Reaction Pathways and Locating Molecular Transition States. *Chem. Phys. Lett.* **1977**, *49* (2), 225–232.

(73) Zimmerman, P. Reliable Transition State Searches Integrated with the Growing String Method. *J. Chem. Theory Comput.* **2013**, *9* (7), 3043–3050.

(74) Zimmerman, P. M. Growing String Method with Interpolation and Optimization in Internal Coordinates: Method and Examples. *J. Chem. Phys.* **2013**, *138* (18), 184102.

(75) Peters, B.; Heyden, A.; Bell, A. T.; Chakraborty, A. A Growing String Method for Determining Transition States: Comparison to the Nudged Elastic Band and String Methods. *J. Chem. Phys.* **2004**, *120* (17), 7877–7886.

(76) E, W.; Ren, W.; Vanden-Eijnden, E. Finite Temperature String Method for the Study of Rare Events †. *J. Phys. Chem. B* **2005**, *109* (14), 6688–6693.

(77) E, W.; Ren, W.; Vanden-Eijnden, E. String Method for the Study of Rare Events. *Phys. Rev. B* **2002**, *66* (5), 52301.

(78) Zimmerman, P. M. Single-Ended Transition State Finding with the Growing String Method. *J. Comput. Chem.* **2015**, *36* (9), 601–611.

(79) Schlegel, H. B. *Geometry Optimization on Potential Energy Surfaces*; World Scientific Publishing: Singapore, 1995.

(80) Maeda, S.; Harabuchi, Y.; Ono, Y.; Taketsugu, T.; Morokuma, K. Intrinsic Reaction Coordinate: Calculation, Bifurcation, and Automated Search. *Int. J. Quantum Chem.* **2015**, *115* (5), 258–269.

(81) Fukui, K. The Path of Chemical Reactions - the IRC Approach. *Acc. Chem. Res.* **1981**, *14* (12), 363–368.

(82) Henkelman, G.; Uberuaga, B. P.; Jónsson, H. A Climbing Image Nudged Elastic Band Method for Finding Saddle Points and Minimum Energy Paths. *J. Chem. Phys.* **2000**, *113* (22), 9901–9904.

(83) Trygubenko, S. A.; Wales, D. J. A Doubly Nudged Elastic Band Method for Finding Transition States. *J. Chem. Phys.* **2004**, *120* (5), 2082–2094.

(84) Byeon, A.; Lee, J. W. Electrocatalytic Activity of BN Codoped Graphene Oxide Derived from Carbon Dioxide. *J. Phys. Chem. C* **2013**, *117* (46), 24167–24173.

(85) Xiong, R.; Li, X.; Byeon, A.; Lee, J. W. Production of Nitrogen-Doped Graphite from Carbon Dioxide Using Polyaminoborane. *RSC Adv.* **2013**, *3* (48), 25752.

(86) Zhang, J.; Byeon, A.; Lee, J. W. Boron-Doped Electrocatalysts Derived from Carbon Dioxide. *J. Mater. Chem. A* **2013**, *1* (30), 8665.

(87) Roy, L.; Zimmerman, P. M.; Paul, A. Changing Lanes from Concerted to Stepwise Hydrogenation: The Reduction Mechanism of Frustrated Lewis Acid-Base Pair Trapped CO2 to Methanol by Ammonia-Borane. *Chem. - A Eur. J.* **2011**, *17* (2), 435–439.

(88) Zimmerman, P. M.; Zhang, Z.; Musgrave, C. B. Simultaneous Two-Hydrogen Transfer as a Mechanism for Efficient CO 2 Reduction. *Inorg. Chem.* **2010**, *49* (19), 8724–8728.

Chapter 2: Reactivity and Mechanism in C(sp^3)–N Bond-Forming Reductive Elimination from Palladium(IV)

This chapter is largely based upon published work:
Reproduced with permission from Pendleton, I. M.; Pérez-Temprano, M. H.; Sanford, M. S.; Zimmerman, P. M. Experimental and Computational Assessment of Reactivity and Mechanism in C(sp^3)–N Bond-Forming Reductive Elimination from Palladium(IV). *J. Am. Chem. Soc.* **2016**, *138* (18), 6049–6060.

2.1 Abstract

This report describes a combined experimental and computational investigation of the mechanism of C(sp^3)–N bond-forming reductive elimination from sulfonamide-ligated Pd^{IV} complexes. After an initial experimental assessment of reactivity, we used ZStruct, a computational combinatorial reaction finding method, to analyze a large number of multistep mechanisms for this process. This study reveals two facile isomerization pathways connecting the experimentally observed Pd^{IV} isomers, along with two competing S_N2 pathways for C(sp^3)–N coupling. One of these pathways involves an unanticipated oxygen-nitrogen exchange of the sulfonamide ligand prior to an inner-sphere S_N2-type reductive elimination. The calculated $\Delta G^{\ddagger}$ values for isomerization and reductive elimination with a series of sulfonamide derivatives are in good agreement with experimental data. Furthermore, the simulations predict relative reaction rates with different sulfonamides, which is successful only after considering competition between the proposed operating mechanisms. Overall, this work shows that the combination of experimental studies and new computational tools can provide fundamental mechanistic insights into complex organometallic reaction pathways.

2.2 Introduction

Over the past decade, Pd-catalyzed C(sp^3)–N bond forming reactions (involving both C–H amination and oxidative amination of alkenes) have emerged as valuable methods in organic

synthesis.[1,2] Although high-valent palladium complexes have been proposed as intermediates in these transformations, a detailed mechanistic understanding of the key C(sp^3)–N bond-forming step has remained largely elusive.[3,4] Recently, we isolated a Pd^{IV} model complex, $\mathbf{1_{Ts}}$, that undergoes selective C(sp^3)–N coupling (Figure 2.1).[5] This work was the first example of C(sp^3)–N bond-forming reductive elimination from a well-defined Pd^{IV} complex.[6]

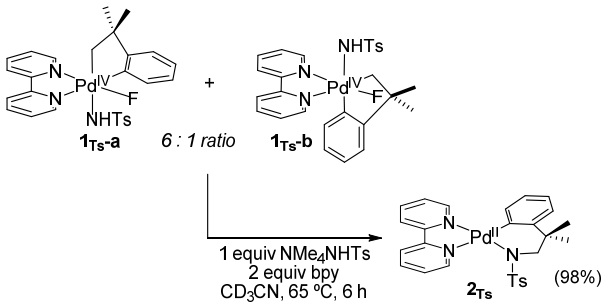

Figure 2.1. C(sp^3)–N Bond-Forming Reductive Elimination from 1_{Ts}

A detailed mechanistic understanding of this C(sp^3)–N coupling process would provide valuable information about relative rates, ligand design, and stereochemistry that could ultimately inform new catalyst design and optimization. However, experimental mechanistic studies of reductive elimination from $\mathbf{1_{Ts}}$ are hampered by the complexity of this system. For example, two different isomers of this octahedral Pd^{IV} complex ($\mathbf{1_{Ts}}$**-a** and $\mathbf{1_{Ts}}$**-b**) are detectable, and others could be kinetically accessible under the reaction conditions. Furthermore, multiple kinetically indistinguishable reductive elimination pathways are possible from each of these isomers (*vide infra*).

The complexity of these competing reductive elimination pathways motivated us to pursue computational studies to gain a greater understanding of this transformation. We reasoned that this system would serve as an attractive test case for the ZStruct program, a new reaction-finding tool developed in the Zimmerman lab.[7] ZStruct enables a combinatorial exploration of reaction pathways originating from an initial species (Figure 2.2) and uses quantum chemistry to provide accurate analysis of the thermodynamic and kinetic factors that govern each path. The entire set of ZStruct-discovered reaction pathways are automatically characterized at the full level of detail and accuracy available to modern quantum chemical simulations of reaction mechanism. In comparison to a traditional DFT investigation, this method significantly expands the scope of reactivity and can reveal previously unknown mechanistic pathways. Importantly, the advantages

of this method must be balanced by its high computational cost relative to traditional DFT.[8] However, with the rapidly expanding availability of computational power, ZStruct and other modern reaction network discovery tools[9] are expected to become more and more economical for mechanistic investigations in years to come.

We report herein that combining experimental studies with ZStruct allowed us to unravel competing pathways for carbon-nitrogen bond-forming reductive elimination from complex $\mathbf{1}_{\mathbf{Ts}}$ and derivatives thereof. During these studies, ZStruct unveiled an unanticipated, alternative pathway for C(sp^3)–N coupling at Pd^{IV} alkyl sulfonamide complexes.

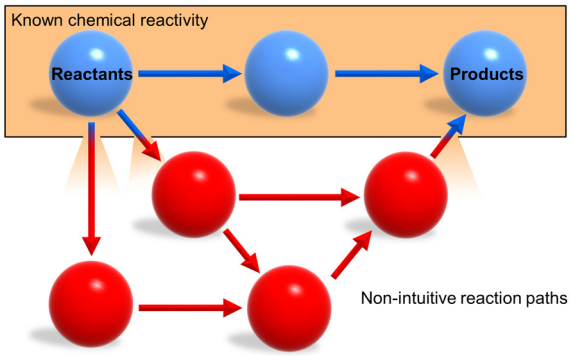

Figure 2.2 ZStruct mediated mechanism discovery incorporates known and non-intuitive chemical pathways.

This pathway, shown in **Figure 2.3**, is an inner-sphere, concerted reductive elimination via a 5-membered transition state that does not require pre-dissociation of the sulfonamide. Prior literature reports have shown that C(sp^3)–C(sp^2)[10] and C(sp^2)–X reductive elimination processes from high-valent group 10 complexes occur through concerted inner-sphere mechanisms, while C(sp^3)–heteroatom[11,12,13,14] couplings generally favor outer-sphere S_N2-type mechanisms. To our knowledge, concerted inner-sphere paths have not been previously implicated for C(sp^3)–N coupling.[15,16] However, as detailed below, in our system, it is necessary to invoke competing inner and outer-sphere C(sp^3)–N reductive elimination mechanisms to fully explain the experimental data. Overall, this work leverages a synergistic combination of experimental studies and ZStruct to obtain a detailed mechanistic picture of C(sp^3)–N bond-forming reductive elimination from $\mathbf{1}_{\mathbf{Ts}}$ and its analogues.

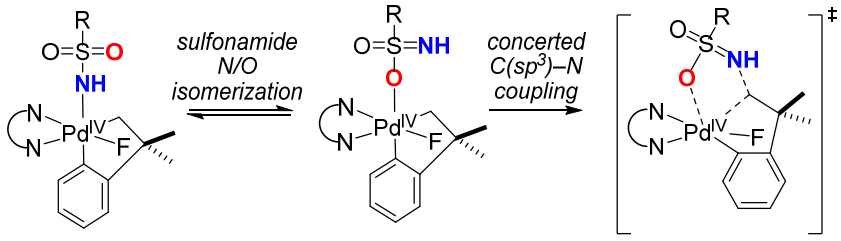

Figure 2.3 New Pathway for C(sp^3)–N Reductive Elimination of Sulfonamide Substrates Discovered by ZStruct

2.3 Results and Discussion

2.3.1 Possible Mechanisms for C(sp^3)–N Reductive Elimination from Pd^{IV} Complexes. We initially considered 4 mechanisms for reductive elimination from Pd^{IV} complexes of general structure **1**. All of these mechanisms have significant precedent in the literature for other carbon-heteroatom bond-forming reductive elimination processes.[17,18,19,20]

The first possibility (pathway **Ia/b**) involves direct nucleophilic attack by exogeneous RNH^- on the six-coordinate Pd^{IV} starting complex. As shown in Figure 2.4, this encompasses two distinct processes, as it could occur from either isomer **1a** or isomer **1b**. The rate expression for each is expected to be similar and is shown in Figure 2.4.

Pathway **II** involves the dissociation of one arm of the bipyridine ligand to generate a neutral 5-coordinate intermediate, followed by concerted C–N reductive elimination via a traditional 3-membered transition state. This pathway is only possible for isomer **1b**, since the sulfonamide and σ-alkyl ligands are *trans* to one another in **1a**. Because Pd^{IV} complex **1b** is unsymmetrical, this pathway could involve two different neutral pentacoordinate Pd^{IV} intermediates.

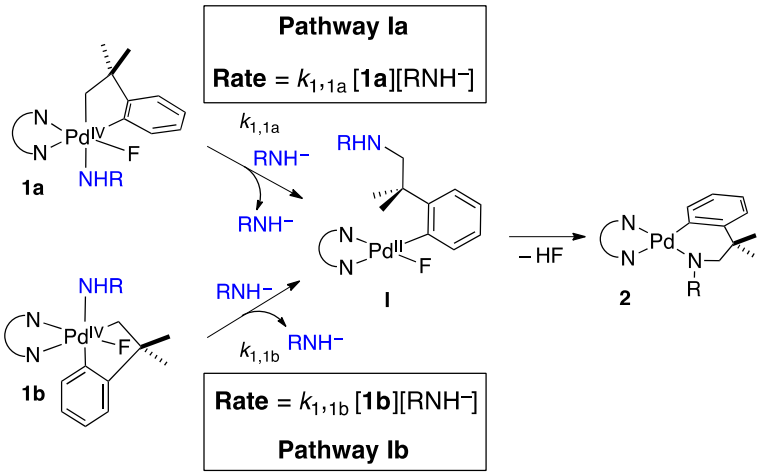

Figure 2.4 Pathway I: Direct Nucleophilic Attack

In these two-step mechanisms, either the ligand dissociation or C–N coupling could be the rate-determining step. The rate expression for each possibility is shown in Figure 2.5.

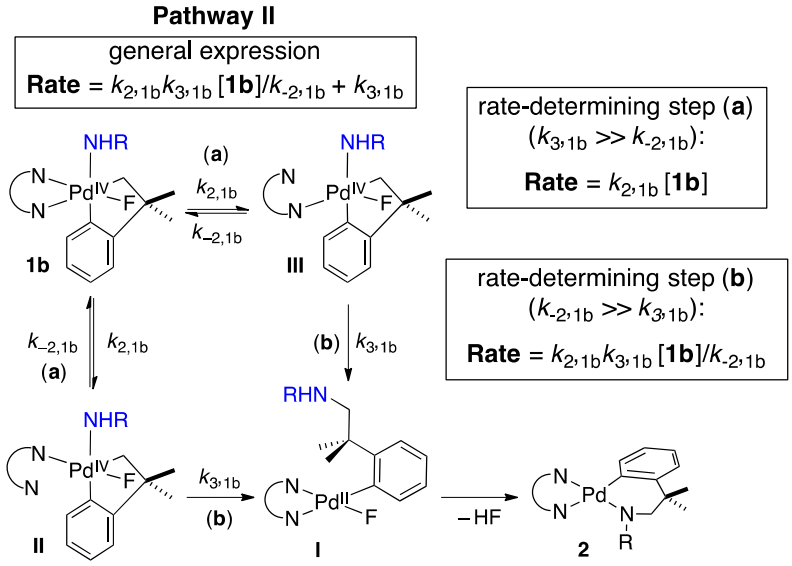

Figure 2.5 Pathway II: Bipyridine Ligand Dissociation

Pathway **III** proceeds via concerted C(sp^3)–N bond-forming reductive elimination (via a traditional 3-membered transition state) from the octahedral palladium center of **1b**. This pathway is not possible for **1a**, since the sulfonamide and σ-alkyl ligands are *trans* to one another in this isomer. This mechanism and the corresponding rate expression are shown Figure 2.6.

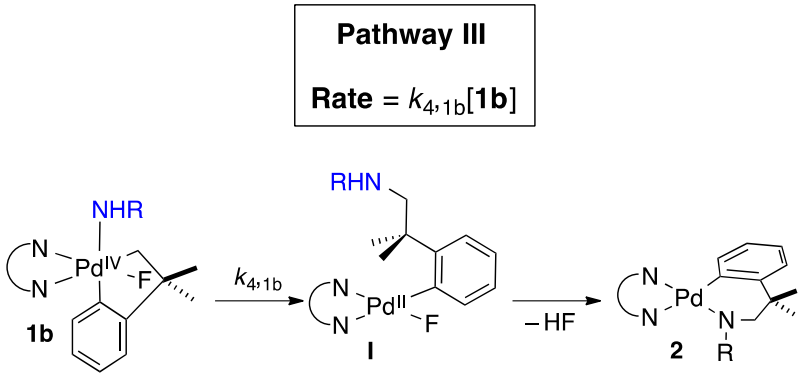

Figure 2.6 Pathway III: Concerted Reductive Elimination

Finally, pathway **IVa/b** involves two-steps: pre-equilibrium dissociation of RNH^- to afford a 5-coordinate cationic intermediate followed by S_N2-type attack of RNH^- on the Pd-σ-alkyl intermediate. As in the previous two-step mechanisms, either the ligand dissociation or the C–N coupling could be the rate-determining step. The rate expressions for each of these possibilities are shown in Figure 2.7.

2.3.2 Previous Studies of $\mathbf{1_{Ts}}$. Our initial communication provided preliminary mechanistic insights into C(sp^3)–N bond-forming reductive elimination from $\mathbf{1_{Ts}}$.[5] These studies showed that the reaction exhibits a first-order dependence on [$\mathbf{1_{Ts}}$] and zero-order dependence on [NMe_4NHTs]. These data unambiguously rule out pathway **I**, but do not allow us to differentiate between pathways **II-IV**. We also observed rapid exchange between free and Pd-bound $TsNH^-$ at temperatures significantly lower than those required for C(sp^3)–N coupling.[21] This indicates that the sulfonamide dissociation step of pathway **IV** is fast under our reaction conditions.

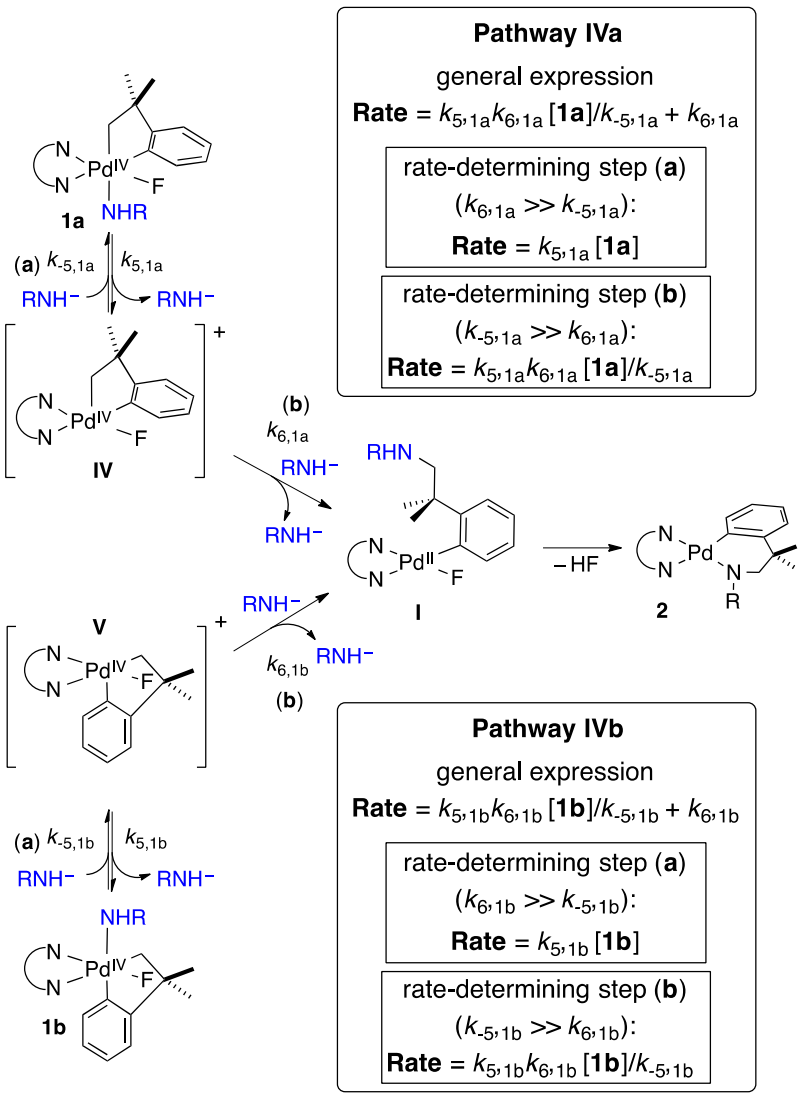

Figure 2.7. Pathway IV: S_N2 Pathway

2.4 Experimental Studies of C(sp^3)–N Coupling

2.4.1 Initial Screen of Sulfonamide Nucleophiles. Using the results with $\mathbf{1}_{Ts}$ as starting point, we first studied C(sp^3)–N bond-forming reductive elimination as a function of nucleophile with a series of sulfonamides.[22] The sulfonamides $CF_3SO_2NH^-$, $CF_2HSO_2NH^-$, and $CH_3SO_2NH^-$ were selected to represent a range of electronic properties (i.e., pK_a values). A fourth sulfonamide, $TsMeN^-$ was selected to alter the steric properties and hydrogen bond donor ability of the nucleophile, while maintaining similar pK_a to $TsNH^-$.

The concentrations of the Pd^{IV} starting materials and of the reductive elimination products were monitored via ^{1}H NMR spectroscopy. The rate constant ($k_{C\text{-}N}$) with each sulfonamide was determined by fitting the concentration versus time data to the kinetic model proposed in Figure 2

(rate = $k_{C\text{-}N}[\mathbf{1_R}]$). During the fitting of the kinetic data, the concentrations of $\mathbf{1_R}$**-a** and $\mathbf{1_R}$**-b** were added together and treated as a single Pd^{IV} complex. As summarized in Table 2.1, changing the steric and electronic properties of the sulfonamide had a significant impact on $k_{C–N}$. The fastest reaction was observed with the most electron deficient sulfonamide $CF_3SO_2NH^-$ ($k_{C–N}$ = 6.59 x 10^{-4} s^{-1}; entry 1). The slowest reactions were observed with $CH_3SO_2NH^-$ and $TsNH^-$, which react approximately 5-fold slower than $CF_3SO_2NH^-$ (1.65 x 10^{-4} s^{-1} and 1.43 x 10^{-4} s^{-1}, respectively). Previous studies of related $C(sp^3)$–O coupling reactions from Pt^{IV} complexes showed that electron deficient benzoate derivatives react significantly faster than electron rich derivatives (Hammett ρ value = +1.44 for this system). Based on this prior work, we anticipated that we might observe faster rates with more electron deficient sulfonamides (i.e., sulfonamides with lower pK_a values).[19e] While this general trend is observed in Table 2.1, entries 1-4, the disubstituted sulfonamide ($TsMeN^-$, entry 5) is a clear outlier. This latter sulfonamide has the highest pK_a value, but shows an unexpectedly fast rate.

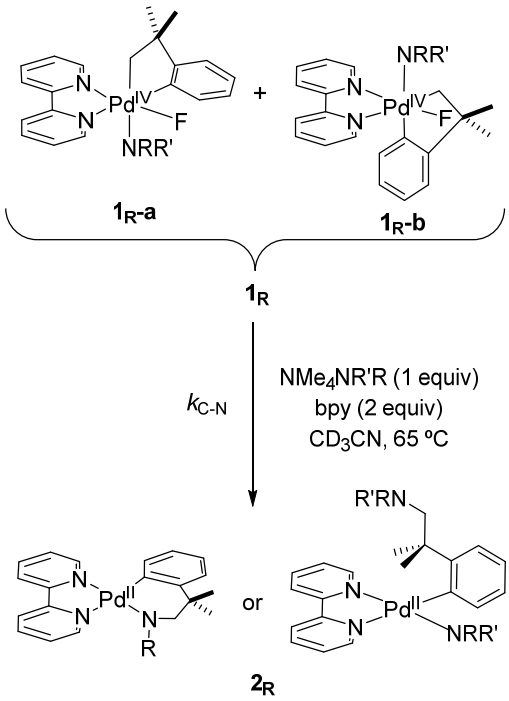

Entry	R	R'	pK_a[a]	$k_{C-N,65°C}$ (10^{-4} s^{-1})
1	CF_3SO_2 (Tf)	H	6.37	6.59
2	CF_2HSO_2	H	7.46	3.87
3	CH_3SO_2 (Ms)	H	10.87	1.65
4	p-tolylSO_2 (Ts)	H	10.26	1.43
5	p-tolylSO_2 (Ts)	Me	11.67	4.75

[a] pK_a values from the literature database of ACD/Laboratories Software version 11.02. All of the reported pK_a values are for the neutral sulfonamide (R_2NH).

Table 2.1. Reductive elimination reaction rate constant for C(sp^3)–N coupling using different sulfonamides.

2.4.2. C(sp^3)–N Reductive Elimination from 1_{Tf}, 1_{Ms} and 1_{TsNMe}. We next pursued more detailed investigations of the complexes containing $TfNH^-$, $MsNH^-$ and $TsMeN^-$. These were selected because: (1) they encompass the largest range of steric and electronic properties of the sulfonamides examined; (2) they are also among the fastest and slowest reacting; (3) they include the key outlier with respect to the initially expected pK_a trend ($TsMeN^-$); and (4) computational results suggest that a change in mechanism occurs between these nucleophiles (*vide infra*).

We established the kinetic orders of the C–N reductive elimination process in [Pd^{IV}] and [sulfonamide] for $\mathbf{1_{Tf}}$, $\mathbf{1_{Ms}}$ and $\mathbf{1_{TsNMe}}$. In all cases, these reactions exhibited a 1st order dependence on [Pd^{IV}][23] and a zero-order dependence on [sulfonamide].[24] As discussed above for $\mathbf{1_{Ts}}$, this data allows us to definitively rule out a direct S_N2 mechanism (pathway **I** in Figure 2.4), since this would exhibit a 1st order dependence on sulfonamide.[25]

We next explored the feasibility of pathway **II**, which involves pre-equilibrium de-chelation of the bipyridine ligand prior to C–N bond-formation. If dissociation of one of the nitrogen arms of the ligand were occurring, we would expect to see a large rate difference as a function of the rigidity of the bidentate ligand. To test this possibility, we synthesized complex $\mathbf{1'_{Tf}}$, in which the bipyridine is replaced with electronically similar but more rigid phenanthroline. As shown in Figure 2.8, the rate of reductive elimination from these two complexes under our optimal conditions was essentially identical ($k_{2,bpy}$ = 6.59 × 10^{-4} s^{-1} and $k_{2,phen}$ = 6.88 × 10^{-4} s^{-1}). This experiment provides preliminary evidence against the de-chelation mechanism.[26] Notably, the computational studies also strongly indicate against this mechanism (*vide infra*).

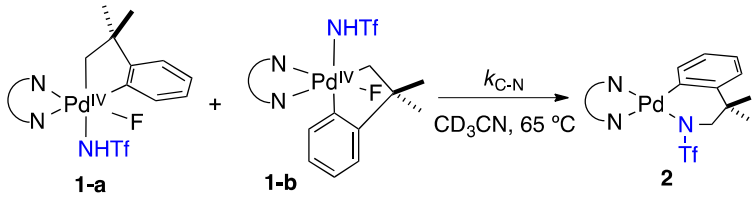

Ligand	Pd^{IV} Complex	k_{C-N}
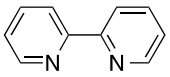	$\mathbf{1_{Tf}}$	6.59 × 10^{-4} s^{-1}
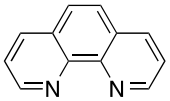	$\mathbf{1'_{Tf}}$	6.88 × 10^{-4} s^{-1}

Figure 2.8 Ligand Effects on the Rate of C(sp^3)–N Reductive Elimination

Eyring plots for C(sp^3)–N bond-forming reductive elimination from $\mathbf{1_{Tf}}$, $\mathbf{1_{Ms}}$ and $\mathbf{1_{TsNMe}}$ were obtained by monitoring the reaction rate over the temperature range of 50 ºC to 75 ºC. A representative plot is shown in Figure 2.9, and the activation parameters obtained from this analysis are provided in Table 2.2. The most noteworthy aspect of this data is the large differences in the entropy of activation between $\mathbf{1_{Ms}}$ and $\mathbf{1_{Tf}}$/$\mathbf{1_{TsNMe}}$. Specifically, the $\Delta S^{\ddagger}$ values for $\mathbf{1_{Tf}}$ and

$\mathbf{1}_{\mathbf{TsNMe}}$ are comparable to one another (-4.9 and -3.4 cal·K^{-1}·mol^{-1}, respectively) and are approximately 20 eu more positive than that for the reductive elimination from $\mathbf{1}_{\mathbf{Ms}}$.

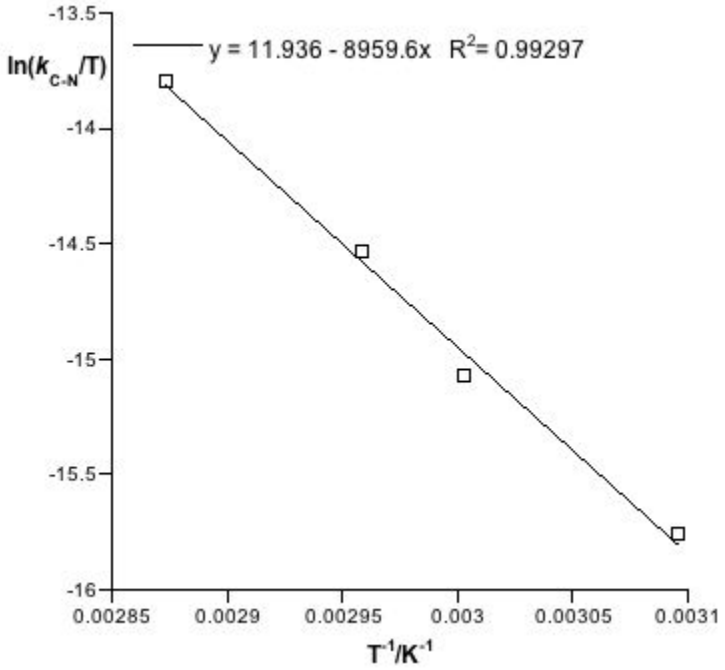

Figure 2.9 Eyring plot for determination of $\Delta H^{\ddagger}$ and $\Delta S^{\ddagger}$ for the C(sp^3)–N reductive elimination from $\mathbf{1}_{\mathbf{Ms}}$.

	TfNH$^-$	MsNH$^-$	TsMeN$^-$
$\Delta H^{\ddagger}$ [1]	23.2	17.8	23.8
$\Delta S^{\ddagger}$ [2]	–4.9	–23.5	–3.4
$\Delta G^{\ddagger}_{65°C}$ [1]	24.8	25.7	25.0

[1] kcal·mol^{-1}; [2] cal/mol·K

Table 2.2 Activation parameters for the C (sp^3)–N bond forming reaction.

This preliminarily suggests that different reductive elimination pathways might be operating upon variation of the sulfonamide (a proposal that is supported by computation, *vide infra*).

2.4.3 Lability of the sulfonamide ligand in $\mathbf{1_{Tf}}$, $\mathbf{1_{Ms}}$ and $\mathbf{1_{TsNMe}}$. We next examined the lability of the sulfonamide ligand in these complexes. The treatment of **1_{Ms}-a**/**1_{Ms}-b** with 1.2 equiv of NMe_4NHTs at room temperature resulted in fast sulfonamide exchange to form an equilibrium mixture of $\mathbf{1_{Ms}}$ and $\mathbf{1_{Ts}}$. Similar fast exchange was observed upon treatment of **1_{TsNMe}-a**/**1_{TsNMe}-b** with 1.2 equiv of NMe_4NHTs at room temperature. For a solution of **1_{Tf}-a** and 3.0 equiv of NMe_4TfNH, EXSY NMR studies at 20 ºC show fast exchange between free and bound $TfNH^-$. Overall, these results are similar to those obtained with $\mathbf{1_{Ts}}$, and they demonstrate that: (1) sulfonamide dissociation pathways (e.g., pathway **IV**) are kinetically feasible and (2) sulfonamide dissociation is not the rate-limiting step of the C–N coupling process.

2.4.4 1-a/1-b Isomerization Process. We hypothesized that the differences in reductive elimination rates/mechanism between $\mathbf{1_{Tf}}$, $\mathbf{1_{Ms}}$ and $\mathbf{1_{TsNMe}}$ might be related to the accessibility and/or reactivity of different Pd^{IV} isomers. As such, we conducted a detailed study of the isomerization process. Under our reaction conditions, all of these complexes exist as a mixture of two isomers: **1_R-a** and **1_R-b**.[5] However, isomer **1_R-a** can be formed in quantitative yield via the room temperature reaction of complex **3** with NMe_4NR in CD_3CN, and it then undergoes slow isomerization to form an equilibrium mixture of **1_R-a**/**1_R-b** at room temperature (Figure 2.10).[27] This isomerization is significantly faster than reductive elimination, and none of the C–N coupled product is detected over the time frame of isomer equilibration.

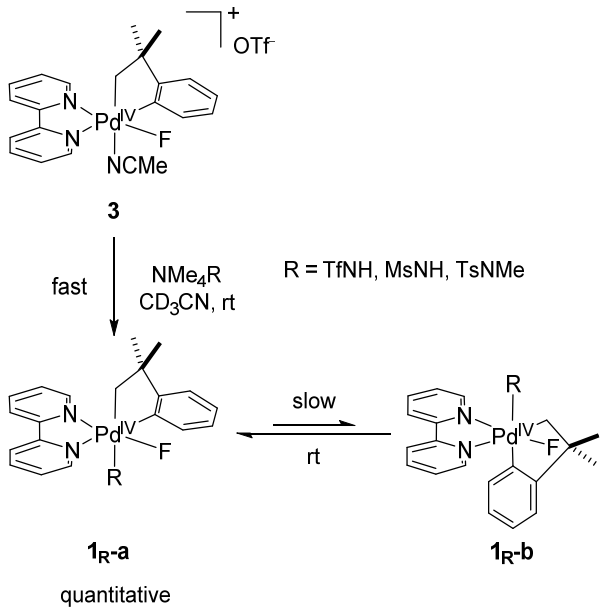

Figure 2.10. 1_R-a/1_R-b isomerization

We obtained the rate and equilibrium constant for the isomerization of each complex over a range of temperatures using NMR spectroscopic analysis. Figure 2.11 shows the data for $\mathbf{1_{Ms}}$ as a representative example. The data were fit to the kinetic model shown in Figure 2.11,[28] by nonlinear least-squares (NLLS) regression.[29] The thermodynamic and activation parameters for these equilibrium processes were determined using the van't Hoff and Eyring equations, respectively. As summarized in Table 2.3, both the rate and equilibrium constant for isomerization varies as a function of sulfonamide. However, neither of these values correlates with the observed rate of C(sp^3)–N coupling.

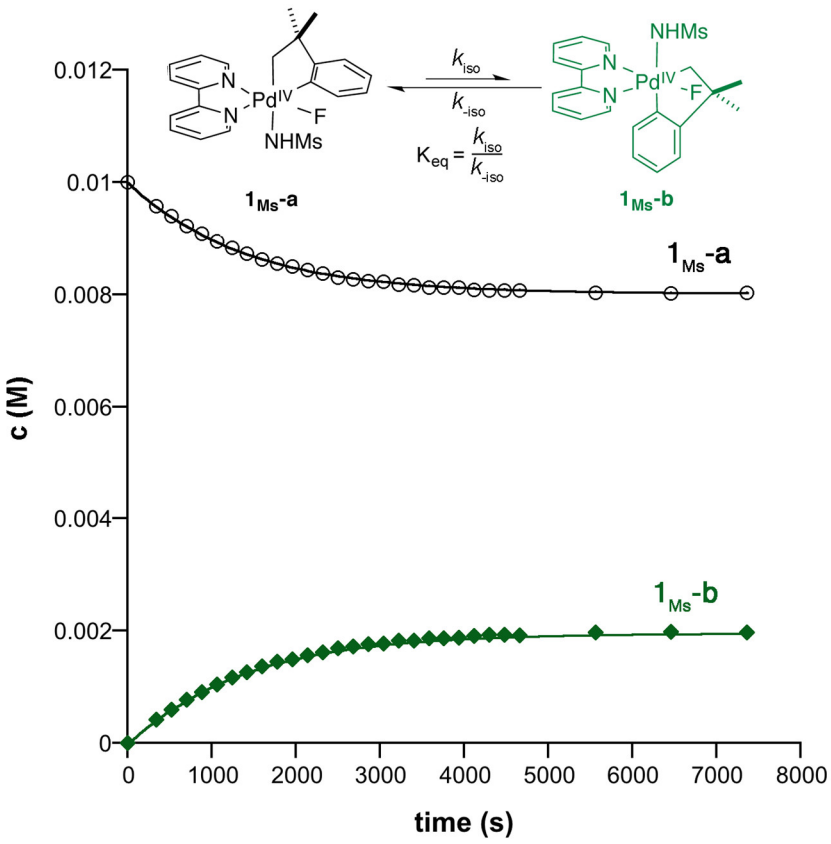

Figure 2.11 1_{Ms}-a/1_{Ms}-b isomerization process at 45 ºC. Solid lines are the best fit using GEPASI.

	TfNH$^-$	MsNH$^-$	TsMeN$^-$
ΔH^{0} [1]	1.08	0.21	0.06
ΔS^{0} [2]	–0.45	–2.16	–1.17
$\Delta G^{0}_{65°C}$ [1]	1.23	0.94	0.46
$K_{eq,65°C}$	0.16	0.24	0.51
$\Delta H^{‡}$ [1]	18.5	19.4	21.3
$\Delta S^{‡}$ [2]	–6.6	–14.8	–6.1
$\Delta G^{‡}_{65°C}$ [1]	20.7	24.4	23.4

[1] kcal·mol^{-1}; [2] cal/mol·K

Table 2.3. Thermodynamic and activation parameters for the isomerization process using different sulfonamide substrates.

2.4.5. Summary and Conclusions from Experimental Studies. Overall, the experimental mechanistic studies provide several mechanistic insights into this C(sp^3)–N reductive elimination process. First, sulfonamide structure has a significant influence on the rate of reductive elimination. Second, there is not a clear trend with respect to electronic effect (pK_a) of the

sulfonamide and the rate of C(sp^3)–N coupling (with sterically larger $TsNMe^-$ being the key outlier). Third, reductive elimination is 1st order in [Pd] and zero order in sulfonamide for all of the systems examined. Fourth, two Pd^{IV} isomers, connected by a facile isomerization step, are observed in the reaction mixture during the course of the reaction. Fifth, both isomerization and sulfonamide exchange are faster than reductive elimination.

Although the experimental studies do not provide a satisfying explanation for all these data, they allow us to rule out a direct S_N2 mechanism (pathway **I**). Furthermore, the observation of similar rates with bpy versus phen ligands suggests against the bipyridine de-chelation mechanism (pathway **II**). However, these studies do not provide data to distinguish between pathways **III** and **IV**. In addition, other undetectable isomers might also be accessible (for example, **1c**, **1d**, and **1e** in Figure 2.12) and could potentially be involved in C(sp^3)–N coupling via related mechanisms. In combination with the possibility of at least two pathways and five different Pd^{IV} isomers, there are a minimum of 14 kinetically indistiguishable mechanisms that could be operating in this system. In addition, many of these pathways could have similar barriers (and thus be operating simultaneously), further complicating experimental mechanistic analysis. As such, we turned to ZStruct to obtain a more detailed mechanistic understanding of this reductive elimination reaction.

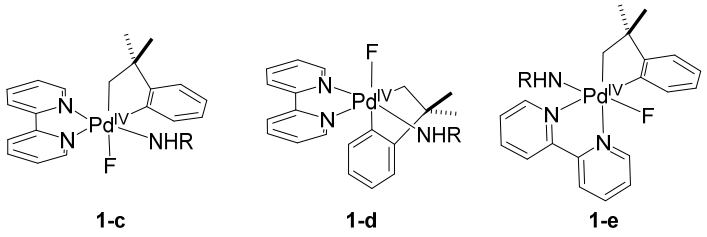

Figure 2.12 Possible unobserved Pd^{IV} isomers.

2.5 Identification of Isomerization Mechanism Using Computational Combinatorial Reaction Finding.

2.5.1 Reaction Path Identification. Based on the complexity of this system, we viewed it as an ideal test case for the computational mechanism discovery program, ZStruct.[6a,6b] ZStruct is a reaction exploration tool designed to interrogate complex chemical transformations using only minimal user input. The method is able to: (1) generate a large number of chemically reasonable reaction intermediates in a multistep mechanism through combinations of bond "break" and "form" operations; (2) evaluate relevant thermodynamic and kinetic parameters using DFT; and

(3) utilize state-of-the-art reaction path finding methods to efficiently locate minimum energy paths and transition states.[6c,6d] ZStruct differentiates axial and equatorial bonding positions of octahedral transition metal complexes and interrogates pseudorotation and axial/equatorial ligand isomerizations as well as bond-breaking events.

As such, it enables a full search of potentially reactive Pd^{IV} species. In comparison to a traditional DFT investigation, this method proposes and evaluates a combinatorial set of reactions *in silico* without substantial user intervention. This process does not require input of a predetermined set of hypothetical reaction steps, so the mechanistic pathways that are evaluated by ZStruct can be completely unexpected. ZStruct was initially developed and tested for reactions of main group compounds,[7,30] and the current work represents the first application to transition metal complexes. A summary of these steps is shown in Figure 2.13, and a full description of the method is given in the introduction chapter of this dissertation.

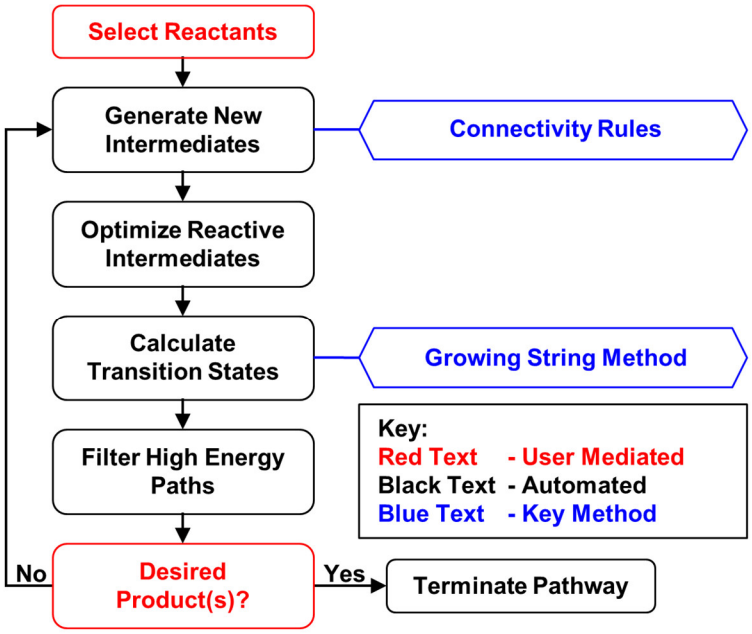

Figure 2.13. Overview of the ZStruct Combinatorial Reaction Finding Tool

2.5.2. Computational Details. **1_{Ms}-a/1_{Ms}-b** were selected as chemically relevant and computationally tractable starting complexes for the ZStruct analysis. Application of ZStruct to **1_{Ms}-a/b** generated 9,482 chemical structures and 794 individual elementary steps as well as all 794 associated transition states. During the initial assessment of reaction paths, we used the B3LYP density functional[31] in a spin restricted formalism with the LANL2DZ[32] basis set.[33] The cost of the search was approximately 80,000 computing hours, which corresponds to less than 1

week of computational time on 1,000 CPUs. To narrow these pathways down to the most plausible reaction mechanisms, screening and higher-level evaluations were performed, as shown in Figure 2.14.

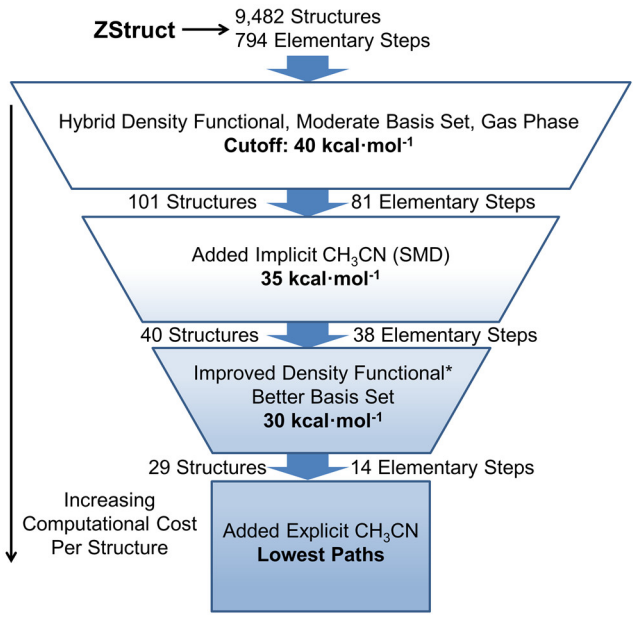

Figure 2.14. Screening and activation energy cutoffs ($\Delta G^{\ddagger}$) used for finding the lowest energy pathways from $\mathbf{1}_{Ms}$. *Improved density functional incorporating long-range and dispersion corrections.

The energy cutoffs were selected based on the experimentally measured barriers for isomerization and reductive elimination from $\mathbf{1}_{Ms}$**-a**. The experimental barriers, which are all less than 28 kcal·mol^{-1}, suggested that barriers more than a few kcal·mol^{-1} higher would be uncompetitive. Taking into account corrections from solvent,[34] we set the first screening cutoff at 40 kcal·mol^{-1}. After removing pathways with activation energies of ≥40 kcal·mol^{-1}, 81 elementary steps (~10% of the total generated) remained for further analysis (first filter, Figure 2.13). For these elementary steps, the energies were evaluated at an implicit solvent corrected level of theory [SMD][35,36] and were subjected to a stricter energy filter of 35 kcal·mol^{-1}. This second filter reduced the key reactions to include 38 elementary steps.

The lowest energy pathways for isomerization and C(sp^3)–N reductive elimination were then analyzed using the dispersion and long-range corrected ωB97X-D density functional[37] with 6-311++G** basis set for hydrogen through sulfur and LANL2TZ(f) for Pd to provide accurate

energetics.[38] For the 14 lowest barrier elementary steps (third filter), the geometries were re-optimized after adding a single explicit acetonitrile as a reagent to account for solvent binding to the palladium center (fourth filter).[39] For a more detailed description of the ZStruct method, selection of level of theory, as well as the development and application of energy cutoffs, see appendicies for this chapter.

2.5.3 Overview of ZStruct Results. As summarized in Figure 2.15, the ZStruct studies predicted two different, energetically viable pathways for isomerization between **1_{Ms}-a** and **1_{Ms}-b** as well as for C(sp^3)–N bond-forming reductive elimination. A first low energy mechanism involves the proposed sulfonamide dissociation/S_N2 pathway involving intermediate **4_{Ms}** (pathway **IV** in Figure 2.15). However, ZStruct also identified previously unanticipated pathways for both isomerization and C(sp^3)–N coupling, which proceed via an oxygen-bound sulfonamide intermediate (**5_{Ms}**). As described in detail below, this unanticipated pathway is critical to explain the observed trends in rate as a function of sulfonamide substitution. A complete discussion of the computational results is provided below.

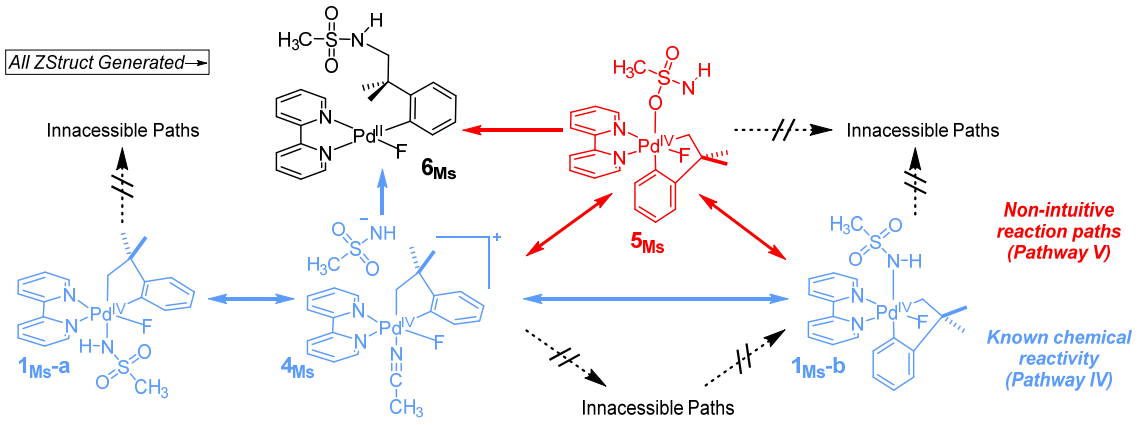

Figure 2.15. Overview of ZStruct search of the reactivity of **1_{Ms}-a** involving multiple unproductive search paths as well as known and unknown chemical reactivity. Shown in blue are expected chemical reactivity while red highlights the non-intuitive reaction paths.

2.5.4 ZStruct Pathways for Isomerization. ZStruct generated two low barrier mechanisms for the isomerization of **1_{Ms}-a** to **1_{Ms}-b** (Figure 2.16). In the first elementary step, **$TS7_{Ms}$**, the Pd–$NHSO_2CH_3$ bond of **1_{Ms}-a** is exchanged for a Pd–$NCCH_3$ bond to generate intermediate **4_{Ms}**.[40] Complex **4_{Ms}** then undergoes sulfonamide binding and concomitant reorganization of the aryl

backbone to afford isomer **1$_{Ms}$-b** through **TS8$_{MS}$**. The computed ΔG^0 was 1.0 kcal·mol^{-1}, which agrees with the experimentally measured 0.94 ± 0.05 kcal·mol^{-1} at 65 °C.

The second isomerization pathway proceeds via displacement of MsNH$^-$ by CH_3CN to form **4$_{Ms}$,** but then follows a unique path compared to the first isomerization mechanism. From **4$_{Ms}$**, coordination of the sulfonamide through one of its oxygen atoms leads to **5$_{Ms}$** via **TS9$_{Ms}$**. This O-bound sulfonamide intermediate then undergoes a concerted exchange of the sulfonamide oxygen with nitrogen at the palladium center via **TS10$_{Ms}$** to form the product **1$_{Ms}$-b**. Notably, the κ^2-coordination seen in **TS10$_{Ms}$** resembles that of bidentate sulfonamide-ligated Pd^{IV} intermediates proposed by Ritter and coworkers.[14] The similarity in the activation barriers for the two mechanisms in Figure 2.16 ($\Delta\Delta G^{‡}$ = 0.2 kcal·mol^{-1}) suggests that they likely occur competitively.

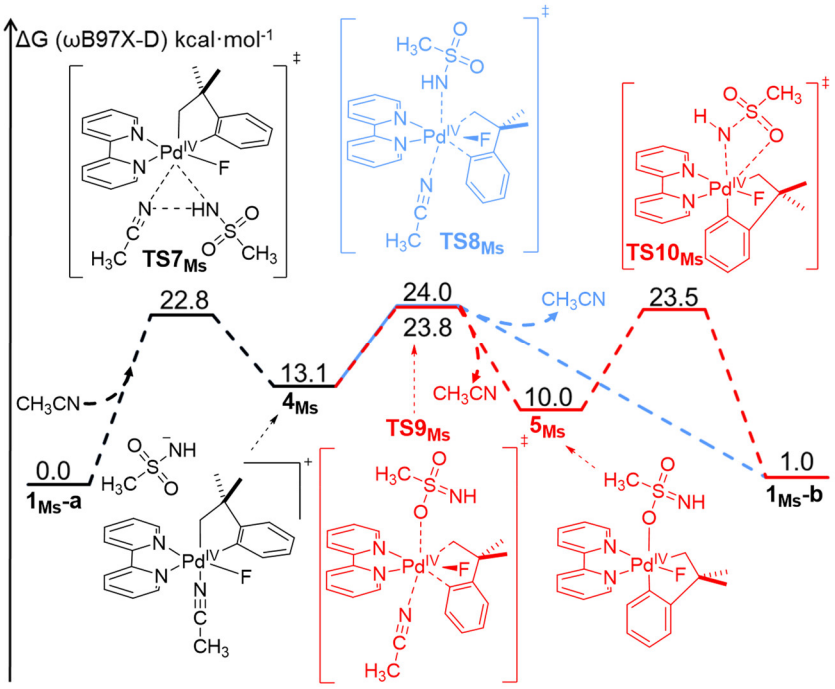

Figure 2.16. Two pathways for isomerization of **1$_{Ms}$-a** to **1$_{Ms}$-b**.

The experimental value of $\Delta G^{‡}$ for isomerization (24.4 kcal·mol^{-1} at 65 ºC) is in close agreement with the computed barriers of 24.0 and 23.8 kcal·mol^{-1} for the mechanisms in Figure 2.16. The computation is also consistent with the experimental observation that the isomerization process is zero order in sulfonamide. Furthermore, the ordered conformation of the sulfonamide

approach as well as the presence of a stabilizing CH_3CN ligand in **TS8$_{Ms}$** and **TS9$_{Ms}$** are both consistent with the experimentally measured $\Delta S^{\ddagger}$ value of -14.8 ± 3.4 cal·K^{-1}·mol^{-1}.

While searching for reaction pathways connecting the observable isomers (**1$_{Ms}$-a** to **1$_{Ms}$-b)**, three additional pathways were found leading to experimentally unobserved isomers (Figure 2.17). All three of these isomers (**1$_{Ms}$-c, 1$_{Ms}$-d** and **1$_{Ms}$-e**) were calculated to be more thermodynamically stable than **1$_{Ms}$-a** and **1$_{Ms}$-b**. However, the only kinetically viable pathway for isomerization connects **1$_{Ms}$-a** and **1$_{Ms}$-b**.[41] Overall, these results are consistent with the experimental observation that **1$_{Ms}$-a** and **1$_{Ms}$-b** are the only isomers detected experimentally (Figure 2.1 and Figure 2.12), and indicate that the other isomers are not kinetically relevant intermediates.

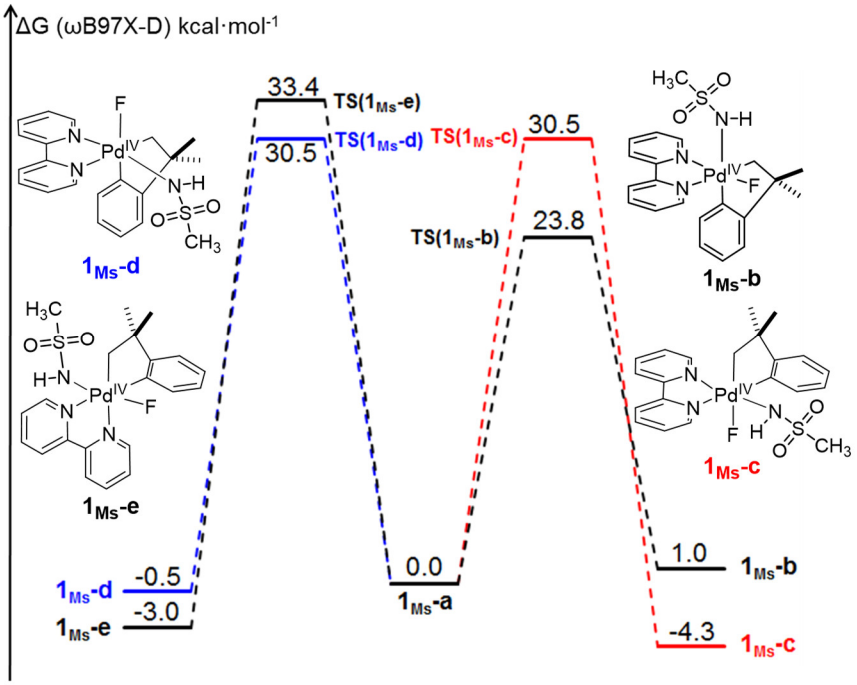

Figure 2.17. Energy barriers for pathways leading to the formation of **1$_{Ms}$** isomers (see Appendices for full reaction pathways).

2.6 ZStruct Evaluation of C(sp^3)–N Bond-Forming Reductive Elimination.

After ruling out the participation of other Pd^{IV} isomers, we analyzed possible pathways leading from **1$_{Ms}$-a** and **1$_{Ms}$-b** to C(sp^3)–N bond-forming reductive elimination.[42,43] ZStruct identified the proposed pathways **II-IV** as well as an unanticipated pathway, **V**. ZStruct predicts that pathway **II** is energetically inaccessible ($\Delta G^{\ddagger} > 32.0$ kcal/mol; see Appendices for complete

details). This is consistent with the experimental results, which provided evidence against this mechanism. In addition, the direct reductive elimination pathway (**III**) did not pass the screening criteria of Figure 2.13., as it has a calculated $\Delta G^{\ddagger}$ of 51.7 kcal·mol^{-1} (see Appendices for details). As such, the discussion below focuses on pathway **IV** as well as the new mechanism identified by ZStruct (pathway **V**).

2.6.1 <u>Pathway IV</u>. ZStruct found that the lowest energy route for C(sp^3)–N coupling starting from **1$_{Ms}$-a** is a two-step sequence (pathway **IV** in Figure 2.7). The first step involves the pre-equilibrium exchange of MsNH$^-$ for CH$_3$CN (**TS7$_{Ms}$**) to generate an octahedral Pd^{IV} acetonitrile complex, **4$_{Ms}$** (Figure 2.18). Rate- limiting C(sp^3)–N bond-formation then proceeds via outer sphere S$_N$2-type attack of MsNH$^-$ on the axial sp^3-carbon ligand (**TS11$_{Ms}$**, Figure 2.19).

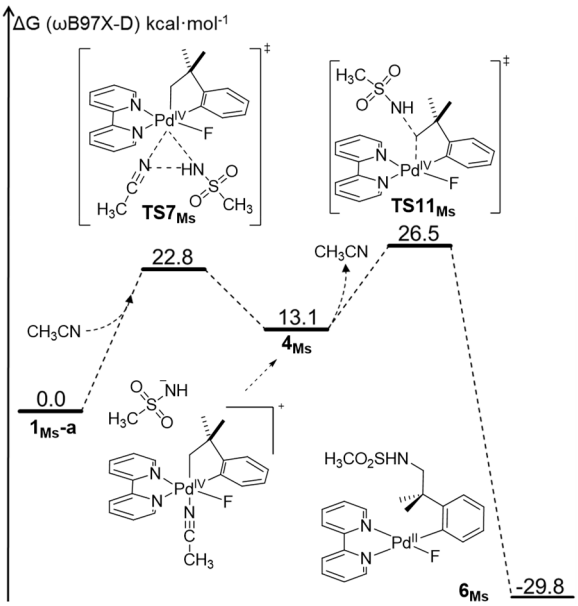

Figure 2.18. Pathway **IV**. C(sp^3)–N reductive elimination pathway from **1$_{Ms}$-a**.

The nucleophile has an approach angle of 143.3° (compared to the ideal 180º in a traditional S$_N$2 reaction), highlighting the steric constraints of this transition state. The calculated value of $\Delta G^{\ddagger}$ (26.5 kcal·mol^{-1} at 65 ºC) matches well with that observed experimentally (25.7 kcal·mol^{-1}). Importantly, related S$_N$2-like mechanisms for C(sp^3)–heteroatom reductive elimination have been proposed at platinum,[3] palladium,[44] and rhodium.[45] However, the S$_N$2-nature of **TS11$_{Ms}$** is particularly noteworthy considering that the participating carbon is a highly hindered neopentyl-type center.[12]

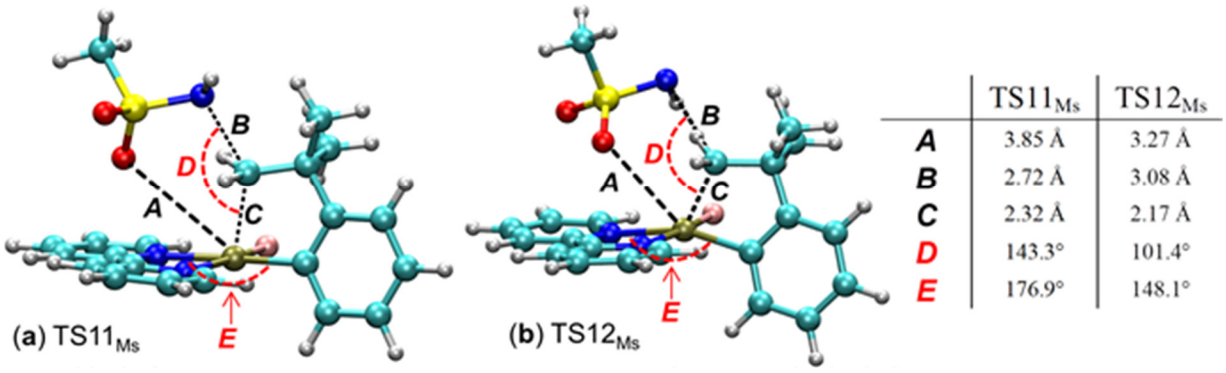

	$TS11_{Ms}$	$TS12_{Ms}$
A	3.85 Å	3.27 Å
B	2.72 Å	3.08 Å
C	2.32 Å	2.17 Å
D	143.3°	101.4°
E	176.9°	148.1°

Figure 2.19. (a) C(sp^3)–N reductive elimination transition state **$TS11_{Ms}$** from **1_{Ms}-a** (in Pathway IV). (b) C(sp^3)–N reductive elimination transition state **$TS12_{Ms}$** from **1_{Ms}-b** (in Pathway V).

2.6.2 <u>Pathway V.</u> A second low energy pathway for C–N bond formation was identified by ZStruct and originates from **1_{Ms}-b**. Interestingly, this mechanism (pathway **V**) is not among those initially hypothesized above, and has much less precedent in the literature.[13] As shown in Figure 2.20, pathway **V** involves a two-step sequence, in which an initial nitrogen-oxygen exchange of the sulfonamide at the Pd center is followed by reductive elimination via an inner sphere concerted 5-membered transition state. Since the second step is calculated to be rate determining, the rate expression for this pathway is fully consistent with the experimental kinetic orders. The complete reaction profile for C(sp^3)–N bond formation from **1_{Ms}-b** is shown in Figure 2.21. The calculated value of $\Delta G^{\ddagger}$ for the highest energy transition state of pathway **IV** (26.7 kcal·mol^{-1} at 65 ºC) is very similar to that for pathway **V** (26.5 kcal·mol^{-1} at 65 ºC). This suggests that the two pathways occur at comparable rates in this system.

As shown in Figure 2.21, the inner sphere C(sp^3)–N coupling in pathway **V** proceeds via backside attack, analogous to the outer-sphere S_N2-type mechanism of pathway **IV**. As such, stereochemical labeling studies would not be effective for experimentally distinguishing between pathways **IV** and **V**. However, the bond angle for approach of the sulfonamide in **$TS12_{Ms}$** is much shallower than that in pathway **V** (101.4° in comparison to 143.3°). This is due to a sustained stabilizing Pd–O interaction in the transition state, where the Pd–O distance is 3.27 Å for **$TS12_{Ms}$**, compared to 3.85 Å in **$TS11_{Ms}$** (Figure 2.19). Other key bond lengths and angle comparisons are given in Figure 2.19, and these values are summarized for all of sulfonamides in the Appendices.

Because they are both S_N2 reactions with similar rate expressions, **$TS11_{Ms}$** and **$TS12_{Ms}$** might be initially considered chemically indistinguishable. However, in practice, there are a

number of key differences including transition state structure (quantitatively different angles and bond lengths, Figure 2.19), inner vs. outer sphere mechanism, and activation barriers.

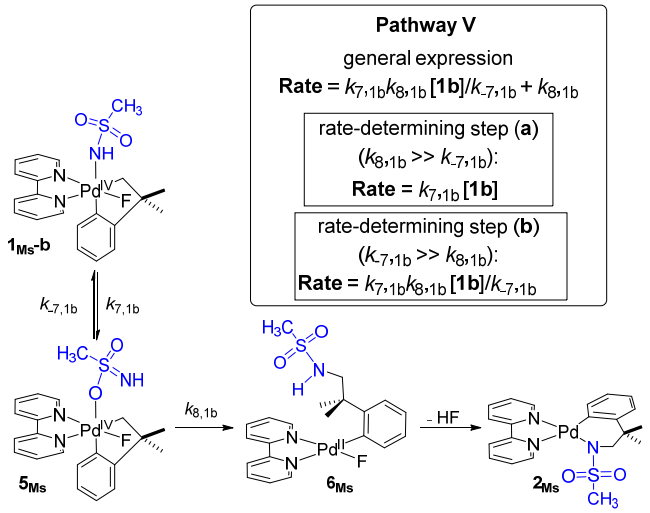

Figure 2.20. Pathway V from 1_{Ms}-b

As will be shown below, the differences in reaction mechanism lead to changes in mechanism (pathway **IV** vs **V**) as a function of sulfonamide structure.

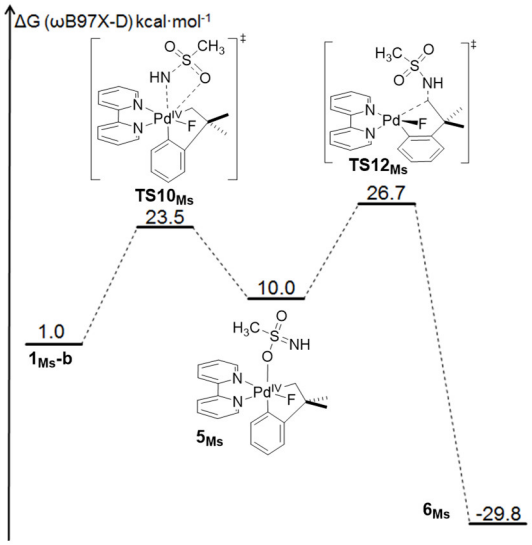

Figure 2.21. Pathway **V**. C(sp^3)–N reductive elimination from $\mathbf{1_{Ms}}$**-b**. All energies are referenced to $\mathbf{1_{Ms}}$**-a**.

2.7 Computational Sulfonamide Screen and Experimental Verification.

To further assess the feasibility of the proposed pathways, we computationally analyzed reductive elimination through pathways **IV** and **V** for the sulfonamides $TfNH^-$, $CF_2HSO_2NH^-$, $TsNH^-$ and $TsMeN^-$. As summarized in Table 2.4 and Figure 2.22, the lowest calculated barriers and experimental $\Delta G^‡$ values for the five sulfonamides are in excellent agreement ($R^2 = 0.90$).

The predicted lowest energy pathway (i.e., **IV** versus **V**) was found to vary as a function of sulfonamide structure. For the sulfonamides $CF_2HSO_2NH^-$ and $CH_3SO_2NH^-$, pathways **IV** and **V** have similar values of $\Delta G^‡$, while $TsNH^-$ favors pathway **IV**. In contrast, $TsMeN^-$ and $TfNH^-$ favor pathway **V**. For all five sulfonamides, the calculated $\Delta G^‡$ for pathway **IV** generally correlates with pK_a, with higher pK_a's affording higher barriers. (A linear regression of $\Delta G^‡$ for pathway **IV** versus pK_a has an $R^2 = 0.77$).

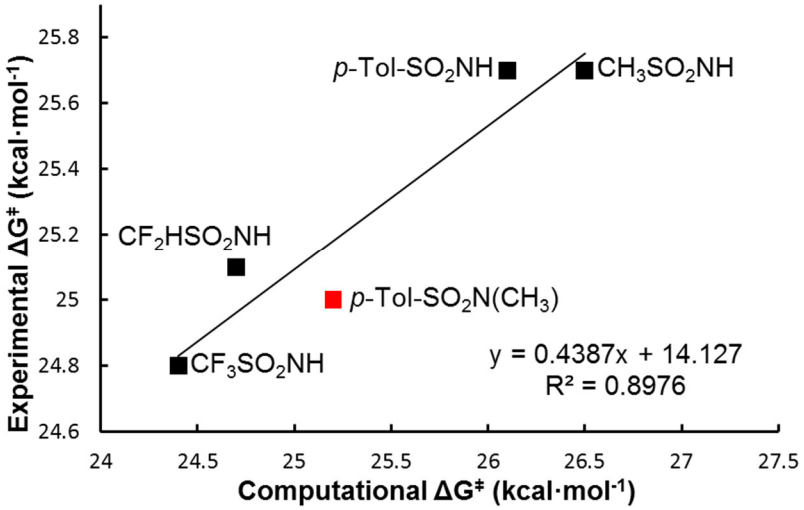

Figure 2.22. Comparison between computational and experimental $\Delta G^‡$ for C(sp^3)–N reductive elimination. The point computation predicted prior to experiment is highlighted in red.

This trend is consistent with results from Goldberg's group studying C(sp^3)–O coupling at Pt^{IV}. Specifically, they showed a linear Hammett plot ($\rho = +1.44$) upon varying the substituents on the benzoate nucleophile.[19e] A key consequence of this pK_a trend is that the most basic sulfonamide ($TsMeN^-$) has a prohibitively high barrier for reductive elimination via pathway **IV**. As such, the rela- tively fast rate of reductive elimination with this nucleophile is due to the accessibility of pathway **V**, which does not trend with pK_a (a linear regression for the five sulfonamides has $R^2 = 0.28$).

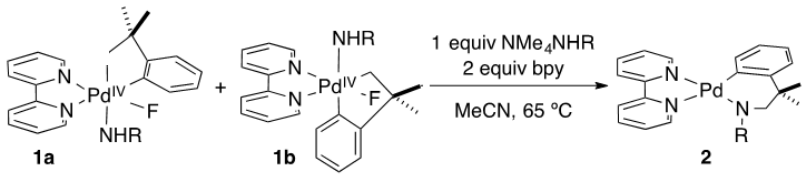

R	pK$_a$*	Path. IV[a] ΔG‡$_{DFT}$	Path. V[b] ΔG‡$_{DFT}$	ΔG‡$_{Exp}$
CF_3SO_2 (Tf)	6.37	25.3	24.4	24.8
CF_2HSO_2	7.46	24.7	25.1	25.1
p-Tol-SO_2NH (Ts)	10.26	26.1	28.5	25.7
CH_3SO_2 (Ms)	10.87	26.5	26.7	25.7
p-Tol-SO_2NCH_3 (Ts)	11.67	27.8	25.2	25.0

*pKa values from the literature database of ACD/Laboratories Software version 11.02. [a]From $\mathbf{1_{Ms}}$-**a**; [b]from $\mathbf{1_{Ms}}$-**b**.

Table 2.4 Comparison of lowest barrier calculated C(sp^3)–N reductive elimination and experimentally measured ΔG‡ values for various sulfonamides

The factors controlling the relative barriers for pathway **V** as a function of sulfonamide appear to be complex, and we have not been able to identify clear trends in $\Delta G^{\ddagger}$ as a function of pK_a or bond lengths/bond angles that fit for all of the sulfonamides. Nonetheless, one instructive comparison for pathway **V** is between $TsHN^-$ and $TsMeN^-$, which differ only by substitution of a hydrogen for a methyl group on the sulfonamide. As shown in Table 2.4, this change results in a 3.3 kcal·mol^{-1} decrease in $\Delta G^{\ddagger}$ for pathway **V**, thereby enabling fast reductive elimination from the $TsMeN^-$ complex via this pathway. A carefully comparison of these systems shows that, with $TsNH^-$, the transition state for C–N bond formation via pathway **V** requires breaking a TsN–H---F–Pd hydrogen bond. This hydrogen-bond breaking is clearly reflected in the increasing H---F distance moving from $\mathbf{5_{Ts}}$ (2.01 Å) to transition state $\mathbf{TS12_{Ts}}$ (3.05 Å) to the product $\mathbf{6}_{Ts}$ (4.80 Å). Importantly, a similar hydrogen bond is not possible in the analogous intermediate $\mathbf{5_{TsNMe}}$, since the hydrogen bond donor has been replaced with a methyl group. The magnitude of $\Delta\Delta G^{\ddagger}$ between the two sulfonamides for pathway **V** (3.3 kcal/mol) is fully consistent with the penalty associated with breaking a hydrogen bond. As such, we propose that the lack of a H-bond donor in $TsMeN^-$

is likely responsible for the preferred mechanism for C(sp^3)–N reductive elimination, and enables fast C–N bond-formation despite the high pK_a of this sulfonamide.

Overall, the computational activation barriers for the five sulfonamides agree well with experiment (Figure 2.22), but only when taking into account two distinct mechanistic routes, pathways **IV** and **V**. Furthermore, while pathway **IV** is computed to be the lowest (or approximately equal) barrier mechanism for 3 of the 5 sulfonamides, $\mathbf{1_{TsNMe}}$ has a much lower barrier for pathway **V**. Pathway **V** is also favored for $\mathbf{1_{Tf}}$, but in this case the energy difference between pathways **IV** and **V** is less significant ($\Delta\Delta G^{\ddagger} < 1$ kcal·mol^{-1}). These observations are consistent with the experimental activation entropies. The $\Delta S^{\ddagger}$ values for C(sp^3)-N coupling from $\mathbf{1_{Tf}}$ and $\mathbf{1_{TsNMe}}$ are similar (–4.9 and –3.4 cal·K^{-1}·mol^{-1}) and clearly distinct from $\Delta S^{\ddagger}$ for $\mathbf{1_{Ms}}$ (–23.5 cal·K^{-1}·mol^{-1}). The higher $\Delta S^{\ddagger}$ likely reflects the increased order associated with solvation of the charged intermediates/transition state in pathway **IV** versus the neutral compounds in pathway **V**. This demonstrates that both predicted mechanisms are critical for understanding the observed rates.

2.8 Additional predictions based on thermodynamic considerations.

We next sought to computationally examine the impact of moving to the sulfonamide Tf_2N^-, which has an even lower pK_a than that of $TfNH^-$. The studies described above suggest that the Pd^{IV} complex of this sulfonamide ($\mathbf{1_{BisTf}}$) should react at a fast rate via pathway **IV**. Consistent with this hypothesis, the $\Delta G^{\ddagger}$ for C(sp^3)–N coupling from $\mathbf{1_{BisTf}}$ via pathway **IV** is calculated to be 23.7 kcal·mol^{-1}. A significantly higher value (26.9 kcal·mol^{-1}) is calculated for pathway **V**. However, the simulations also predict that the C(sp^3)–N coupling product $\mathbf{6_{BisTf}}$ is 5.5 kcal·mol^{-1} *uphill* from the starting material, $\mathbf{1_{BisTf}}$. Therefore, C(sp^3)–N coupling from $\mathbf{1_{BisTf}}$ is predicted to be kinetically fast, but thermodynamically unfavorable (Figure 2.23).

The ZStruct assessment of $\mathbf{1_{BisTf}}$ suggested that alternative, more thermodynamically favorable reductive elimination pathways are likely to occur with this complex. As such, we also computationally evaluated the pathway for C(sp^3)–C(sp^2) bond-forming reductive elimination from $\mathbf{1_{BisTf}}$.

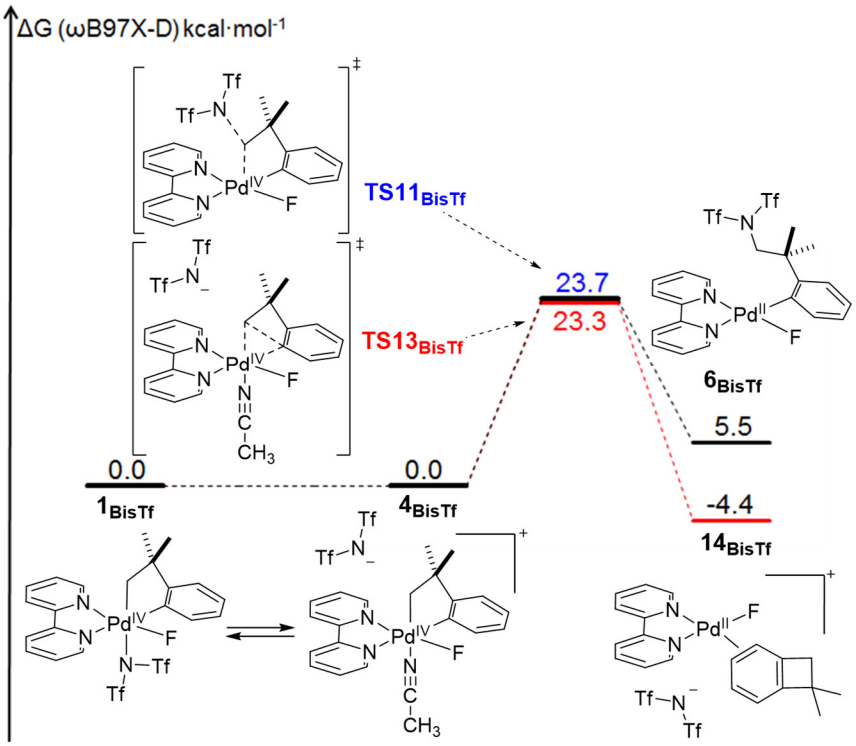

Figure 2.23. C(sp^3)–N versus C(sp^3)-C(sp^2) reductive elimination from common pentacoordinate intermediate $\mathbf{4}_{\mathbf{BisTf}}$. All energies referenced to $\mathbf{1}_{\mathbf{BisTf}}$-**a**.

This process is predicted to be thermodynamically downhill (–4.4 kcal·mol^{-1} to generate the initial intermediate $\mathbf{14}_{\mathbf{BisTf}}$), with a computed activation barrier of 23.3 kcal·mol^{-1} (Figure 2.23). To test these computational predictions, we conducted the thermolysis of a mixture of **3** with 2 equiv of NMe_4NTf_2 in CD_3CN at 65 ºC. As anticipated, none of the thermodynamically disfavored product of C(sp^3)–N bond-forming reductive elimination ($\mathbf{6}_{\mathbf{BisTf}}$) was detected. Instead, the C(sp^2)–C(sp^3) bond-forming reductive elimination product, cyclobutane **15**, was obtained in quantitative yield (Figure 2.24). The activation barrier for the formation of **15** was measured experimentally as 23.8 kcal·mol^{-1}. This is in excellent agreement with the computational prediction of 23.3 kcal·mol^{-1}.

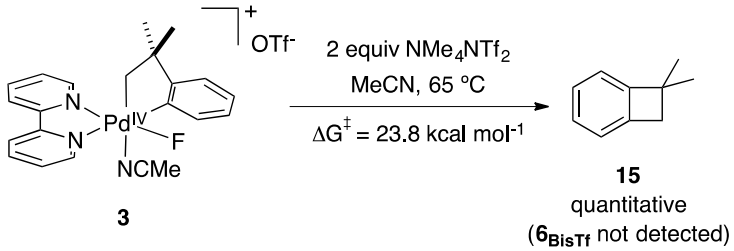

Figure 2.24. Thermolysis of 3 in the presence of NMe_4NTf_2

2.9 Conclusions

Detailed mechanistic investigations of reductive elimination from octahedral Pd^{IV} complexes are challenging due to the presence of multiple isomers and the feasibility of multiple kinetically indistinguishable pathways. In this report, we disclose a combined experimental and simulation investigation of competing isomerization and C(sp^3)–N bond-forming reductive elimination from a series of Pd^{IV} complexes. Several possible pathways could be ruled out through experimental investigations, but numerous plausible mechanisms proved to be experimentally indistinguishable.

These challenges were addressed by using ZStruct, a computational reaction discovery method, to explore this complicated chemical landscape. ZStruct enabled us to rapidly rule out pathways involving unobservable isomers and to establish an isomerization mechanism within 1 kcal·mol^{-1} of the experimentally determined $\Delta G^{\ddagger}$.

In addition, two low energy mechanisms for C(sp^3)–N bond-formation were identified: an S_N2-type outer sphere C–N coupling (pathway **IV**) and a concerted inner sphere C–N bond formation that proceeds via a 5-membered transition state from an O-bound sulfonamide intermediate (pathway **V**). Pathway **V** appears to be the major pathway for reductive elimination for some sulfonamides. This hitherto unreported pathway therefore merits consideration in any future studies of C(sp^3)–N reductive elimination reactions of sulfonamide derivatives.

Taking into account competition between these two mechanisms, ZStruct results showed good agreement with the experimentally measured values of $\Delta G^{\ddagger}$ for C(sp^3)–N bond-forming reductive elimination with stereoelectronically varied sulfonamides. Across a variety of substrates, competition between pathways **IV** and **V** needs to be accounted for to accurately predict and explain experimental outcomes. In one case, computation also predicted that C(sp^2)–

$C(sp^3)$ reductive elimination would occur instead of the kinetically facile, yet thermodynamically disfavored $C(sp^3)$–N coupling from $\mathbf{1}_{\mathbf{BisTf}}$.

This study contributes to a growing body of work demonstrating the advantages of a combined simulation and experimental approach to mechanistic investigations, especially those pertaining to organometallic complexes.[46] Moving forward, we plan to use this approach to evaluate the full suite of possible reductive elimination reactions from $\mathbf{1}_{\mathbf{Ms}}$ and its analogues (i.e., competing $C(sp^3)$–N, $C(sp^2)$–N, $C(sp^3)$–F, $C(sp^2)$–F, and $C(sp^3)$–$C(sp^2)$ reductive elimination).

While this chapter demonstrates that the combination of experimental mechanistic studies with ZStruct holds great promise for the detailed evaluation of complex reaction mechanisms, identification of structural features of the molecule, specifically intramolecular interactions such as the H-F interaction remain difficult to justify computationally. Using only manual analysis of intramolecular hydrogen bond interactions provided an explanation with a narrow scope limited predictive potential. Chapter 3 endeavors to develop a reliable approach for computationally investigating important molecular features through design and subsequent study of a thermodynamic landscape of complexes using statistical analysis.

2.10 References

(1) For some examples of Pd^{II}-catalyzed $C(sp^3)$–H amination see: (a) McNally, A.; Haffemayer, B.; Collins, B. S. L.; Gaunt, M. J. *Nature* **2014**, *510*, 129. (b) Sun, W.-W.; Cao, P.; Mei, R.-Q.; Li, Y.; Ma, Y.-L.; Wu, B. *Org. Lett.* **2014**, *16*, 480. (c) Ye, X.; He, Z.; Ahmed, T.; Weise, K.; Akhmedov, N. G.; Petersen, J. L.; Shi, X. *Chem. Sci.* **2013**, *4*, 3712. (d) Zhang, Q.; Chen, K.; Rao, W.-H.; Zhang, Y.; Chen, F.-J.; Shi, B.-F. *Angew. Chem. Int. Ed.* **2013**, *52*, 13588. (e) Iglesias, Á.; Álvarez, R.; de Lera, Á. R.; Muñiz, K. *Angew. Chem. Int. Ed.* **2012**, *51*, 2225. (f) Nadres, E. T.; Daugulis, O. *J. Am. Chem. Soc.* **2012**, *134*, 7. (g) He, G.; Zhao, Y.; Zhang, S.; Lu, C.; Chen, G. *J. Am. Chem. Soc.* **2012**, *134*, 3.

(2) Amination of alkenes see: (a) Martínez, C.; Wu, Y.; Weinstein, A. B.; Stahl, S.; Liu, G.; Muñiz, K. *J. Org. Chem.* **2013**, *78*, 6309. (b) Muñiz, K.; Martínez, C. *J. Org. Chem.* **2013**, *78*, 2168. (c) Xiong, T.; Li, Y.; Mao, L.; Zhang, Q.; Zhang, Q. *Chem. Commun.* **2012**, *48*, 2246. (d) Xu, T.; Qiu, S.; Liu, G. *J. Organomet. Chem.* **2011**, *696*, 46. (e) Liskin, D. V.; Sibbald, P. A.; Rosewall, C. F.; Michael, F. E. *J. Org. Chem.* **2010**, *75*, 6294. (f) Iglesias, Á.; Pérez, E. G.; Muñiz, K. *Angew. Chem. Int. Ed.* **2010**, *49*, 8109. (g) Sibbald, P. A.; Michael, F. E. *Org. Lett.* **2009**, *11*, 1147. (h) Rosewall, C. F.; Sibbald, P. A.; Liskin, D. V.; Michael, F. E. *J. Am. Chem. Soc.* **2009**, *131*, 9488. (i) Sibbald, P. A.; Rosewall, C. F.; Swartz, R. D.; Michael, F. E. *J. Am. Chem. Soc.* **2009**, *131*, 15945. (j) Muñiz, K.; Hövelmann, C. H.; Streuff, J. *J. Am. Chem. Soc.* **2008**, *130*, 763. (k) Muñiz, K. *J. Am. Chem. Soc.* **2007**, *129*, 14542. (l) Minatti, A.; Muñiz, K. *Chem. Soc. Rev.* **2007**, *36*, 1142. (m) Streuff, J.; Hövelmann, C. H.; Nieger, M.; Muñiz, K. *J. Am. Chem. Soc.* **2005**, *127*, 14586.

(3) For mechanistic study on C(sp^3)–N bond-forming reductive elimination from Pt^{IV}, see: Pawlikowski, A. V.; Getty, A. D.; Goldberg, K. I. *J. Am. Chem. Soc.* **2007**, *129*, 10382.

(4) Iglesias, Á.; Muñiz, K. *Helv. Chim. Acta* **2012**, *95*, 2007.

(5) Pérez-Temprano, M. H.; Racowski, J. M.; Kampf, J. W.; Sanford, M. S. *J. Am. Chem. Soc.* **2014**, *136*, 4097.

(6) The 2 equiv of bpy is added to limit 2º side reactions of the reductive elimination product (i.e., substitution of the bpy ligand of $\mathbf{2_{Ts}}$ with $TsNH^-$). It is not believed to impact the mechanism of the C(sp^3)–N coupling reaction. See reference 5 for additional information.

(7) (a) Zimmerman, P. M. *J. Comput. Chem.* **2015**, *36*, 601. (b) Zimmerman, P. M. *Mol. Simul.* **2015**, *41*, 43. (c) Zimmerman, P. M. *J. Comput. Chem.* **2013**, *34*, 1385. (d) Zimmerman, P. *J. Chem. Theory Comput.* **2013**, *9*, 3043. (e) Zimmerman, P. M. *J. Chem. Phys.* **2013**, *138*, 184102.

(8) The cost of the search was approximately 80,000 computing hours, which corresponds to less than 1 week of computational time on 1,000 CPUs.

(9) For other recent publications demonstrating chemical exploration software see: (a) Wang, L.-P.; Titov, A.; McGibbon, R.; Liu, F.; Pande, V. S.; Martínez, T. J. *Nat. Chem.* **2014**, *6*, 1044–1048. (b) Rappoport, D.; Galvin, C. J.; Zubarev, D. Y.; Aspuru-Guzik, A. *J. Chem. Theory Comput.* **2014**, *10*, 897–907. (c) Maeda, S.; Morokuma, K. *J. Chem. Theory Comput.* **2011**, *7*, 2335–2345. (d) Maeda, S.; Taketsugu, T.; Morokuma, K. *J. Comput. Chem.* **2014**, *35*, 166–173. (e) Ohno, K.; Maeda, S. *Chem. Phys. Lett.* **2004**, *384*, 277–282. (f) Maeda, S.; Ohno, K.; Morokuma, K. *Phys. Chem. Chem. Phys.* **2013**, *15*, 3683–3701. (g) Bergeler, M.; Simm, G. N.; Proppe, J.; Reiher, M. *J. Chem. Theory Comput.* **2015**, *11*, 5712-5722.

(10) Byers, P. K.; Canty, A. J.; Crespo, M.; Puddephatt, R. J.; Scott, J. D. *Organometallics* **1988**, *7*, 1363–1367.

(11) Dick, A. R.; Kampf, J. W.; Sanford, M. S. *J. Am. Chem. Soc.* **2005**, *127*, 12790–12791.

(12) Camasso, N. M.; Pérez-Temprano, M. H.; Sanford, M. S. *J. Am. Chem. Soc.* **2014**, *136*, 12771.

(13) For a proposal of related pathways for C–O bond-forming reductive elimination with carboxylate nucleophiles, see: Gary, J. B.; Sanford, M. S. *Organometallics* **2011**, *30*, 6143.

(14) Furuya, T.; Benitez, D.; Tkatchouk, E.; Strom, A. E.; Tang, P.; Goddard, W. A.; Ritter, T. *J. Am. Chem. Soc.* **2010**, *132*, 3793–3807.

(15) Pawlikowski, A. V; Getty, A. D.; Goldberg, K. I. *J. Am. Chem. Soc.* **2007**, *129*, 10382–10393.

(16) For recent reviews on Pd^{IV} reductive elimination please see: (a) Muñiz, K. *Angew. Chemie - Int. Ed.* **2009**, *48*, 9412–9423. (b) Sehnal, P.; Taylor, R. J. K.; Fairlamb, I. J. S. *Chem. Rev.* **2010**, *110*, 824–889. (c) Xu, L.-M.; Li, B.-J.; Yang, Z.; Shi, Z.-J. *Chem. Soc. Rev.* **2010**, *39*, 712–733.

(17) For S_N2-mechanism of $C(sp^3)$-X (pathway I) from Pt^{IV} see: Shilov, A. E.; Shul'pin, G. B. *Chem. Rev.* **1997**, *97*, 2879.

(18) Literature precedents for pathway II see: (a) Arthur, K. L.; Wang, Q. L.; Bregel, D. M.; Smythe, N. A.; O'Neill, B. A.; Goldberg, K. I.; Moloy, K. G. *Organometallics* **2005,** *24,* 4624. (b) Crumpton-Bregel, D. M.; Goldberg, K. I. *J. Am. Chem. Soc.* **2003,** *125,* 9442. (c) Crumpton, D. M.; Goldberg, K. I. *J. Am. Chem. Soc.* **2000,** *122,* 962.

(19) Literature precedents for reductive elimination from cationic species (pathways III and V) see: (a) Smythe, N. A.; Grice, K. A.; Williams, B. S.; Goldberg, K. I. *Organometallics* **2009,** *28,* 277. (b) Khusnutdinova, J. R.; Newman, L. L.; Zavalij, P. Y.; Lam, Y.-F.; Vedernikov, A. N. *J. Am. Chem. Soc.* **2008,** *130,* 2174. (c) Khusnutdinova, J. R.; Zavalij, P. Y.; Vedernikov, A. N. *Organometallics* **2007,** *26,* 3466. (d) Vedernikov, A. N.; Binfield, S. A.; Zavalij, P. Y.; Khusnutdinova, J. R. *J. Am. Chem. Soc.* **2006,** *128,* 82. (e) Williams, B. S.; Goldberg, K. I. *J. Am. Chem. Soc.* **2001,** *123,* 2576. (f) Williams, B. S.; Holland, A. W.; Goldberg, K. I. *J. Am. Chem. Soc.* **1999,** *121,* 252.

(20) Literature precedents for pathway IV see: (a) Rivada-Wheelaghan, O.; Roselló-Merino, M.; Díez, J.; Maya, C.; López-Serrano, J.; Conejero, S. *Organometallics* **2014**, *33*, 5944. (b) Rivada-Wheelaghan, O.; Ortuño, M. A.; Díez, J.; García-Garrido, S. E.; Maya, C.; Lledós, A.; Conejero, S. *J. Am. Chem. Soc.* **2012**, *134*, 15261. (c) Crosby, S. H.; Thomas, H. R.; Clarkson, G. J.; Rourke, J. P. *Chem. Commun.* **2012**, *48*, 5775. (d) Zhao, S.-B.; Wang, R.-Y.; Nguyen, H.; Becker, J. J.; Gagné, M. R. *Chem. Commun*. **2012**, *48*, 443. (e) Khusnutdinova, J. R.; Newman, L. L.; Zavalij, P. Y.; Lam, Y.-F.; Vedernikov, A. N. *J. Am. Chem. Soc.* **2008**, *130*, 2174.

(21) The sulfonamide exchange cannot take place by an associative mechanism since $\mathbf{1_{Ts}}$ is coordinatively saturated.

(22) Rate studies were performed under our optimal conditions, using 1 equiv of bpy as an additive. As discussed in our previous communication (ref 5), the bpy is added to prevent decomposition of the reductive elimination product **2**, but does not impact the C–N coupling process (see ref. 6).

(23) The observed first order dependence of [Pd] rules out reductive elimination mechanisms involving two palladium centers.

(24) The observed zero order dependence on sulfonamide rules out mechanisms that involve displacement of the fluoride ligand with an equivalent of exogeneous sulfonamide prior to reductive elimination.

(25) Based on this data, we can also rule out the formation of a Pd^{IV} intermediate with two N-ligands and subsequent C-N reductive elimination. This pathway would also be expected to show a first order dependence on sulfonamide.

(26) For related experiments, see: (a) Racowski, J. M.; Dick, A. R.; Sanford, M. S. *J. Am. Chem. Soc.* **2009**, *131*, 10974. (b) Dick, A. R.; Kampf, J. W.; Sanford, M. S. *J. Am. Chem. Soc.* **2005**, *127*, 12790.

(27) The isomerization process was studied in the presence of excess of NMe_4NR to avoid reductive elimination processes during the measurement of the equilibrium. A zeroth-order dependence on [NMe_4NR] was observed for this step.

(28) Similar models were applied to TfNH and TsNMe.

(29) (a) Mendes, P. *Comput. Appl. Biosci.* **1993**, *9*, 563. (b) Mendes, P. *Trends Biochem. Sci.* **1997**, *22*, 361. (c) Mendes, P.; Kell, D. B. *Bioinformatics* **1998**, *14*, 869. (d) Martins, A. M.; Mendes, P.; Cordeiro, C.; Freire, A. P. *Eur. J. Biochem.* **2001**, *268*, 3930.

(30) (a) Sun, Z.; Winschel, G. A.; Zimmerman, P. M.; Nagorny, P. *Angew. Chem. Int. Ed.* **2014**, *53*, 11194–11198. (b) Ludwig, J. R.; Zimmerman, P. M.; Gianino, J. B.; Schindler, C. S. *Nature*, **2016**, in press: doi:10.1038/nature17432.

(31) (a) Becke, A. D. *Phys. Rev. A* **1988**, *38*, 3098–3100. (b) Becke, A. D. *J. Chem. Phys.* **1993**, *98*, 5648. (c) Lee, C.; Yang, W.; Parr, R. G. *Phys. Rev. B* **1988**, *37*, 785–789.

(32) (a) Hay, P. J.; Wadt, W. R. *J. Chem. Phys.* **1985**, *82*, 299. (b) Hay, P. J.; Wadt, W. R. *J. Chem. Phys.* **1985**, *82*, 270. (c) Hay, P. J.; Wadt, W. R. *J. Chem. Phys.* **1985**, *82*, 270. (d) Wadt, W. R.; Hay, P. J. *J. Chem. Phys.* **1985**, *82*, 284. (e) Dunning, T. H.; Hay, P. J. *Methods of Electronic Structure Theory, Volume 2*; Schaefer, H. F., Ed.; Plenum Publishing Company Limited: New York, 1977.

(33) The smaller basis set was chosen as a compromise between cost and accuracy in expectation of the large sample size of initial screening process.

(34) While the initial calculations were not performed using solvent, the maximum solvent stabilization observed from gas phase to fully solvated was 10 $kcal \cdot mol^{-1}$. Paths with $\Delta G^{\ddagger}$ above 40 $kcal \cdot mol^{-1}$ would still not compete with the rates observed for $C(sp^3)$-N R.E. or isomerization.

(35) For general paper on SMD: A.V.Marenich, C.J.Cramer, D.G.Truhlar. *J.Phys.Chem. B.* **2009**, *113*, 6378-6396.

(36) Tomasi, J.; Mennucci, B.; Cammi, R. *Chem. Rev*. **2005**, *105*, 2999. (b) Cammi, R.; Tomasi, J. *J. Comput. Chem*. **1995**, *16*, 1449.

(37) Chai, J. D.; Head-Gordon, M. *Phys. Chem. Chem. Phys.* **2008**, *10*, 6615.

(38) Minenkov, Y.; Singstad, Å.; Occhipinti, G.; Jensen, V. R. *Dalton Trans.* **2012**, *41*, 5526.

(39) Calculations including CH_3CN were referenced to 1_{Ms}-a_withCH_3CN, calculations without CH_3CN are referenced to 1_{Ms}-a.

(40) In one system, the incorporation of an explicit solvent molecule of acetonitrile was crucial for accurate representation the isomerization shown in Figure 2.15. The barriers for sulfonamide dissociation (**TS6**) and isomerization (**TS9**) (**7** → **10**) were 2.9 and 3.4 kcal·mol^{-1} higher, respectively, without explicit solvent. This effect can be rationalized by the stabilizing interaction of acetonitrile's lone pair with the cationic palladium center.

(41) Pathways leading to **1_{Ms}-c**, **1_{Ms}-d**, **1_{Ms}-e** from **1_{Ms}-b** were found to be higher in energy than those originating from **1_{Ms}-a.** These results are detailed in the SI.

(42) Since the reaction is zero order in sulfonamide and bpy doesn't have any effect in the C(sp^3)–N reductive elimination, we performed the calculations without the presence of exogeneous sulfonamide and bpy. Thus, we avoid the generation of intermediates and TS involving unproductive pathways and the analysis of those data that would require even more computer power and time.

(43) A single explicit solvent molecule or several (including sampling of the many possible solvent molecule arrangements) were attempted for each conformation. The lowest energy structures are reported.

(44) (a) Marquard, S. L.; Hartwig, J. F. *Angew. Chem. Int. Ed.* **2011**, *50*, 7119. (b) Marquard, S. L.; Rosenfeld, D. C.; Hartwig, J. F. *Angew. Chem. Int. Ed.* **2010**, *49*, 793.

(45) Sanford, M. S.; Groves, J. T. *Angew. Chem. Int. Ed.* **2004**, *43*, 588.

(46) For recent reviews detailing a combined computational and experimental approach to organometallic mechanisms, see: (a) Bonney, K. J.; Schoenebeck, F. *Chem. Soc. Rev.* **2014**, *43*, 6609. (b) Cheng, G.; Zhang, X.; Chung, L. W.; Xu, L.; Wu, Y. *J. Am. Chem. Soc.* **2015**, *137*, 1706–1725. (c) Jover, J.; Fey, N. *Chem. An Asian J.* **2014**, *9*, 1714. (d) Sperger, T.; Sanhueza, I. a.; Kalvet, I.; Schoenebeck, F. *Chem. Rev.* **2015**, *115*, 9532–9586.

Chapter 3: The Thermodynamic Landscape and Descriptors of Cobalt catalyzed CO_2 Reduction

3.1 Introduction

Towards using CO_2 as a C_1 carbon feedstock,[1–4] many homogenous catalysts have been developed to produce methanol, formic acid, or formate salts.[5–9] While large scale implementation of any CO_2 reduction process would likely need to utilize earth-abundant transition metals, such as Cu,[10] Ni,[11–16] Co,[17–21] and Fe,[21,22] some of the highest activity catalysts are currently based upon precious metals like Au,[23] Ir,[24–26] Re,[27] Rh,[28–30] and Ru.[31–37]. On the other hand, Linehan and coworkers reported that $Co(dmpe)_2H$ (dmpe = 1,2-Bis(dimethylphosphino)ethane) was highly efficient for CO_2 reduction to formate,[38] providing a promising example that could lead to a library of bis(diphosphine)-ligated cobalt catalysts.

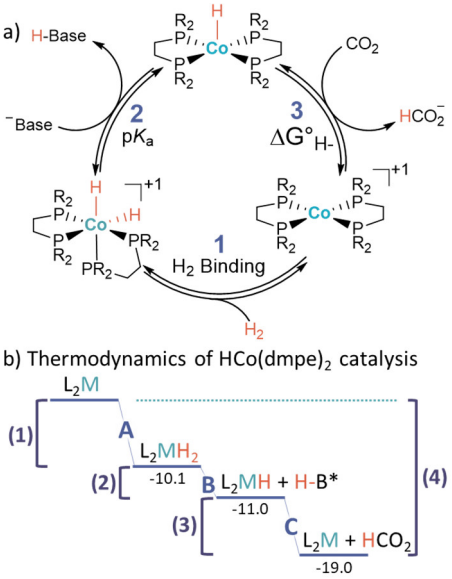

Figure 3.1. a) Catalytic cycle for CO_2 reduction by cobalt bis(diphosphine) metal complexes b) Free energy diagram for $Co(dmpe)_2H$ catalyzed CO_2 reduction using Verkade's base.

The catalytic cycle for CO_2 reduction using dihydrogen as a reducing agent is shown in Figure 3.1. The thermodynamics of this cycle depend upon the choice of base, solvent and ligand. The base provides a tunable thermodynamic force and modifying the solvent can change the free

energy of the overall process,[39] but modulating the ligands will not alter the overall spontaneity of a reaction (Figure 1b.). Instead, changes to the ligands can only shift the relative energy of intermediates within the catalytic cycle. Taking these factors into account, effective CO_2 reduction requires: (1) facile H_2 heterolysis, usually by the catalyst being sufficiently acidic to be paired with the selected base, and (2) metal-H hydricity for thermodynamically viable conversion of CO_2 to formate.

The $Co(dmpe)_2$ catalyst was reported as most efficient using stoichiometric Verkade's base to drive the catalytic cycle. With weaker bases such as 1,8-Diazabicyclo[5.4.0]undec-7-ene (DBU), higher pressures of CO_2 and H_2 were required to turn over catalysis. Using the same general mechanistic manifold (Figure 3.1), a subsequent report demonstrated an effective L_2NiH (where L=1,2-[bis(dimethoxypropyl)phosphino]ethane) complex which was demonstrated to successfully reduced CO_2 using water as a solvent.[16] While the reactivity of cobalt complexes are highly ligand dependent bis(diphosphine) ligand scaffolds seem to affect the reduction of CO_2 under various conditions.

In general, bis(diphosphine) ligand scaffolds are widely used and investigated ligand class in organometallic chemistry.[40] These ligands provide a range of reactivity and, owing to the widespread use, are commercially available. From a computational perspective, ligand screening systems have incorporated bidentate phosphines with the long-term goal of catalyst screening, optimization, and development of structure-activity relationships.[41,42] The impact of systematic ligand changes on cobalt catalyzed CO_2 reduction reactivity is not fully understood, owing in part to the difficulty associated with synthesis of novel metal phosphine complexes; only a limited number of these complexes are reported in the literature.[43–47] Computationally generated catalysts, derived from ligand libraries or taken from commercially inspired ligand scaffolds, can be used to extend beyond the synthetically available complexes to explore inaccessible chemical space.

The structure-energy relationships that underlie cobalt catalyzed CO_2 reduction can be studied using first principles simulations. Previous computational studies have explored a handful of PNP-type pincer complexes[48,49] for CO_2 reduction, and the present article is therefore in the same spirit. Specifically, this article explores the potential for tuning of Co-based CO_2 reduction catalysts using large libraries of bis-phosphine complexes. A benchmark set of thermodynamic data for heteroleptic metal bis-phosphines will permit evaluation of the relative capacity for CO_2 reduction for each complex, as well as indications of how the underlying catalyst structure dictates

reactivity. Therefore H_2 binding, deprotonation, and hydride transfer thermodynamic properties are examined for a large set of cobalt complexes, exploring both homoleptic and heteroleptic metal bis(diphosphines) constrained to a subset of all reported commercially bis(diphosphine) ligands.

3.2 Computational Benchmarking

To begin this investigation, a computational model is constructed to inform the three ligand-controlled steps of catalysis (Figure 3.1b). Here, three thermodynamic quantities hold particular interest: H_2 binding through oxidative addition to the transition metal, pK_a, and hydricity, all of which must be accurately quantified to form a useful model. Prior benchmark studies have examined pK_a for organometallic complexes[50,51–54] and found that density functional theory (DFT) approaches were sufficient to reproduce these quantities. To build our own model, a benchmark set was assembled to include eight cobalt and nickel bis(diphosphine) ligated metal complexes with experimentally reported pK_a values ranging from -2.3 to 38.[53,55–58,58,59] Comparisons were made between various simulation approaches with different DFT functionals, basis sets, solvation models, and thermodynamic corrections (see appendices for all comparisons). Gas phase DFT simulations overestimate energetic differences, but still linearly correlate (R^2 = 0.93) with experimental results. Implicit SMD solvation in acetonitrile results in a significantly more precise pK_a, but adding vibrational zero-point energy corrections reduces the correlation between computed and experimental. No substantial change in accuracy was observed when using DLPNO-CCSD(T) computations compared to DFT (ωB97X-D).

Prior reports on hydricity have shown it is more challenging to compute compared to pK_a.[60,61] The most accurate methods for calculating $\Delta G°_{H^-}$ have employed DFT with CPCM solvation models, resulting in only limited correlation with experimentally observed hydricities.[62] For benchmarking, a series of nine metal hydrides with experimental $\Delta G°_{H^-}$ values ranging from 31.8 to 66.3 kcal/mol[21,59,60,63–69] were selected. Similar to the pK_a benchmark, comparisons were made between various simulation approaches, and a single model chosen for general use (see appendices for full details). The solvation model was found to significantly impact precision of the results, as at the ωB97X-D/Def2-SVP level of theory SMD-PCM was observed to have an R^2=0.75 while Def2-SVP/CPCM R^2=0.89 and Def2-TZVP R^2=0.87 when compared to experiment (Figure 3.2). DLPNO-CCSD(T), using Def2-TZVP and Def-SVP basis sets, linearly correlates with DFT methods such as ωB97X-D (see appendices for details). These results indicate that using ωB97X-D/Def2-SVP/$PCM_{acetonitrile}$ would provide precise comparisons for calculating test set pK_a and hydricity values.

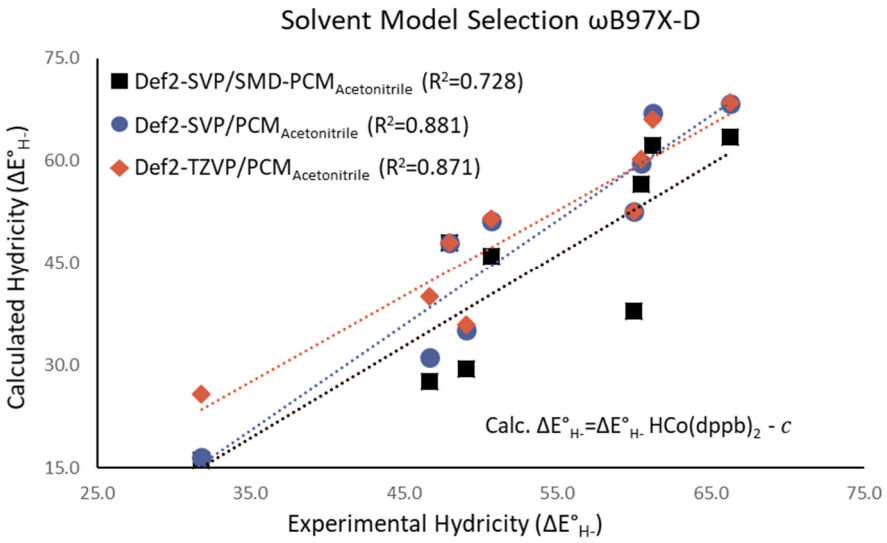

Figure 3.2. Experimental and calculated hydricity values using ωB97X-D/Def2-SVP level of theory comparing SMD-PCM $_{acetonitrile}$ and PCM$_{acetonitrile}$

Section 3.2.1 Bisphosphine Library and Thermodynamic Landscape

With a suitable computational method in hand, a library of heteroleptic cobalt complexes of the type Co(L)(L') was developed. As a first step, a series of bis(diphosphine) ligand scaffolds were selected with a range of electron withdrawing/donating effects, for example **16-dcpe** and **40-dpp(perfluoro)Bz** as electron acceptors, and electron donating ligands such as **19-d(4-methoxy-Ph)pe** and **36**. A variety of backbone linkers was also selected to intentionally vary parameters such as bite angle and cone angle. Commercially available phosphine ligands that were prohibitively large and/or prevented the formation of octahedral complexes were excluded (Figure 3).

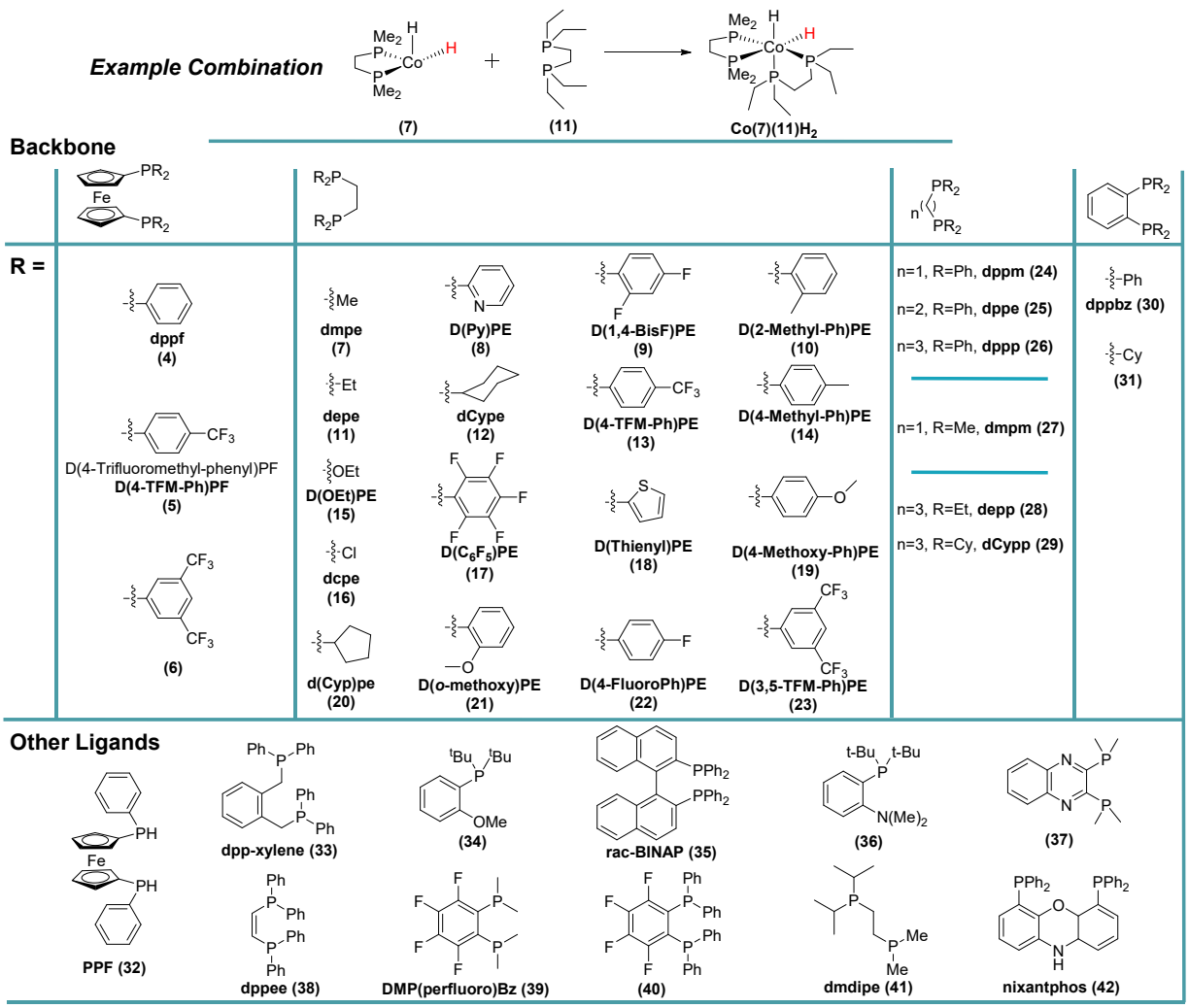

Abbreviations: Et=Ethyl, Ph=Phenyl, Cy=Cyclohexyl,1,1'-Bis(phenylphosphino)ferrocene=**ppf**, 1,2-bis((diphenylphosphanyl)methyl)benzene=**dppmb**, 2-(2-(di-tert-butylphosphosphanyl)ethyl)pyridine=**D(tBu)PPye**, 2,3-bis(dimethylphosphino)quinoxaline=**dmpq** 1,2-bis((dimethyl)(diisopropyl)phosphino)ethane=**dmdipe**

Figure 3.3. Outline of the bis(diphosphine) ligand library approach used for this study.

The catalyst library contains 780 unique cobalt complexes which were generated from the combination of pairs of ligands from Figure 3.3. Figure 3.4 illustrates the resulting thermodynamic landscape which compares H_2 binding, pK_a, and hydricity using the ωB97X-D/Def2-SVP/PCM$_{acetonitrile}$ level of theory. Figure 3.4 also illustrates how altering the solvation environment from acetonitrile to tetrahydrofuran (THF) results in a slight shift of the thermodynamic landscape toward more acidic and weaker hydride donor complexes.

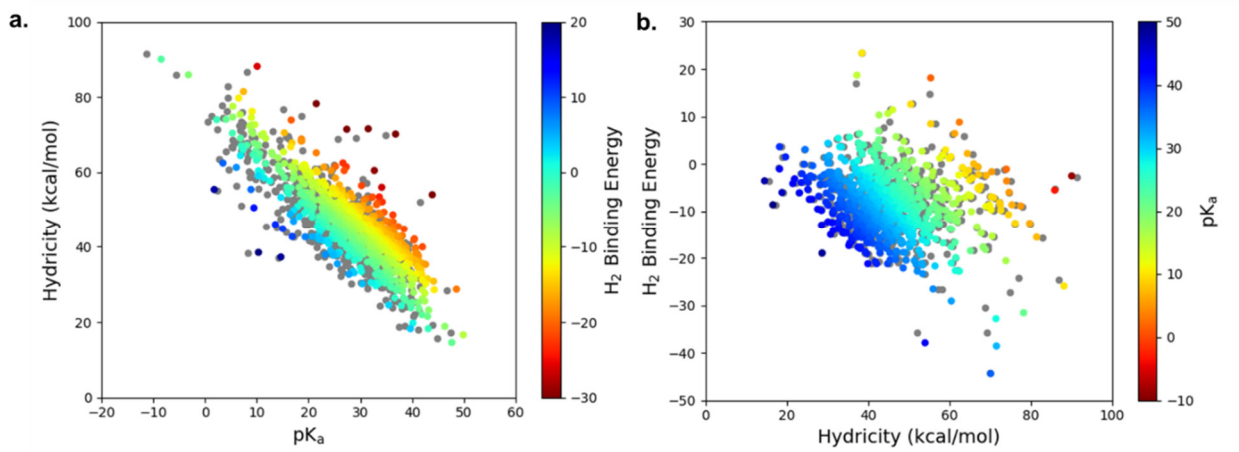

Figure 3.4 ωB97X-D/Def2-SVP/PCM$_{acetonitrile}$ thermodynamic landscape shown in color with ωB97X-D/Def2-SVP/PCM$_{THF}$ shown as a background in grey (a) Hydricity (kcal·mol^{-1}) versus pK_a with H_2 binding (kcal·mol^{-1}) on the Z-axis (b) Hydricity (kcal·mol^{-1}) versus H_2 binding (kcal·mol^{-1}) with pK_a on the Z-axis.

These results make clear that the thermodynamic values of hydricity, pK_a, and H_2 binding are dependent on one another. For example, the strong negative correlation between hydricity and pK_a illustrates electronic effects on the thermodynamic cycle of H_2 binding, deprotonation, and hydride loss. Strongly electron withdrawing groups are expected to reduce pK_a while increasing hydricity, whereas electron-donor phosphines result in a more electron-rich cobalt species which tend to be good hydride donors and weaker acids. Similarly, complexes that readily give up protons and hydrides with also have endothermic H_2 binding, while weak-hydride/weak-acid complexes are associated with more exothermic H_2 binding. A balance of these factors is required for the catalytic landscape to be as flat as possible, resulting in higher rates of CO_2 reduction.

Section 3.3 Qualitative assessment of the thermodynamic landscape

The Co complex library permits closer examination of chemical features which dictate trends in the energetic landscape. Upon identification of these features from a qualitative level, quantitative relationships will be built to better validate these descriptions. The extreme regions of the landscape—i.e. at high acidity or hydricity—were predominately governed by electronic properties of the ligands. For instance, **16-dcpe** was the predominant ligand found in the most acidic 10% of the thermodynamic landscape (Figure 3.5). Intuitively, the chlorine atoms bound to the phosphorous of **16-dcpe** make the complex electron deficient—and thus acidic. All 35 instances of ligand **16-dcpe** appear in the most acidic 50% of the landscape as well as the most

acidic complex in the test set. The electronic character of **16-dcpe** is further emphasized by Co(16)(16)H_2 with a calculated pK_a of -3.5 (this complex, were it to form, would be highly unstable). The most common ligand in the least acidic region of the thermodynamic landscape is the electron-donating **27-dmpm**. Complexes containing ligand **27** are almost exclusively limited to the least acidic half of the thermodynamic landscape (pK_a range 27.5 - 49.9). The only exception to this is Co(**27**)(**16**), where **16** overpowers the effect of **27**, resulting in a pK_a of 6.8, 20.7 pK_a units more acidic than the next complex containing ligand **27**.

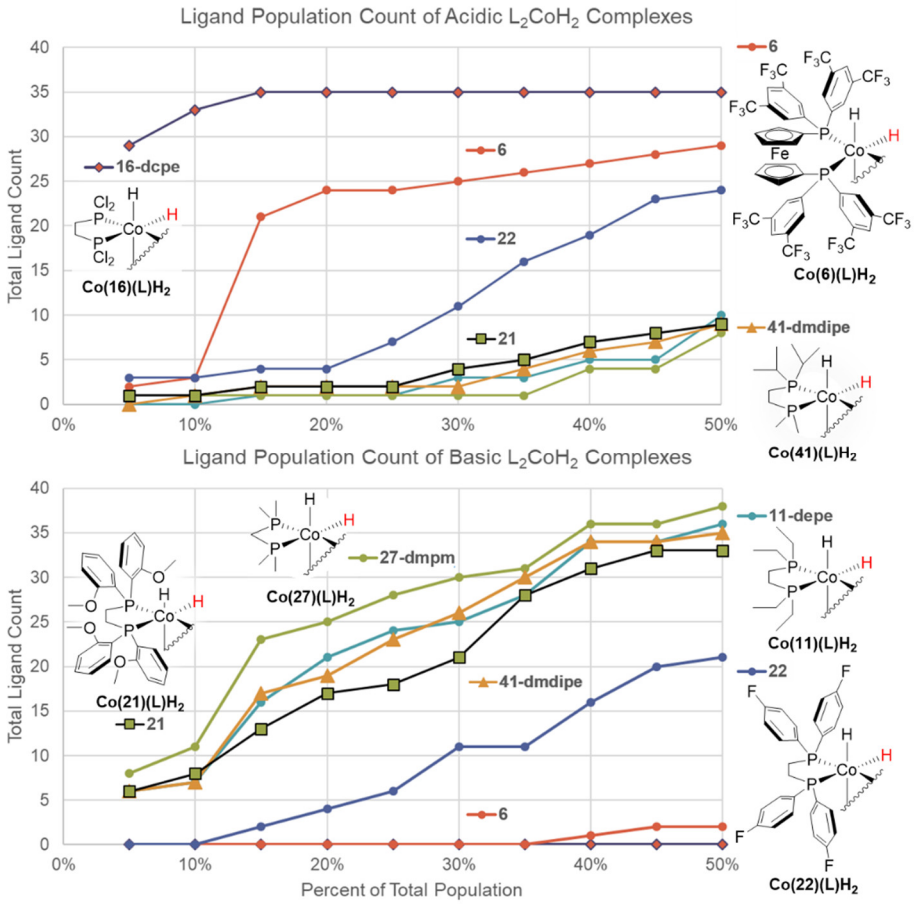

Figure 3.5. Quantitative analysis of ligand population for the (a) most-acidic and (b) least-acidic regions of the thermodynamic landscape

Moving on to the next thermodynamic property, a population analysis of hydricity indicates that ligands **21** and **36** predominate in the highly hydridic region of the thermodynamic landscape, shown in Figure 3.6. Electron donation from methoxy substituted arenes on ligand **21** and the direct σ donation from the lone pairs of nitrogen of ligand **36** result in reactive hydrides. In

comparison, the electron withdrawing groups on ligands **16-dcpe** and **6** are almost exclusively limited to the least hydridic half of the thermodynamic landscape. As expected by the negative correlation between pK_a and hydricity, no complexes containing ligand **16** are among the 50% most hydridic complexes.

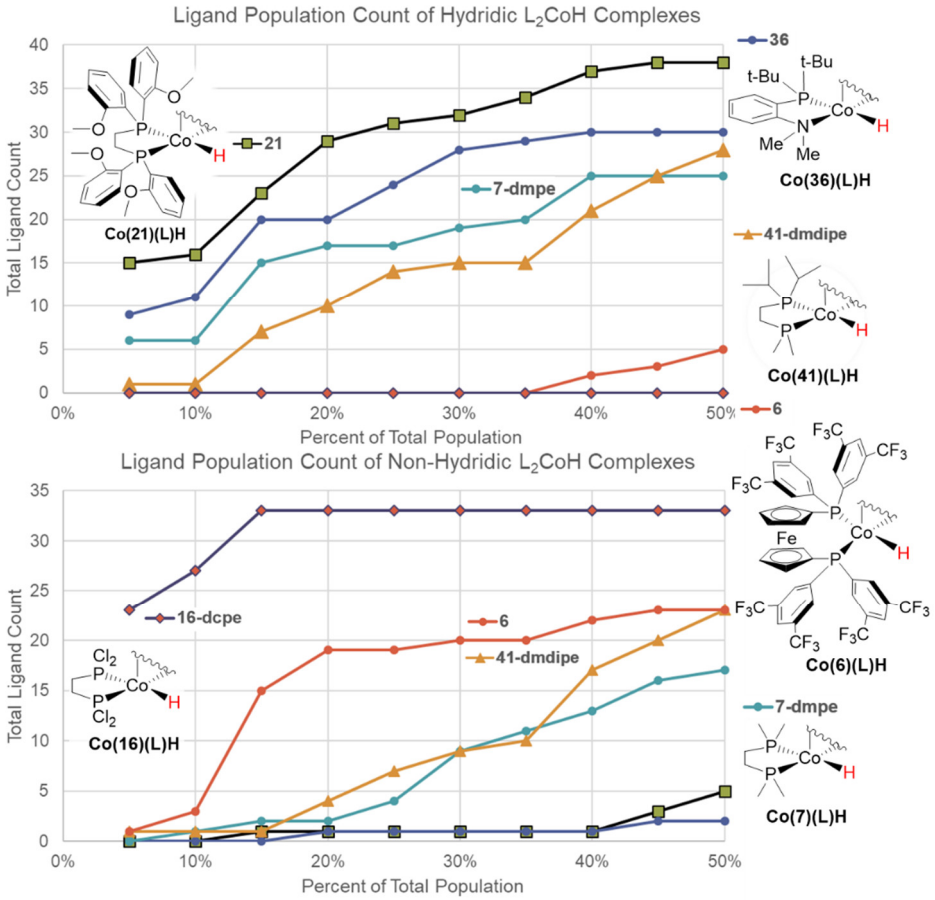

Figure 3.6. Quantitative analysis of ligand population in the (a) most hydridic and (b) least hydridic regions of the thermodynamic landscape

In general, significant overlap is expected between the high pK_a and strong hydride donor complexes within the bottom right of landscape shown in Figure 4a. A comparison of structures containing ligand **21** in this region helps to illustrate the interdependency of pKa, H_2 binding, and hydricity. The population of ligand **21** seems to be primarily distributed along the strong hydride donor window of the landscape, ranging from $\Delta G°_H$- 14.6 kcal/mol to 33.2 kcal/mol, with 15 instances among strong hydride donor complexes. When assessing the same number of complexes in a vertical window, ranging for pK_a 49.9 to 38.3, only 6 instances of ligand **21** are observed. The variation in population of complexes containing ligand **21** in the strong hydride window vs. high

pK_a window can be attributed to differences in H_2 binding; variation in hydricity while constraining pK_a is largely associated with H_2 binding energy. As the electronic environment of **21** is largely dominated by the electron donating methoxy substituents, a likely cause of the variation in H_2 binding is steric encumberment from the ligand paired with **21**. Qualitative steric analysis can be made through comparison of other common ligands within the most hydridic and high pK_a regions. Hydridic ligands **21** (ortho-methoxy substituents), **36** (t-butyl groups), and **41** (isopropyl groups) appear more sterically encumbered than basic ligands, **27** (methyl substituents), **11** (ethyl substituents) and **22** (*p*-fluoro). While not a complete explanation, these analyses suggest that H_2 binding and hydricity could be correlated with steric features of the molecule.

This qualitative assessment of the thermodynamic landscape has provided intuitive electronic factors that determine whether a given complex will exist in a proton-donating or hydride-donating region. Furthermore, the differences in the populations of ligands within each region indicate that further quantification of steric features could explain variations in the H_2 binding energy. In the next section of this article, specific molecular features are evaluated for their ability to describe structure-activity relationships in this landscape.

Section 3.4 Exploring Molecular Feature Based Descriptions of the Thermodynamic Landscape

The results of Section 3.1 suggest that regions of the landscape might be described by variation in electronic and steric features of the catalysts. We aimed to better understand which molecular features best describe variation in the thermodynamics of cobalt catalyzed CO_2 reduction. Toward this end, the multivariate regression know as LASSO (least absolute shrinkage and operator) was invoked. LASSO allows systematic evaluation of input features by penalizing terms with little influence on the accuracy of the resulting model. For instance, if a dataset were 2 dimensional in nature, but included 2 additional, low relevance or redundant features, LASSO would drop out the latter two features and give a regression with just 2 terms (i.e. $y = m_1x_1 + m_1x_2 + m_3x_3 + m_4x_4 \rightarrow y = m_1x_1 + m_3x_3$). Therefore, the following procedure was enacted: (1) Linear expressions with all (normalized) features were constructed, and (2) LASSO selects the best low-dimensional regressions for subsequent analysis. Important features for discussion are highlighted in Figure 3.7 below.

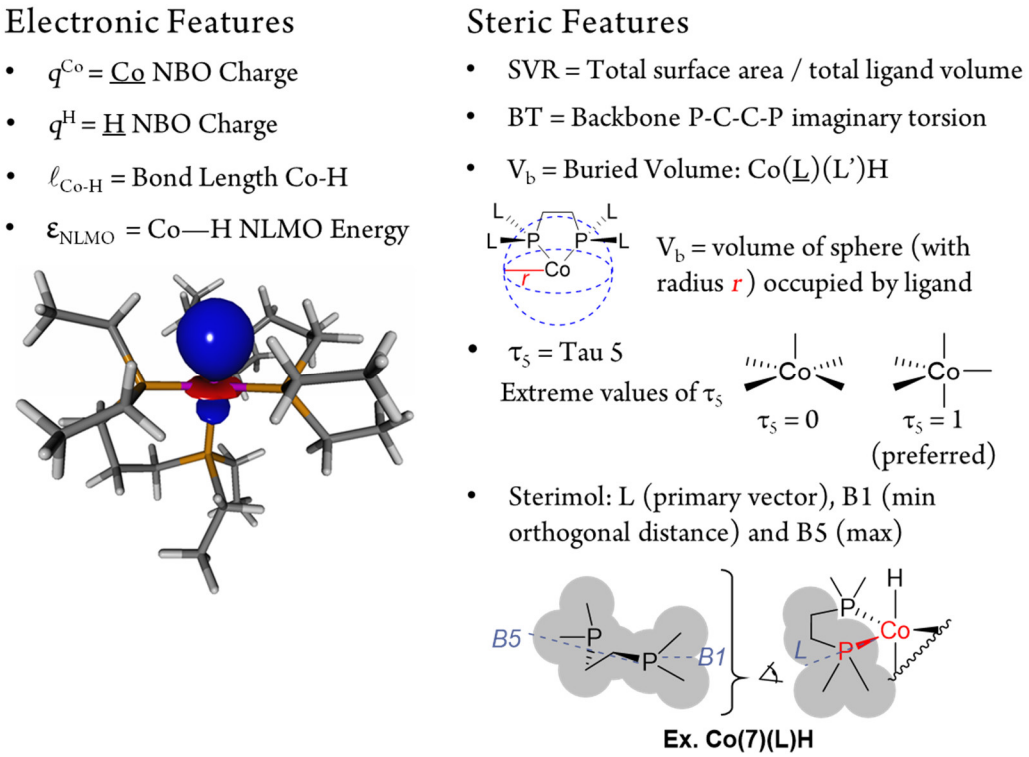

Figure 3.7. Features considered in constructing a molecular representation for pK_a and hydricity.

The intermediate Co(L)(L')H was selected as the target structure for the development of electronic and steric features. While steric features, such as buried volume and bite angle, are not expect to change significantly from the Co(L)(L')H_2 to Co(L)(L')H, we hypothesized that the electronic character of the Co—H hydride on Co(L)(L')H would be informative of both hydricity and acidity. For this study NBO atomic charges for cobalt and the metal hydride as well as the NLMO (natural bond orbital) energy and bond length for the Co—H bond in the Co(L)(L')H complex were included. Commonly cited steric features including, bite angle[70,71], total ligand area, total ligand volume, buried volume,[72] and Sterimol parameters *L*, *B1*, and *B5* were selected.[73] Bite angle has been called upon as a key molecular features in many organometallic QSAR studies, including past computational work by Guo and coworkers exploring relationships between structural features and metal bis(diphosphine) catalyzed CO_2 reduction.[61,70] Buried volume has been recently incorporated into QSAR studies for the purpose of characterizing steric bulk near the metal center of catalyst that could impact overall reaction yield[74] or enantioselectivity.[75] Sterimol parameters have been used widely throughout drug discovery chemistry[76] while recently experience a renaissance of sorts and now being more widely incorporated into the description of the steric properties for transition metal catalyzed chemical reactions.[75,77–80] Distortion around the Co(L)(L')H metal center was quantified by Tau 5 (trigonal bipyramidal distortion).[81]

As a first step in targeting a feature based representation for thermodynamics, the landscape was reduced to 487 complexes spanning a slightly narrower region of approximately 50 pK_a and 70 kcal/mol hydricity containing only alkenyl, aryl, and alkyl backbones. Specifically, catalysts with ferrocene backbones as well as Rac-BINAP (35), Nixantphos and ligand **33** were excluded in subsequent analyses. We hypothesized that by constraining the landscape to more closely related ligands, correlation between the structure and thermodynamics would be improved. Despite this initial constraint, the first analyses revealed that few of the commonly employed steric descriptors seemed to significantly contribute to the predictive value of the model. The best correlation between a feature based model versus QM calculated pK_a was identified as a 11 term model with an observed $R^2 = 0.78$ where the predominate features were the Co—H NLMO energy and NBO populations. However, in the absence of the electronic information provided by Co—H NLMO energy and NBO populations, the best correlation identified was an eight term model with an observed $R^2 = 0.40$. The poor correlation between the model in the absence of NBO data and the QM calculated pK_a strongly suggested that the molecular features such as bite angle, sterimol,

buried volume, and distortion, poorly describe statistical variance across large regions of chemical space. These data also suggested that out of the available features in our dataset the energy of the Co—H NLMO is the most correlative feature for describing the relative acidity and hydricity of a cobalt bis(diphosphine) complexes.

We next attempted to better understand the information provided by the Co—H NLMO energy. A linear regression of QM calculated pK_a versus NLMO energy produced an observed R^2 = 0.71 (Figure 3.8a) and an observed R^2 = 0.57 (Figure 3.8b) when hydricity was plotted versus NLMO energy. Importantly, the one term NLMO model only has an observed R^2 of 0.07 less than a 11 term model which included additional steric features as well as NBO populations on cobalt and the metal hydride.

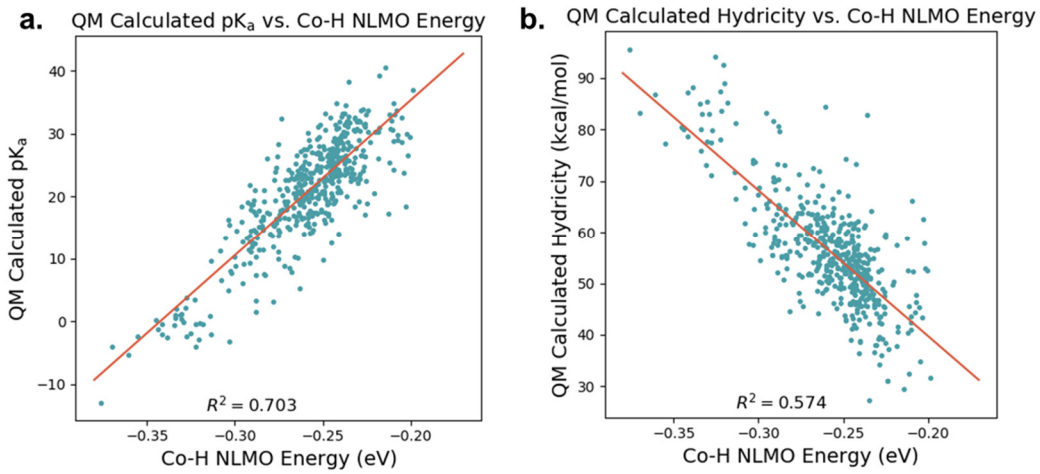

Figure 3.8. QM calculated (a) pK_a and (b) hydricity versus Co—H NLMO energy (eV)

$$pK_a = 247.7\varepsilon_{NLMO} + 84.8$$

Equation 3.1. Equation relating the ε_{NLMO} energy with pK_a shown in figure 3.8a

$$\Delta G^\circ_{H^-}\left(\frac{kcal}{mol}\right) = -284.5\varepsilon_{NLMO} - 17.1$$

Equation 3.2. Equation relating the ε_{NLMO} energy with hydricity shown in figure 3.8b

Though the NLMO is from the Co(L)(L')H intermediate, this orbital would still be expected to provided significant information regarding the hydricity and acidity of the metal complexes and would also be expected to contain some limited information regarding the energy of H_2 binding. For hydricity, these data suggest that the lower the Co—H bonding orbital energy, the more stable the Co—H bond, and the less labile the hydride. For acidity, the more stable the

Co—H NLMO, the more acidic the Co(L)(L')H_2 complex is expected to be. Figure 3.9 illustrates some of the possible shifts in the thermodynamics for hydricity, and pK_a through modulation of the NLMO energy.

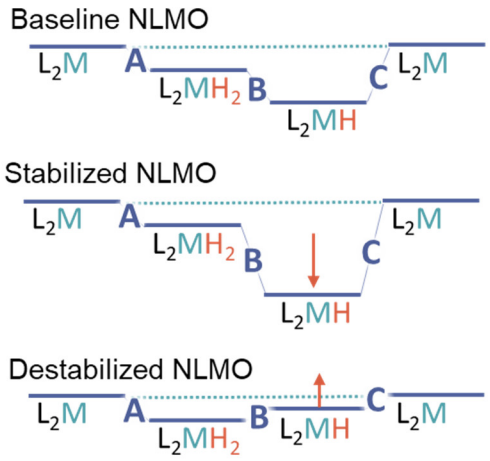

Figure 3.9. Illustration of effects on pK_a ***B*** and hydricity ***C*** caused by modulation of Co—H NLMO energies

What can clearly be observed is that the stability of the NLMO is intimately related to the acidity and hydricity. While the consideration of H_2 binding complicates the relationship between acidity and hydricity these can be reduced to two distinct classes, endothermic and exothermic H_2 binding: 1) If an H_2 binding process is highly exothermic then both hydricity and pK_a are less favorable 2) If the H_2 binding process is endothermic hydricity and pK_a will be more favorable. Notably, the characterization of the H_2 binding step seems to be most difficult to characterize using any combinations of features in our dataset. The best correlation for H_2 binding was observed for a 13 term model with an $R^2 = 0.46$ in which NBO populations on cobalt — from each of the three catalytic intermediates — were the most heavily weighted features. From these analyses we can conclude that the Co—H NLMO energy correlates with hydricity and pK_a across the entirety of the thermodynamic landscape and is crucial for the construction of a predictive model, even when only limited information regarding H_2 binding is available.

These data suggest that limited correlation exists between molecular features other than NLMO and NBO populations and thermodynamics within the dataset. Attempting to divide the landscape into smaller regions by pK_a, hydricity, H_2 binding, ligand scaffold, and even

constraining only to catalytically relevant regions provided little additional insight, but continuously suggested that the best overall feature was the localized Co—H NLMO descriptor.

Section 3.5. Selection of the Best Catalyst Using QM Calculations

We next set out to determine the most thermodynamically favorable catalysts according to QM data using two sequential thresholds for selection. The first reduction applied a thermodynamic cutoff, thereby considering only the most catalytically relevant species. As a point of reference, the thermodynamic values calculated for our dataset predict $Co(dmpe)_2H$ catalyst with a pK_a of 31.3, hydricity of 46.4, and a H_2 binding of -13.1 kcal/mol. More generally, in acetonitrile the hydride transfer to CO_2 is favorable for catalysts with < 44.0 kcal/mol calculated hydricity. For pK_a, we aimed to select catalysts more acidic or similar to previously reported $Co(dmpe)_2H$ catalyst. While there are some entropic penalties associated with H_2 binding, increasing the pressure of H_2 in these reactions seems to have little deleterious impact on catalysis.[82] Therefore, reactions that are less than -5.0 kcal/mol with respect to H_2 binding seemed reasonable to include. Based on these metrics we bounded the selection to only catalysts favorable H_2 binding, hydride transfer to CO_2 in acetonitrile and to catalysts that were similar or more acidic than calculated values for $Co(dmpe)_2H_2$. An overview of stepwise reduction of the thermodynamic landscape, and the selection of best case catalysts from each step, is shown in Figure 3.10.

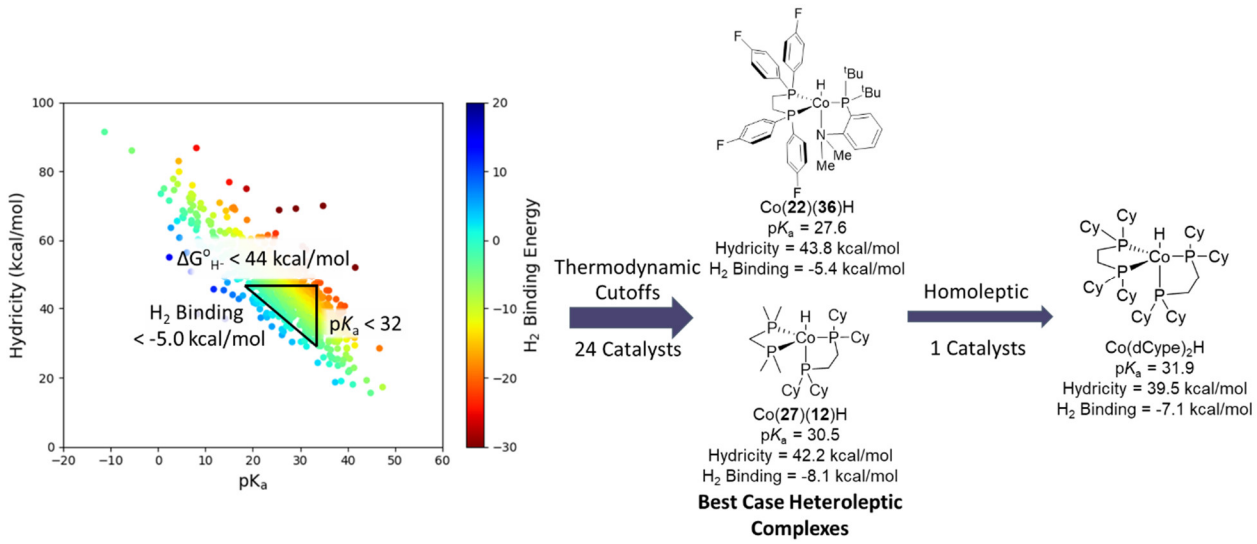

Figure 3.10. Stepwise reduction of the thermodynamic landscape toward the selection of best-case catalysts.

In total we observed only 24 species inside the constrained region of the thermodynamic landscape. While the synthetic tractability of the heteroleptic complexes limits experimental study, the surprising lack of complexes within the windows illustrates the challenge associated with selecting ligands capable of balancing the desired thermodynamic parameters. During our assessment of the ligand population we identified that complexes generally considered to be electron donating were primarily associated with strong hydride donor complexes. Similarly, our regression analysis also pointed toward the correlation between a high energy Co—H NLMO and stronger hydride donors. Taken together these data would suggest destabilizing the NLMO through electron donation would be expected to postion complexes in a region far from the catalytically active window. The top ten thermodynamically relevant catalysts are presented in table 3.1 entries 1-10 along with catalytically competent cobalt complexes table 3.1 entries 11-13.

General Octahedral Structure: $Co(L)(L')H_2$

Entry	L	L'	pK_a	ΔH°_{H-}	H_2 Binding
1	36	22	27.6	43.8	-5.4
2	27	12	30.5	42.4	-8.1
3	25	7	30.6	42.8	-8.6
4	35	27	30.6	43.0	-8.7
5	14	27	30.7	44.2	-10.2
6	19	27	30.8	44.2	-10.2
7	36	20	30.9	40.7	-6.8
8	34	11	31.1	44.2	-10.5
9	24	36	31.8	38.0	-5.4
10	12	12	31.9	39.5	-7.1
11	11	11	33.2	45.8	-15.0
12	7	7	31.3	46.4	-13.1
13	25	25	22.8	49.1	-4.2

Table 3.1 Entries 1-10 show the top thermodynamically relevant $Co(L)(L')H_2$ complexes from the landscape while entries 11-13 highlight catalytically competent homoleptic catalysts

We observed that the most favorable catalysts within the window contain ligands characterized as electron neutral, dCype (**12**), dmpm (**27**), dmpe (**7**), or combinations of electron withdrawing and electron donating ligands such as Co(**22**)(**36**)H_2. The electron donating and electron withdrawing properties of the ligands must be in balance such that heteroleptic complex remains in the catalytic region of interest. Neutral ligands are thereby more likely to be in the center of the landscape closest to the region of catalytic interest. These data also suggest that seemingly subtle changes to ligand environment, such as shifting from alkyl to aryl substituted phosphines, has a large impact on the acidity, hydricity and H_2 binding character of the complexes. For example, shifting from $Co(dCype)_2H_2$ to $Co(dppe)_2H_2$ (table 3.1 entry 13) results in an almost 10 kcal/mol difference in the calculated values for hydricity.

Based on our analysis of the landscape the most thermodynamically favorable homoleptic complex is the $Co(dCype)_2H_2$. This complex is calculated to be relatively more acidic and hydridic than the previously reported $Co(dmpe)_2H_2$, or $Co(depe)_2H$ catalysts (table 3.1 entries 11-12).[83] The H_2 binding energy for the $Co(dCype)_2H_2$ catalyst is calculated to be more endothermic than the $Co(dmpe)_2H_2$ catalyst by 7.9 kcal/mol, showing that the cyclohexyl substituted phosphine results in substantial energetic difference when compared to simpler alkyl ligands. Observed differences in the binding energy accounts for thermodynamic favorability of deprotonation and hydride transfer for the $Co(dCype)_2H$ catalyst, an effect which could be attributed to the more crowded steric environment around the metal center.

These analysis suggest that potential complexes for cobalt bis(diphosphine) catalysts are highly sensitive to the electronic character of the ligands. Only a few combinations of ligands within the landscape have the properties necessary to aptly balance the thermodynamics for each step of the catalytic process. Despite the limited number of complexes in this region of the landscape, we identified the $Co(dCype)_2H_2$ as an important target for further experimental investigation. This complex has not yet been experimentally reported, but is associated with a more endothermic H_2 binding process than previously reported $Co(dmpe)_2H$ while maintaining what would appear to be superficially similar electronic character. The net result is that the $Co(dCype)_2H_2$ complex is overall the most thermodynamically favorable and potentially synthesizable catalyst in the landscape.

Section 3.6. Conclusions

In this article we demonstrate a step-wise approach to development of a computational chemical library from benchmarked experimental data and description of a thermodynamic landscape. Our dataset consisted of Co(L)(L')H_2 type complexes generated from set of commercially available of bis(diphosphines) which covered a thermodynamic landscape of over 50 orders of magnitude acidity and hydricity. Overall, the diversity of complexes in this landscape has provided unique insight into limited ability to quantify ligand interactions using traditional steric and electronic features. The attempted use of traditionally employed steric and electronic molecular features revealed that these parameters seem to have little statistical correlation with the thermodynamics of CO_2 reduction for cobalt bis(diphosphine) complexes. From this dataset we found a single highly correlative electronic feature, the Co—H NLMO bond energy, which alone provided an observed $R^2 = 0.70$ for pK_a and an observed $R^2 = 0.54$ for hydricity. Using the quantum chemical dataset we were able to extract and interpret the best catalysts from the landscape. We identified the Co(dCype)$_2$H catalyst as the most catalytically relevant species. In summary, ligand population and NLMO analysis both suggest that presence of neutral ligands appears to position complexes in the region of catalytic interest while ligands with electronic character shift the complexes toward the extreme edges of the landscape. Work remains in the development of molecular features which aptly describe the steric environment around cobalt bis(diphosphines) specifically pertaining to H_2 binding.

3.7 Computational Details

A detailed account of the methods used throughout this publication can be found in appendix B. This investigation utilized B3LYP[84], B3P86, and ωB97X-D[85] density functions, as well as the DLPNO-CCSD(T)[86] method. Utilized basis sets include: LANL2DZ[87,88] Def2-SVP[89], Def2TZVP, and ma-Def2-SVP. Solvation methods: SMD-PCM[90] and CPCM[91–93]. Software packages include: QChem[94] and Orca[95].

3.8 References

(1) Aresta, M.; Dibenedetto, A. Utilisation of CO_2 as a Chemical Feedstock: Opportunities and Challenges. *Dalt. Trans.* **2007**, No. 28, 2975.

(2) He, L.-N.; Wang, J.-Q.; Wang, J.-L. Carbon Dioxide Chemistry: Examples and Challenges in Chemical Utilization of Carbon Dioxide. *Pure Appl. Chem.* **2009**, *81* (11).

(3) Appel, A. M.; Bercaw, J. E.; Bocarsly, A. B.; Dobbek, H.; Dubois, D. L.; Dupuis, M.; Ferry, J. G.; Fujita, E.; Hille, R.; Kenis, P. J. a; et al. Frontiers, Opportunities, and Challenges in Biochemical and Chemical Catalysis of CO_2 Fixation. *Chem. Rev.* **2013**, *113* (8), 6621–6658.

(4) Abelson, P. H. Limiting Atmospheric CO_2. *Science* **2000**, *289* (5483), 1293–1293.

(5) Federsel, C.; Jackstell, R.; Beller, M. State-of-the-Art Catalysts for Hydrogenation of Carbon Dioxide. *Angew. Chemie Int. Ed.* **2010**, *49* (36), 6254–6257.

(6) Saeidi, S.; Amin, N. A. S.; Rahimpour, M. R. Hydrogenation of CO_2 to Value-Added products—A Review and Potential Future Developments. *J. CO2 Util.* **2014**, *5*, 66–81.

(7) Sakakura, T.; Choi, J.-C.; Yasuda, H. Transformation of Carbon Dioxide. *Chem. Rev.* **2007**, *107* (6), 2365–2387.

(8) Wang, W.-H.; Himeda, Y.; Muckerman, J. T.; Manbeck, G. F.; Fujita, E. CO_2 Hydrogenation to Formate and Methanol as an Alternative to Photo- and Electrochemical CO_2 Reduction. *Chem. Rev.* **2015**, *115* (23), 12936–12973.

(9) Wang, W.; Wang, S.; Ma, X.; Gong, J. Recent Advances in Catalytic Hydrogenation of Carbon Dioxide. *Chem. Soc. Rev.* **2011**, *40* (7), 3703.

(10) Yuan, R.; Lin, Z. Mechanism for the Carboxylative Coupling Reaction of a Terminal Alkyne, CO_2 , and an Allylic Chloride Catalyzed by the Cu(I) Complex: A DFT Study. *ACS Catal.* **2014**, *4* (12), 4466–4473.

(11) Li, J.; Lin, Z. Density Functional Theory Studies on the Reduction of CO_2 to CO by a (NHC)Ni^0 Complex. *Organometallics* **2009**, *28* (14), 4231–4234.

(12) Song, J.; Klein, E. L.; Neese, F.; Ye, S. The Mechanism of Homogeneous CO_2 Reduction by Ni(cyclam): Product Selectivity, Concerted Proton–Electron Transfer and C–O Bond Cleavage. *Inorg. Chem.* **2014**, *53* (14), 7500–7507.

(13) Ríos, P.; Rodríguez, A.; López-Serrano, J. Mechanistic Studies on the Selective Reduction of CO_2 to the Aldehyde Level by a Bis(phosphino)boryl (PBP)-Supported Nickel Complex. *ACS Catal.* **2016**, *6* (9), 5715–5723.

(14) Yuan, R.; Lin, Z. Computational Insight into the Mechanism of Nickel-Catalyzed Reductive Carboxylation of Styrenes Using CO_2. *Organometallics* **2014**, *33* (24), 7147–7156.

(15) Wang, W.; Wang, S.; Ma, X.; Gong, J. Recent Advances in Catalytic Hydrogenation of Carbon Dioxide. *Chem. Soc. Rev.* **2011**, *40* (7), 3703–3727.

(16) Burgess, S. A.; Kendall, A. J.; Tyler, D. R.; Linehan, J. C.; Appel, A. M. Hydrogenation of CO_2 in Water Using a Bis(diphosphine) Ni–H Complex. *ACS Catal.* **2017**, *7* (4), 3089–3096.

(17) Ge, H.; Jing, Y.; Yang, X. Computational Design of Cobalt Catalysts for Hydrogenation of Carbon Dioxide and Dehydrogenation of Formic Acid. *Inorg. Chem.* **2016**, *55* (23), 12179–12184.

(18) Jeletic, M. S.; Helm, M. L.; Hulley, E. B.; Mock, M. T.; Appel, A. M.; Linehan, J. C. A Cobalt Hydride Catalyst for the Hydrogenation of CO_2 : Pathways for Catalysis and Deactivation. *ACS Catal.* **2014**, *4* (10), 3755–3762.

(19) Kumar, N.; Camaioni, D. M.; Dupuis, M.; Raugei, S.; Appel, A. M. Mechanistic Insights into Hydride Transfer for Catalytic Hydrogenation of CO_2 with Cobalt Complexes. *Dalt. Trans.* **2014**, *43* (31), 11803.

(20) Spentzos, A. Z.; Barnes, C. L.; Bernskoetter, W. H. Effective Pincer Cobalt Precatalysts for Lewis Acid Assisted CO_2 Hydrogenation. *Inorg. Chem.* **2016**, *55* (16), 8225–8233.

(21) Mondal, B.; Neese, F.; Ye, S. Toward Rational Design of 3d Transition Metal Catalysts for CO_2 Hydrogenation Based on Insights into Hydricity-Controlled Rate-Determining Steps. *Inorg. Chem.* **2016**, *55* (11), 5438–5444.

(22) Ren, Q.; Wu, N.; Cai, Y.; Fang, J. DFT Study of the Mechanisms of Iron-Catalyzed Regioselective Synthesis of α-Aryl Carboxylic Acids from Styrene Derivatives and CO_2. *Organometallics* **2016**, *35* (23), 3932–3938.

(23) Yuan, R.; Lin, Z. Mechanistic Insight into the Gold-Catalyzed Carboxylative Cyclization of Propargylamines. *ACS Catal.* **2015**, *5* (5), 2866–2872.

(24) Yang, X. Hydrogenation of Carbon Dioxide Catalyzed by PNP Pincer Iridium, Iron, and Cobalt Complexes: A Computational Design of Base Metal Catalysts. *ACS Catal.* **2011**, *1* (8), 849–854.

(25) Li, J.; Yoshizawa, K. Catalytic Hydrogenation of Carbon Dioxide with a Highly Active Hydride on Ir(III)–Pincer Complex: Mechanism for CO_2 Insertion and Nature of Metal–Hydride Bond. *Bull. Chem. Soc. Jpn.* **2011**, *84* (10), 1039–1048.

(26) Tanaka, R.; Tanaka, R.; Yamashita, M.; Yamashita, M.; Nozaki, K.; Nozaki, K. Catalytic Hydrogenation of Carbon Dioxide Using Ir(III)-Pincer Complexes. *J. Am. Chem. Soc.* **2009**, *131* (40), 14168–14169.

(27) Agarwal, J.; Johnson, R. P.; Li, G. Reduction of CO_2 on a Tricarbonyl Rhenium(I) Complex: Modeling a Catalytic Cycle. *J. Phys. Chem. A* **2011**, *115* (13), 2877–2881.

(28) Hou, C.; Jiang, J.; Zhang, S.; Wang, G.; Zhang, Z.; Ke, Z.; Zhao, C. Hydrogenation of Carbon Dioxide Using Half-Sandwich Cobalt, Rhodium, and Iridium Complexes: DFT Study on the Mechanism and Metal Effect. *ACS Catal.* **2014**, *4* (9), 2990–2997.

(29) Huang, K.-W.; Han, J. H.; Musgrave, C. B.; Fujita, E. Carbon Dioxide Reduction by Pincer Rhodium η2-Dihydrogen Complexes: Hydrogen-Binding Modes and Mechanistic Studies by Density Functional Theory Calculations. *Organometallics* **2007**, *26* (3), 508–513.

(30) Hutschka, F.; Dedieu, A.; Eichberger, M.; Fornika, R.; Leitner, W. Mechanistic Aspects of the Rhodium-Catalyzed Hydrogenation of CO_2 to Formic Acid: A Theoretical and Kinetic Study † , ‖. *J. Am. Chem. Soc.* **1997**, *119* (19), 4432–4443.

(31) Bontemps, S.; Vendier, L.; Sabo-Etienne, S. Ruthenium-Catalyzed Reduction of Carbon Dioxide to Formaldehyde. *J. Am. Chem. Soc.* **2014**, *136* (11), 4419–4425.

(32) Filonenko, G. A.; Conley, M. P.; Copéret, C.; Lutz, M.; Hensen, E. J. M.; Pidko, E. A. The Impact of Metal–Ligand Cooperation in Hydrogenation of Carbon Dioxide Catalyzed by Ruthenium PNP Pincer. *ACS Catal.* **2013**, *3* (11), 2522–2526.

(33) Filonenko, G. A.; Smykowski, D.; Szyja, B. M.; Li, G.; Szczygieł, J.; Hensen, E. J. M.; Pidko, E. A. Catalytic Hydrogenation of CO 2 to Formates by a Lutidine-Derived Ru-C-N-C Pincer Complex: Theoretical Insight into the Unrealized Potential. *ACS Catal.* **2015**, *5* (2), 1145–1154.

(34) Getty, A. D.; Tai, C.-C.; Linehan, J. C.; Jessop, P. G.; Olmstead, M. M.; Rheingold, A. L. Hydrogenation of Carbon Dioxide Catalyzed by Ruthenium Trimethylphosphine Complexes: A Mechanistic Investigation Using High-Pressure NMR Spectroscopy. *Organometallics* **2009**, *28* (18), 5466–5477.

(35) Gunanathan, C.; Milstein, D. Bond Activation and Catalysis by Ruthenium Pincer Complexes. *Chem. Rev.* **2014**, *114* (24), 12024–12087.

(36) Huff, C. A.; Sanford, M. S. Catalytic CO_2 Hydrogenation to Formate by a Ruthenium Pincer Complex. *ACS Catal.* **2013**, *3* (10), 2412–2416.

(37) Namura, K.; Ohashi, M.; Suzuki, H. Synthesis and Structure of a Mixed-Ligand Dinuclear Ruthenium Trihydrido Complex Supported by Cn* and Cp* Ligands (Cn* = 1,4,7-Trimethyl-1,4,7-Triazacyclononane, Cp* = η 5 -C 5 Me 5): Enhancement of Reactivity toward CO_2 by Introduction of the Cn* Ligan. *Organometallics* **2012**, *31* (17), 5979–5982.

(38) Jeletic, M. S.; Mock, M. T.; Appel, A. M.; Linehan, J. C. A Cobalt-Based Catalyst for the Hydrogenation of CO_2 under Ambient Conditions. *J. Am. Chem. Soc.* **2013**, *135* (31), 11533–11536.

(39) Burgess, S. A.; Appel, A. M.; Linehan, J. C.; Wiedner, E. S. Changing the Mechanism for CO_2 Hydrogenation Using Solvent-Dependent Thermodynamics. *Angew. Chemie Int. Ed.* **2017**.

(40) Birkholz (née Gensow), M.-N.; Freixa, Z.; van Leeuwen, P. W. N. M. Bite Angle Effects of Diphosphines in C–C and C–X Bond Forming Cross Coupling Reactions. *Chem. Soc. Rev.* **2009**, *38* (4), 1099.

(41) Jover, J.; Fey, N.; Harvey, J. N.; Lloyd-Jones, G. C.; Orpen, A. G.; Owen-Smith, G. J. J.; Murray, P.; Hose, D. R. J.; Osborne, R.; Purdie, M. Expansion of the Ligand Knowledge Base for Chelating P,P-Donor Ligands (LKB-PP). *Organometallics* **2012**, *31* (15), 5302–5306.

(42) Fey, N.; Papadouli, S.; Pringle, P. G.; Ficks, A.; Fleming, J. T.; Higham, L. J.; Wallis, J. F.; Carmichael, D.; Mézailles, N.; Müller, C. Setting P-Donor Ligands into Context: An Application of the Ligand Knowledge Base (LKB) Approach. *Phosphorus. Sulfur. Silicon Relat. Elem.* **2015**, *190* (5–6), 706–714.

(43) DuBois, D. L.; Miedaner, A. Synthesis, Characterization, and Electrochemical Studies of Iron, Cobalt, and Nickel Complexes of Polyphosphine Ligands. *Inorg. Chem.* **1986**, *25* (26), 4642–4650.

(44) Nakajima, M.; Saito, T.; Kobayashi, A.; Sasaki, Y. Crystal and Molecular Structure of a Paramagnetic Hydridotetrahydro-Borato-Complex of Cobalt: Hydridotetrahydroboratobis(tricyclohexylphosphine)cobalt. *J. Chem. Soc. Dalt. Trans.* **1977**, No. 4, 385.

(45) Schunn, R. A. Interaction of Transition Metal Hydride Complexes with Deuterium, Ethylene-d4, and 1-Butene. *Inorg. Chem.* **1970**, *9* (11), 2567–2572.

(46) Structures, M.; Ch, C. O. B. H. P.; Parkerib, K. Reactions of Cobalt (I1) with $NaBH_4$ in the Presence of Bidentate Phosphines : Crystal. **2003**, *3*, 3956–3962.

(47) Mock, M. T.; Potter, R. G.; Hagan, M. J. O.; Camaioni, D. M.; Dougherty, W. G.; Kassel, W. S.; Dubois, D. L.; Northwest, P.; Box, P. O.; States, U. Synthesis and Hydride Transfer Reactions of Cobalt and Nickel Hydride Complexes to BX_3 Compounds. **2011**.

(48) Ge, H.; Jing, Y.; Yang, X. Computational Design of Cobalt Catalysts for Hydrogenation of Carbon Dioxide and Dehydrogenation of Formic Acid. *Inorg. Chem.* **2016**, *55* (23), 12179–12184.

(49) Chen, X.; Ge, H.; Yang, X. Newly Designed Manganese and Cobalt Complexes with Pendant Amines for the Hydrogenation of CO_2 to Methanol: A DFT Study. *Catal. Sci. Technol.* **2017**, *7* (2), 348–355.

(50) Qi, X.-J.; Liu, L.; Fu, Y.; Guo, Q.-X. Ab Initio Calculations of pK_a Values of Transition-Metal Hydrides in Acetonitrile. *Organometallics* **2006**, *25* (25), 5879–5886.

(51) Chen, S.; Ho, M.-H.; Bullock, R. M.; DuBois, D. L.; Dupuis, M.; Rousseau, R.; Raugei, S. Computing Free Energy Landscapes: Application to Ni-Based Electrocatalysts with Pendant Amines for H_2 Production and Oxidation. *ACS Catal.* **2014**, *4* (1), 229–242.

(52) Morris, R. H. Brønsted–Lowry Acid Strength of Metal Hydride and Dihydrogen Complexes. *Chem. Rev.* **2016**, *116* (15), 8588–8654.

(53) Wiedner, E. S.; Appel, A. M.; DuBois, D. L.; Bullock, R. M. Thermochemical and Mechanistic Studies of Electrocatalytic Hydrogen Production by Cobalt Complexes Containing Pendant Amines. *Inorg. Chem.* **2013**, *52* (24), 14391–14403.

(54) Chen, S.; Raugei, S.; Rousseau, R.; Dupuis, M.; Bullock, R. M. Homogeneous Ni Catalysts for H_2 Oxidation and Production: An Assessment of Theoretical Methods, from Density Functional Theory to Post Hartree−Fock Correlated Wave-Function Theory. *J. Phys. Chem. A* **2010**, *114* (48), 12716–12724.

(55) Matsui, T.; Shigeta, Y.; Morihashi, K. Assessment of Methodology and Chemical Group Dependences in the Calculation of the pK_a for Several Chemical Groups. *J. Chem. Theory Comput.* **2017**, *13* (10), 4791–4803.

(56) Curtis, C. J.; Miedaner, A.; Ellis, W. W.; DuBois, D. L. Measurement of the Hydride Donor Abilities of $[HM(diphosphine)_2]^+$ Complexes (M = Ni, Pt) by Heterolytic Activation of Hydrogen. *J. Am. Chem. Soc.* **2002**, *124* (9), 1918–1925.

(57) Chen, S.; Rousseau, R.; Raugei, S.; Dupuis, M.; DuBois, D. L.; Bullock, R. M. Comprehensive Thermodynamics of Nickel Hydride Bis(Diphosphine) Complexes: A Predictive Model through Computations. *Organometallics* **2011**, *30* (22), 6108–6118.

(58) Rakowski DuBois, M.; DuBois, D. L. The Roles of the First and Second Coordination Spheres in the Design of Molecular Catalysts for H_2 Production and Oxidation. *Chem. Soc. Rev.* **2009**, *38* (1), 62–72.

(59) Ciancanelli, R.; Noll, B. C.; DuBois, D. L.; DuBois, M. R. Comprehensive Thermodynamic Characterization of the Metal−Hydrogen Bond in a Series of Cobalt-Hydride Complexes. *J. Am. Chem. Soc.* **2002**, *124* (12), 2984–2992.

(60) Kovács, G.; Pápai, I. Hydride Donor Abilities of Cationic Transition Metal Hydrides from DFT-PCM Calculations. *Organometallics* **2006**, *25* (4), 820–825.

(61) Qi, X.-J.; Fu, Y.; Liu, L.; Guo, Q.-X. Ab Initio Calculations of Thermodynamic Hydricities of Transition-Metal Hydrides in Acetonitrile. *Organometallics* **2007**, *26* (17), 4197–4203.

(62) Wiedner, E. S.; Chambers, M. B.; Pitman, C. L.; Bullock, R. M.; Miller, A. J. M.; Appel, A. M. Thermodynamic Hydricity of Transition Metal Hydrides. *Chem. Rev.* **2016**, *116* (15), 8655–8692.

(63) Mock, M. T.; Potter, R. G.; O'Hagan, M. J.; Camaioni, D. M.; Dougherty, W. G.; Kassel, W. S.; DuBois, D. L. Synthesis and Hydride Transfer Reactions of Cobalt and Nickel Hydride Complexes to BX_3 Compounds. *Inorg. Chem.* **2011**, *50* (23), 11914–11928.

(64) Price, A. J.; Ciancanelli, R.; Noll, B. C.; Curtis, C. J.; DuBois, D. L.; DuBois, M. R. $HRh(dppb)_2$, a Powerful Hydride Donor. *Organometallics* **2002**, *21* (22), 4833–4839.

(65) Jeletic, M. S.; Hulley, E. B.; Helm, M. L.; Mock, M. T.; Appel, A. M.; Wiedner, E. S.; Linehan, J. C. Understanding the Relationship Between Kinetics and Thermodynamics in CO_2 Hydrogenation Catalysis. *ACS Catal.* **2017**, 6008–6017.

(66) Berning, D. E.; Miedaner, A.; Curtis, C. J.; Noll, B. C.; Rakowski DuBois, M. C.; DuBois, D. L. Free-Energy Relationships between the Proton and Hydride Donor Abilities of $[HNi(diphosphine)_2]^+$ Complexes and the Half-Wave Potentials of Their Conjugate Bases. *Organometallics* **2001**, *20* (9), 1832–1839.

(67) Connelly Robinson, S. J.; Zall, C. M.; Miller, D. L.; Linehan, J. C.; Appel, A. M. Solvent Influence on the Thermodynamics for Hydride Transfer from Bis(diphosphine) Complexes of Nickel. *Dalt. Trans.* **2016**, *45* (24), 10017–10023.

(68) Elgrishi, N.; Kurtz, D. A.; Dempsey, J. L. Reaction Parameters Influencing Cobalt Hydride Formation Kinetics: Implications for Benchmarking H_2-Evolution Catalysts. *J. Am. Chem. Soc.* **2017**, *139* (1), 239–244.

(69) Glezakou, V.-A.; Rousseau, R.; Elbert, S. T.; Franz, J. A. Trends in Homolytic Bond Dissociation Energies of Five- and Six-Coordinate Hydrides of Group 9 Transition Metals: Co, Rh, Ir. *J. Phys. Chem. A* **2017**, acs.jpca.6b11655.

(70) Dierkes, P.; van Leeuwen, P. W. N. M. The Bite Angle Makes the Difference: A Practical Ligand Parameter for Diphosphine Ligands. *J. Chem. Soc. Dalt. Trans.* **1999**, No. 10, 1519–1530.

(71) van Leeuwen, P. W. N. M.; Kamer, P. C. J.; Reek, J. N. H.; Dierkes, P. Ligand Bite Angle Effects in Metal-Catalyzed C−C Bond Formation. *Chem. Rev.* **2000**, *100* (8), 2741–2770.

(72) Falivene, L.; Credendino, R.; Poater, A.; Petta, A.; Serra, L.; Oliva, R.; Scarano, V.; Cavallo, L. SambVca 2. A Web Tool for Analyzing Catalytic Pockets with Topographic Steric Maps. *Organometallics* **2016**, *35* (13), 2286–2293.

(73) Piou, T.; Romanov-Michailidis, F.; Romanova-Michaelides, M.; Jackson, K. E.; Semakul, N.; Taggart, T. D.; Newell, B. S.; Rithner, C. D.; Paton, R. S.; Rovis, T. Correlating Reactivity and Selectivity to Cyclopentadienyl Ligand Properties in Rh(III)-Catalyzed C–H Activation Reactions: An Experimental and Computational Study. *J. Am. Chem. Soc.* **2017**, *139* (3), 1296–1310.

(74) Wu, K.; Doyle, A. G. Parameterization of Phosphine Ligands Demonstrates Enhancement of Nickel Catalysis via Remote Steric Effects. *Nat. Chem.* **2017**, *9* (8), 779–784.

(75) Harper, K. C.; Bess, E. N.; Sigman, M. S. Multidimensional Steric Parameters in the Analysis of Asymmetric Catalytic Reactions. *Nat. Chem.* **2012**, *4* (5), 366–374.

(76) Verloop, A. The Use of Linear Free Energy Parameters and Other Experimental Constants in Structure–Activity Studies. In *Drug Design*; Ariens, E. J., Ed.; Elsevier, 1972; pp 133–187.

(77) Santiago, C. B.; Milo, A.; Sigman, M. S. Developing a Modern Approach To Account for Steric Effects in Hammett-Type Correlations. *J. Am. Chem. Soc.* **2016**, *138* (40), 13424–13430.

(78) Piou, T.; Romanov-Michailidis, F.; Romanova-Michaelides, M.; Jackson, K. E.; Semakul, N.; Taggart, T. D.; Newell, B. S.; Rithner, C. D.; Paton, R. S.; Rovis, T. Correlating Reactivity and Selectivity to Cyclopentadienyl Ligand Properties in Rh(III)-Catalyzed C-H Activation Reactions: An Experimental and Computational Study. *J. Am. Chem. Soc.* **2017**, *139* (3), 1296–1310.

(79) Ota, Y.; Ito, S.; Kuroda, J.; Okumura, Y.; Nozaki, K. Quantification of the Steric Influence of Alkylphosphine–Sulfonate Ligands on Polymerization, Leading to High-Molecular-Weight Copolymers of Ethylene and Polar Monomers. *J. Am. Chem. Soc.* **2014**, *136* (34), 11898–11901.

(80) Huang, H.; Zong, H.; Bian, G.; Yue, H.; Song, L. Correlating the Effects of the N-Substituent Sizes of Chiral 1,2-Amino Phosphinamide Ligands on Enantioselectivities in Catalytic Asymmetric Henry Reaction Using Physical Steric Parameters. *J. Org. Chem.* **2014**, *79* (20), 9455–9464.

(81) Okuniewski, A.; Rosiak, D.; Chojnacki, J.; Becker, B. Coordination Polymers and Molecular Structures among Complexes of mercury(II) Halides with Selected 1-Benzoylthioureas. *Polyhedron* **2015**, *90*, 47–57.

(82) Jeletic, M. S.; Helm, M. L.; Hulley, E. B.; Mock, M. T.; Appel, A. M.; Linehan, J. C. A Cobalt Hydride Catalyst for the Hydrogenation of CO_2 : Pathways for Catalysis and Deactivation. *ACS Catal.* **2014**, *4* (10), 3755–3762.

(83) Jeletic, M. S.; Hulley, E. B.; Helm, M. L.; Mock, M. T.; Appel, A. M.; Wiedner, E. S.; Linehan, J. C. Understanding the Relationship Between Kinetics and Thermodynamics in CO_2 Hydrogenation Catalysis. *ACS Catal.* **2017**, *7* (9), 6008–6017.

(84) Becke, A. D. Density-functional Thermochemistry. III. The Role of Exact Exchange. *J. Chem. Phys.* **1993**, *98* (7), 5648–5652.

(85) Chai, J.-D.; Head-Gordon, M. Long-Range Corrected Hybrid Density Functionals with Damped Atom–atom Dispersion Corrections. *Phys. Chem. Chem. Phys.* **2008**, *10* (44), 6615.

(86) Liakos, D. G.; Neese, F. Is It Possible To Obtain Coupled Cluster Quality Energies at near Density Functional Theory Cost? Domain-Based Local Pair Natural Orbital Coupled Cluster vs Modern Density Functional Theory. *J. Chem. Theory Comput.* **2015**, *11* (9), 4054–4063.

(87) Wadt, W. R.; Hay, P. J. Ab Initio Effective Core Potentials for Molecular Calculations. Potentials for Main Group Elements Na to Bi. *J. Chem. Phys.* **1985**, *82* (1), 284–298.

(88) Hay, P. J.; Wadt, W. R. Ab Initio Effective Core Potentials for Molecular Calculations. Potentials for K to Au Including the Outermost Core Orbitals. *J. Chem. Phys.* **1985**, *82* (1), 299–310.

(89) Weigend, F.; Ahlrichs, R. Balanced Basis Sets of Split Valence, Triple Zeta Valence and Quadruple Zeta Valence Quality for H to Rn: Design and Assessment of Accuracy. *Phys. Chem. Chem. Phys.* **2005**, *7* (18), 3297.

(90) Marenich, A. V.; Cramer, C. J.; Truhlar, D. G. Universal Solvation Model Based on Solute Electron Density and on a Continuum Model of the Solvent Defined by the Bulk Dielectric Constant and Atomic Surface Tensions. *J. Phys. Chem. B* **2009**, *113* (18), 6378–6396.

(91) Mennucci, B.; Tomasi, J. Continuum Solvation Models: A New Approach to the Problem of Solute's Charge Distribution and Cavity Boundaries. *J. Chem. Phys.* **1997**, *106* (12), 5151–5158.

(92) Barone, V.; Cossi, M. Quantum Calculation of Molecular Energies and Energy Gradients in Solution by a Conductor Solvent Model. *J. Phys. Chem. A* **1998**, *102* (11), 1995–2001.

(93) Cancès, E.; Mennucci, B.; Tomasi, J. A New Integral Equation Formalism for the Polarizable Continuum Model: Theoretical Background and Applications to Isotropic and Anisotropic Dielectrics. *J. Chem. Phys.* **1997**, *107* (8), 3032–3041.

(94) Shao, Y.; Gan, Z.; Epifanovsky, E.; Gilbert, A. T. B.; Wormit, M.; Kussmann, J.; Lange, A. W.; Behn, A.; Deng, J.; Feng, X.; et al. Advances in Molecular Quantum Chemistry Contained in the Q-Chem 4 Program Package. *Mol. Phys.* **2015**, *113* (2), 184–215.

(95) Neese, F. The ORCA Program System. *Wiley Interdiscip. Rev. Comput. Mol. Sci.* **2012**, *2* (1), 73–78.

Chapter 4: Final Remarks

With ever increasing computational power, quickly and accurately assessing chemical properties through simulation is becoming easier. The ability to simulate all types of chemical reactions, and the larger scope of related chemical space is quickly becoming feasible. One crucial advancement comes in the form of semi-automated tools for assessing reaction landscapes. These tools enable chemical investigations to explore beyond narrow regions of chemical space providing an increasingly broad view of related reactivity. Given that development of computational tools continues, the combined information from the relevant portions of the potential energy surface and the quantitative structure-energy relationships provided via computational investigation will eventually rival the accuracy and reliability of experimental testing. The implications for exploring chemical space will shift the paradigm of computational investigation from experimental confirmation, to truly guiding which tests are necessary in the laboratory.

4.1 Research Summary

This work continues to explore the use of computational simulation to investigate complex chemical reactivity. In chapter two of this work, a tandem experimental-computational study of $C(sp^3)$-N reductive elimination from a palladium(IV) was performed. The study focused on the relevant reaction pathways for $C(sp^3)$-N reductive elimination, with computational methods providing important insight into alternative reductive eliminations including $C(sp^3)$-$C(sp^2)$ pathways. A complete description of important reaction pathways enabled computation to accurately predict rates and thermodynamics for a new class of palladium complexes.

Chapter 3 aimed to extend the applicability of scalable computational methods for searching large regions of organometallic chemical space. The thermodynamic landscape for cobalt catalyzed CO_2 reduction provided unique insight into energy structure correspondence. Statistical modeling packages were employed to simplify the analysis of many possible chemical descriptors. In the end, the large chemical space revealed the limitations of steric molecular

features and importance of orbital descriptions, as well as highlighting the need for additional intuitive metrics for quantifying electronic and steric contributions. The dataset also suggested that the catalytically relevant regions of the landscape are tightly bounded, heavily favoring electron neutral ligands. These data provided a potentially accessible experimental complex Co(dCype)H for further investigation.

The research outlined in this document is a contribution to a growing body of work which attempts to bridge the gap between experimental and computational chemistry. In contrast to experiment where all possible reaction pathways are naturally sampled, computational chemistry has long been beholden to technical limitations enabling investigation of only a few possible reaction pathways at a time. In many ways, the constrained investigations of computational chemistry were only possible because of the close relationship to experimental chemistry. With the advent of these new tools comes an opportunity for computational chemistry to start performing some of the more complicated aspects of chemical development including reaction screening, computational first reaction discovery, and potentially substrate development and selection. These new opportunities open a rich collaborative environment where the best aspects of experimental and computational chemistry can mesh for fast, accurate and more holistic reaction investigation.

4.2 Constructing Reasonable Models

These new opportunities must be met with caution, however. As computational programs are made more accessible the likelihood that models and datasets will be overinterpreted increases. In particular, chemists must be careful to ensure all approximations and model limitations are clearly understood throughout the investigation. Software such as ZStruct (reaction path finding tool), and the growing string method are designed to provide the user with fast, accessible and accurate data based on minimal structural input information. The ease with which these programs operate can misrepresent the underlying complexity of the chemical environment to which they are applied. Therefore, development of chemically meaningful structural models is even more crucial as these tools continue to advance.

With the advent of new, powerful, and accessible computational methods is likely a rise in the number of studies performed with only limited experimental data. While these types of studies are not intrinsically problematic, extra caution must be applied during the initial stages of model

development. A few common steps have emerged which seem to simplify the early stages of model development, particularly for organometallic systems. These can be roughly divided into: 1) level of theory and method selection 2) initial 'starting material' and 3) model refinement with experimental feedback. The next paragraphs detail, in broad strokes, how to best resolve each of these challenges.

The selection of the appropriate level of theory will likely remain challenging until a highly accurate "silver bullet" method emerges. For now, understanding or testing the limitations and strengths of various DFT implementations provides the best defense against failure. Reviews discussing the differences in basis set,[1] functional,[2–4] and solvation methods[5] remain crucial to selection of the appropriate level of theory to optimize structures[6,7] as well as calculate single points. However, the best solution to DFT method selection seems to be benchmarking against experimental datasets when available. Benchmarking ensures that the key chemical information is captured by the chosen model and that the data is physically meaningful. Using benchmarks, chemical intuition and past literature are vital to the selection of a suitable DFT level of theory.

Computational modeling of reaction pathways requires that investigations aim to identify the lowest energy structures on the potential energy surface. Without these minima, accurate representation of the kinetics and thermodynamics of a given reaction is dubious. For reactions involving a single starting material with limited conformations, such as in simple organic reactions, identification of reference structures is often straight forward. In comparison identification of the best entry into a catalytic organometallic reaction is sometimes less clear. This challenge is complicated by potential substrate-solvent, catalyst-solvent, and conformational mobility of the substrate bound or near the catalyst. The potential pitfalls for not correctly addressing model development at this stage are sometimes mitigated by error cancelation, i.e. if a solvent is bound at the starting material, transition state and product, then omitting the solvent will have a moderated impact on the accuracy. Relying on error cancellation is of course inadvisable. However, directly addressing this problem is rather straight forward. Often the experimentally observable starting material is a sufficient guess structure. Subsequent conformational searches can then be performed to ensure that the most stable geometry is obtained. Furthermore, addition of one or more solvent molecules to open coordination sites of the catalysts can be attempted. Generally, if the reaction is performed in coordinating solvent such as acetonitrile, pyridine, DMSO, water, etc. the user should attempt to bind solvent to the catalyst to see if the energy of the complex is stabilized. If

coordination sites open throughout the reaction path, an appropriate course of action would be to attempt solvent addition for those intermediate structures. Finally, some metal structures have multiple accessible spin states with unique geometries. This is sometimes the case with nickel, cobalt, iron and other first row transition metals. For these types of complexes, all reasonable spin states should be sampled prior to beginning the reaction path sampling.

Finally, the ability to refine the computational structures and mechanisms through experimental feedback is crucial to the development of highly accurate and predictive models. The Zimmerman lab has largely viewed experimental collaboration as a prerequisite for applying reaction path sampling. For instance, in the case of investigating palladium (IV) reductive elimination processes, we obtained a large dataset which included multiple pathways to $C(sp^3)$-$C(sp^2)$ and $C(sp^3)$-F reductive elimination (detailed in appendix A). From the initial ZStruct investigation, there was little discernable difference in the accuracy of the results $C(sp^3)$-N reductive elimination and $C(sp^3)$-$C(sp^2)$ and $C(sp^3)$-F reductive elimination process. Only later, after closely analyzing the differences in expected energies as compared to experiment were we able to better capture the solvation and ligand environment at the palladium (IV) center. Specifically, the incorporation of explicit acetonitrile on the palladium was a crucial addition to the model that was added after the initial reaction discovery process *and primarily due to experimental feedback*. Without the data from experiment the narrow window of energy analyzed in this study is likely infeasible. This example highlights the importance of maintaining a close working relationship between computational and experimental chemistry even as the tools in computational chemistry seem to provide broader and more data rich assessments of the reaction landscape.

While sometimes computational reaction path investigations or QSAR studies must be performed in the absence of real time experimental feedback, preference should be given to chemistry which is actively being studied. In general, computational studies rely upon error cancellation as a common explanation for the high degree of accuracy for DFT studies. While fortuitous error cancellation is likely a contributing factor, much of the ability to systematically develop predictive models relies upon human guidance and close collaboration with experimental chemistry. Each step of the process: selection of the best level of theory, incorporation of additional details to the model, and finally the interpretation of the results, must consider the information obtained from experimental observation as well as the assumptions of the model.

Despite the error associated with DFT in general, user guided model development can significantly minimize error associated with making computational predictions. Operating in a data rich environment has the potential mask the underlying flaws in the initial model. Chemists should be wary of mistaking correlation with causation when analyzing large sets of data, especially those associated with QSAR studies.[8] Scrutiny of each step of the model development, using experimental data, and rigorous intuition checks when possible will often guard against overinterpretation of data rich models. In summary, the prevalence of faster, more accurate, and broader reaching computational assessment is highly encouraging. However, this progress does not eschew but rather deepens the need for collaboration between experimental and computational chemistry.

4.3 Final Thoughts

Reaction landscape investigation through use of automated reaction path finding tools offers new insight into regions of chemical space that have yet to be observed or studied. This dissertation has demonstrated the utility of automated reaction path finding and comprehensive computational investigations of reaction landscapes. Significant work remains toward the development of more user-friendly and intuitive software as well as increased autonomy of reaction path tools. Future work for potential energy surface investigation should target broader integration with experiment as well as using statistics to validate the utility of specific steric and electronic descriptions. Such advances will pave the way for improving our ability to think about and describe the relevant portions of a molecule and how they relate to experimentally observed chemical reactivity.

4.4 References

(1) Papajak, E.; Zheng, J.; Xu, X.; Leverentz, H. R.; Truhlar, D. G. Perspectives on Basis Sets Beautiful: Seasonal Plantings of Diffuse Basis Functions. *J. Chem. Theory Comput.* **2011**, *7* (10), 3027–3034.

(2) Burke, K. Perspective on Density Functional Theory. *J. Chem. Phys.* **2012**, *136* (15), 150901.

(3) Becke, A. D. Perspective: Fifty Years of Density-Functional Theory in Chemical Physics. *J. Chem. Phys.* **2014**, *140* (18), 18A301.

(4) Cohen, A. J.; Mori-Sánchez, P.; Yang, W. Challenges for Density Functional Theory. *Chem. Rev.* **2012**, *112* (1), 289–320.

(5) Matsui, T.; Shigeta, Y.; Morihashi, K. Assessment of Methodology and Chemical Group Dependences in the Calculation of the P K a for Several Chemical Groups. *J. Chem. Theory Comput.* **2017**, acs.jctc.7b00587.

(6) Schlegel, H. B. Geometry Optimization. *Wiley Interdiscip. Rev. Comput. Mol. Sci.* **2011**, *1* (5), 790–809.

(7) Schlegel, H. B. Exploring Potential Energy Surfaces for Chemical Reactions: An Overview of Some Practical Methods. *J. Comput. Chem.* **2003**, *24* (12), 1514–1527.

(8) Polishchuk, P. Interpretation of Quantitative Structure–Activity Relationship Models: Past, Present, and Future. *J. Chem. Inf. Model.* **2017**, *57* (11), 2618–2639.

Appendix A: Supporting Data for Chapter 2

A. 1. Computational Reaction Discovery

A.1.1 General Computational Information

1_{Ms} was chosen for the complete ZStruct reaction path search to significantly reduce the total computational cost. Furthermore, experiment had demonstrated the feasibility of this sulfonamide for C(sp^3) -N bond formation. Once the lowest energy starting conformations for **1_{Ms}-a** and **1_{Ms}-b** palladium complexes were found, these starting points were used for finding the reaction paths disclosed herein. Additionally, excess sulfonamide and bipyridine were not included in the ZStruct analysis as the reaction is zero order in both[1]. Starting from **1_{Ms}-a** and **1_{Ms}-b,** the generated pathways were filtered after each iteration to remove high energy and unreasonable possibilities. **Figure A.1** illustrates the stepwise application of increasing levels of theory to improve upon the computational results.

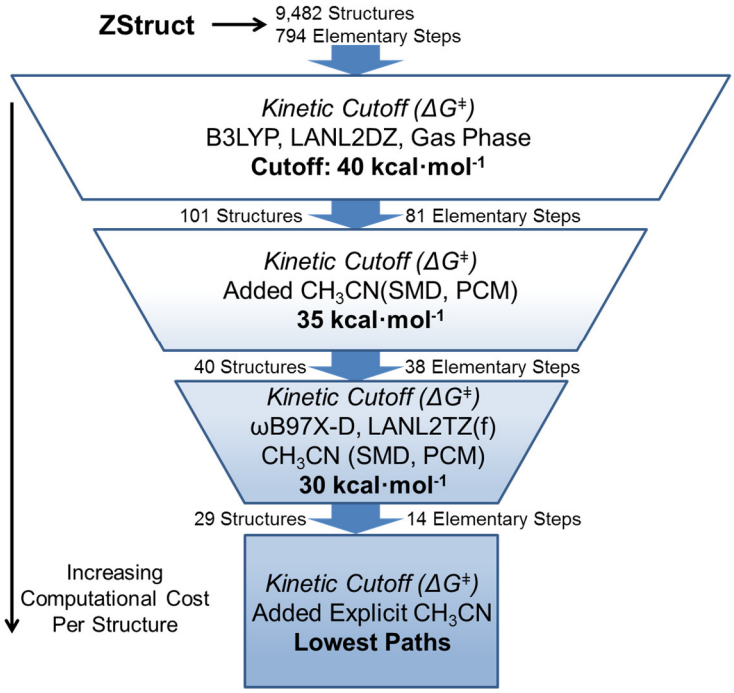

Figure A.1 Detailed outline of computational filtration tiers. Each box contains a summary of the level of theory and the energy cutoff used. Structures passing the threshold proceed to the next level filter.

An updated version of the ZStruct program[1] implemented in C++ generated a total of 9,482 structures and 794 elementary reaction steps. During the initial assessment of reaction paths the B3LYP density functional[2] in a spin restricted formalism with the LANL2DZ[3] basis set was employed. The latest version of the Growing String Method[2,3,4] (GSM) performed the double-ended reaction path searches connecting the initial structures to the ZStruct-generated intermediates. GSM provides a minimum energy path and exact transition state search in a single computation, enabling rapid characterization of the many hypothetical reaction pathways. GSM and ZStruct use Q-Chem 4.0[4] to provide quantum mechanical energies and gradients. All structures generated in this initial search were submitted to the first tier energy filter of 40 kcal·mol^{-1}. After removing high energy intermediates, a total of 101 structures, connected by 81 elementary steps, remained.

High energy pathways conjectured from chemical intuition were also included for completeness (for instance Pathway III, concerted C(sp^3)-N coupling from **1$_{Ms}$-b**, page S25). Other pathways were generated by ZStruct and found to be unfavorable, but could be used as a

reference in related chemical systems; these pathways are included below. The pathways eliminated in the initial cutoff, set at 40 kcal·mol^{-1} were deemed energetically inaccessible based on the magnitude of solvent stabilization provided by **Table A.1**

Structure	Gas Phase Energy B3LYP LANL2DZ	Solvated Energy *B3LYP LANL2DZ Solvation: SMD PCM	Solvated Energy **ωb97x-D LANL2TZ Solvation: SMD PCM	Explicit Solvation **ωb97x-D LANL2TZ Solvation: SMD PCM (1 molecule CH_3CN)
1_{Ms}-a	0	0	0	0
$TS7_{Ms}$	32.3	29.6	25.7	22.8
4_{Ms}	21.6	23.1	24.5	13.1
1_{Ms}-b	1.2	2.8	1.9	1

*Performed in Q-Chem (see above for more information)
**Performed using GAMESS

Table A.1 Comparison of energetics for key intermediates at various levels of theory.

The sulfonamide-Pd^{IV} complex ion pair $\mathbf{4_{Ms}}$ is expected to be the most significantly stabilized by solvent as this species bears the largest charge separation. With this in mind, we selected an energy cutoff that was higher than the largest stabilization due to solvent. As shown in the table, less than 10 kcal·mol^{-1} was the largest observed stabilization for $\mathbf{TS7_{Ms}}$ and $\mathbf{4_{Ms}}$. Since the largest barrier for C(sp^3)-N reductive elimination was experimentally observed to be 25.7 kcal·mol^{-1} prior to the application of ZStruct, we were able to set the first energy cutoff significantly higher, at 40 kcal·mol^{-1}. The energetic margin allotted for the initial gas phase calculations is conservative, incorporating more pathways than were most likely needed. This is demonstrated by the number of high energy, unproductive pathways shown in the following sections of this supporting information. Before application of the second tier screening, the optimized intermediates and transition states were then evaluated in the GAMESS[5] software package to calculate energies in solvent. These calculations used the B3LYP density functional with the LANL2DZ basis set. Solvent was calculated using an implicit PCM[6] solvent model, SMD[7]. After application of this energy filter a total of 40 structures and 38 elementary steps remained. We then compared the initial isomerization results to experiment and found that ionic

structures (specifically the dissociated sulfonamide) were not well-represented by B3LYP energies.

The ωB97X-D[8] density functional was chosen for the next level of screening due to its dispersion correction and inclusion of range-separated exchange, neither which are present in B3LYP. The triple zeta, polarized with diffuse functions 6-311++G**[9] basis set was used for hydrogen through sulfur and LANL2TZ(f) with f orbitals[6c,10] was used for Pd. Solvent was calculated using PCM with SMD. Entropic and enthalpic frequency calculations were performed using Q-Chem 4.0 for a temperature of 65 °C. After these single points were analyzed we were left with 29 structures and 14 elementary steps which comprised our primary pathways.

Performing geometry optimizations at the ωB97X-D level of theory with the larger basis was considerably more time consuming and resulted in minor changes to geometries. **Figure S32** overlays the geometries from B3LYP to those of ωB97X-D. The root mean square error (RMSE) between **1_{Ms}-a** in B3LYP/LANL2DZ and ωB97X-D/LANL2TZ(f)/PCM-SMD for bond length is 0.0017Å, the RMSE for angles 1.68°. The root mean square error (RMSE) between **1_{Ms}-a** in B3LYP/LANL2DZ and ωB97X-D/LANL2TZ(f)/PCM-SMD for bond length is 0.0018Å, the RMSE for angles 2.44°. The energy for **1_{Ms}-a** at the ωB97X-D/LANL2TZ(f)/PCM-SMD was calculated to be -1754.113019 Hartree and **1_{Ms}-b** -1754.109731 Hartree corresponding to 0.0 kcal·mol^{-1} for **1_{Ms}-a** and 2.1 kcal·mol^{-1} for **1_{Ms}-b.**

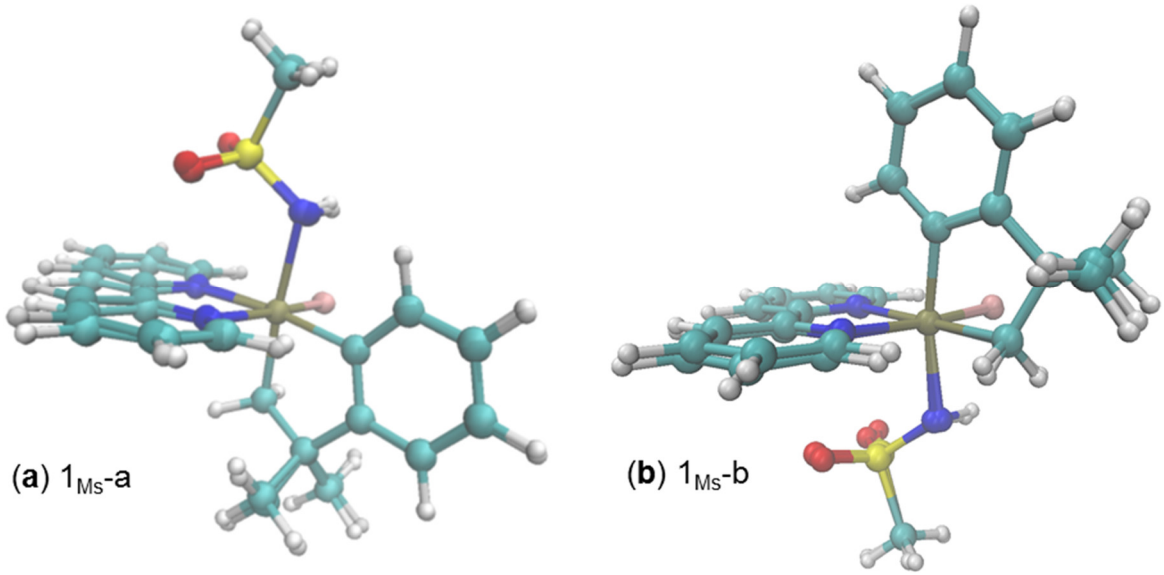

Figure A.2 Overlays of B3LYP/LANL2DZ and ωB97X-D/LANL2TZ(f)/PCM-SMD geometry optimizations for (a) 1_{Ms}-a and (b) 1_{Ms}-b

Finally, one molecule of explicit acetonitrile was used to provide specific solvation interactions and a more accurate energetic assessment. Multiple conformations for each of the solvated structures were sampled to ensure a low energy structure was found. If the explicit solvent did not reduce the energy of a particular elementary step, the value without explicit solvent is reported instead.

Figure A.3 considers the reductive elimination from **1_{Ms}-a** and compares the use of explicit solvent to stabilize all elementary steps, no explicit acetonitrile, and the lowest possible free energy pathway comprised of acetonitirile as a reagent where needed. Noteably, we observed a different transition state for reductive elimination when explicit acetonitrile was considered. The geometries of the transition states in these cases reflect the dissociation of the acetonitrile with concomitant C(sp^3)-N reductive elimination (**$TS11_{Ms}$_withCH_3CN**).

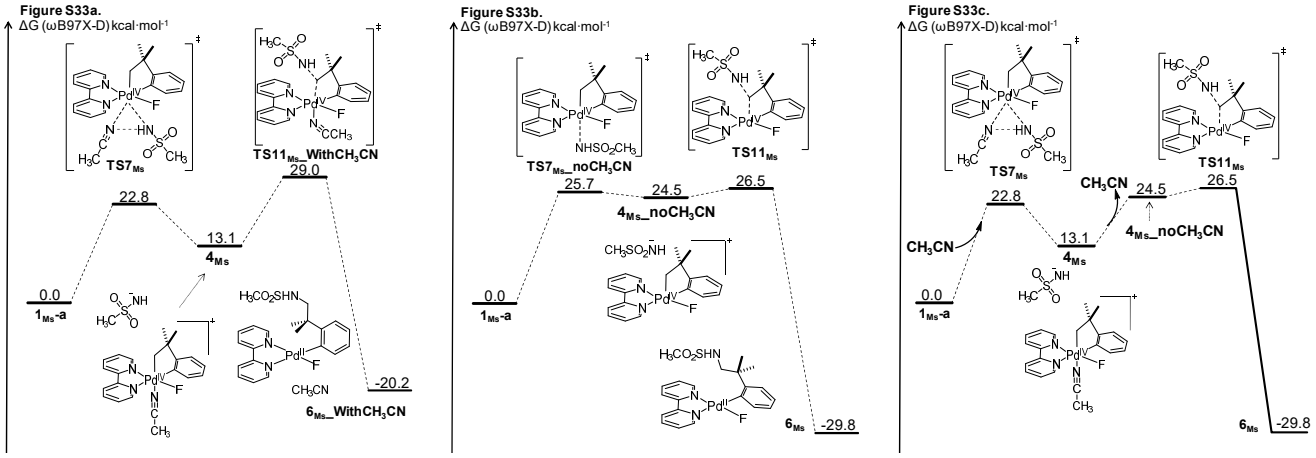

Figure A.3 C(sp^3)-N reductive elimination from 1_{Ms}-a with explicit solvent (a) forced in every step (b) not present in any step and (c) used only where necessary in the calculations.

Discussion and comparison of general C(sp^3)-N reductive elimination mechanisms

The following sections detail the most accessible and favorable mechanisms found through the ZStruct search of **1_{Ms}**. The pathways discussed in the main text correspond to the most likely pathways, but more complete details of the potential reaction mechanisms are provided here.

All computed values shown in **Table A.2** are without explicit acetonitrile. Since no significant bonding interaction with acetonitrile was found in the transition state for the reductive

elimination, inclusion of explicit acetonitrile was associated with an increase in the relative energy of the transition state.

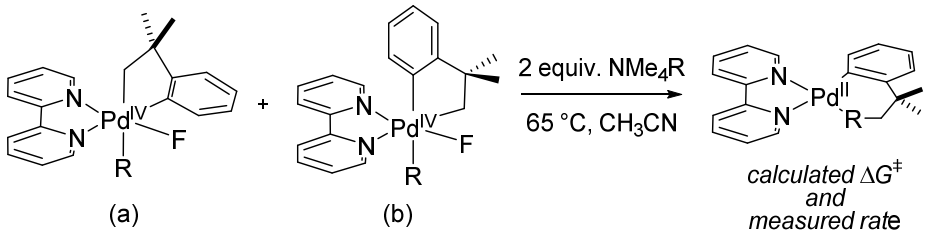

Entry	Structure Number	R	*Comp. Path. IV* $\Delta G^{\ddagger}$	*Comp. Path. V* $\Delta G^{\ddagger}$	Exp. Measured $\Delta G^{\ddagger}$
1	$\mathbf{1_{Ms}}$	CH_3SO_2NH	26.5	26.7	25.7
2	$\mathbf{1_{Ts}}$	*p*-Tol-SO_2NH	26.1	28.5	25.7
3	$\mathbf{1_{CF2H}}$	CF_2HSO_2NH	24.7	25.1	25.1
4	$\mathbf{1_{Tf}}$	CF_3SO_2NH	25.3	24.4	24.8
5	$\mathbf{1_{TsNMe}}$	*p*-Tol-$SO_2N(Me)$	27.8	25.2	25.0
6	$\mathbf{1_{BisTf}}$	$(CF_3SO_2)_2N$	23.7	26.9	N/A

Table A.2 C-N Reductive Elimination Summary

Accurate prediction of $\Delta G^{\ddagger}$ was only possible through consideration of both pathways for reductive elimination. The main text provides an assessment of geometric features comparing pathway IV to pathway V for only $\mathbf{1_{Ms}}$. **Figure S34** and **Table S37** take this comparison further, showing the relevant geometric data for all analyzed sulfonamides. Importantly, these test cases also highlighted key distinctions between the two transition states. For instance, $\mathbf{TS11_{Ms}}$ N-Pd-C average bond angle for ***B*** was 176.9°, while average bond angle for ***B'*** was 152.5°.

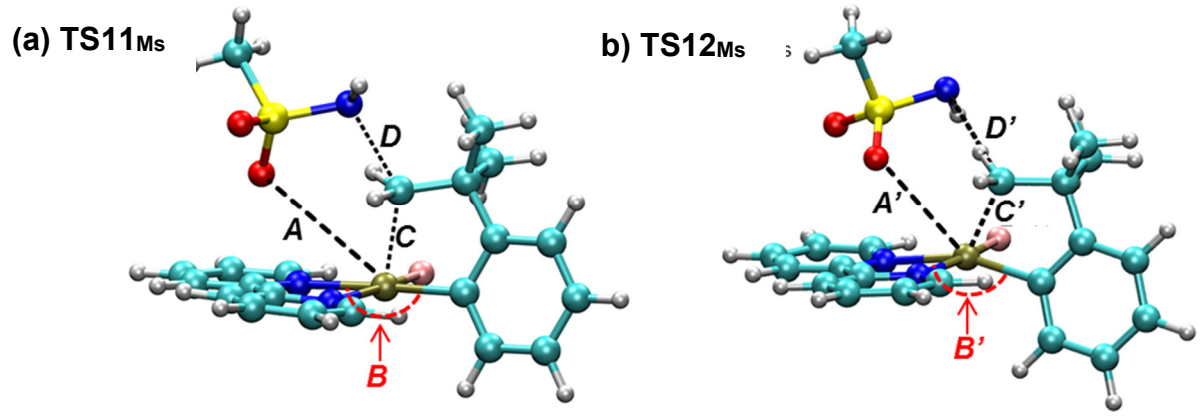

Figure A.4. (a) C(sp^3)–N reductive elimination transition state **TS11$_{Ms}$** from **1$_{Ms}$-a** (in Pathway IV), reference for labels shown in **Table S37**. **(b)** Pd^{IV} reductive elimination transition state **TS12$_{Ms}$** resulting from **1$_{Ms}$-b** (in Pathway V), reference for labels shown in **Table S37**.

R	**A** Pd-O length	**A'** Pd-O length	**B** N-Pd-C angle	**B'** N-Pd-C angle	**C** Pd-C length	**C'** Pd-C length	**D** C-N length	**D'** C-N length
CF_3SO_2 (Tf)	4.85 Å	3.22 Å	176.7°	156.6°	2.23 Å	2.15 Å	2.61 Å	3.21 Å
CF_2HSO_2	3.74 Å	3.22 Å	176.2°	154.7°	2.32 Å	2.16 Å	2.50 Å	3.10 Å
p-Tol-SO_2NH (Ts)	3.17 Å	3.00 Å	176.8°	148.1°	2.23 Å	2.14 Å	2.90 Å	3.18 Å
CH_3SO_2 (Ms)	3.85 Å	3.27 Å	176.9°	148.1°	2.32 Å	2.17 Å	2.49 Å	3.17 Å
p-Tol-SO_2NCH_3 (TsMe)	3.19 Å	3.29 Å	177.0°	150.7°	2.26 Å	2.16 Å	2.72 Å	3.08 Å

Table A.3. Geometry comparison for TS11$_{Ms}$ and TS12$_{Ms}$ for various sulfonamides

Rationalization of Pathway IV and Pathway V

Examination of the two reaction pathways indicated that pathway IV correlated well with pK_a (R^2 = 0.775) while pathway V did not (R^2 = 0.280) (**Figure A.5**).

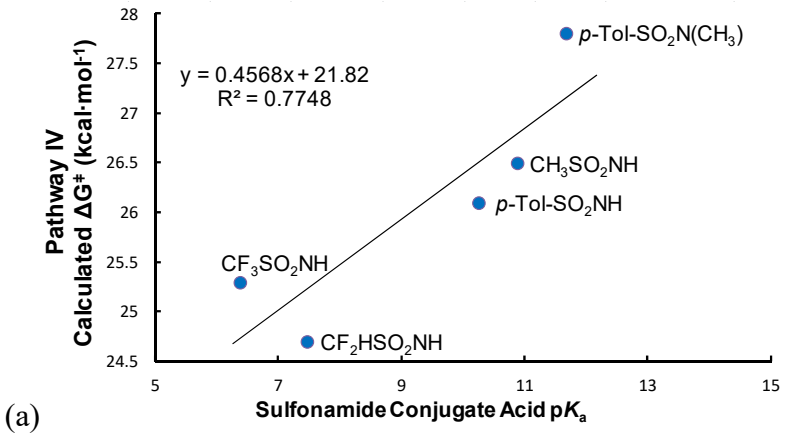

(a)

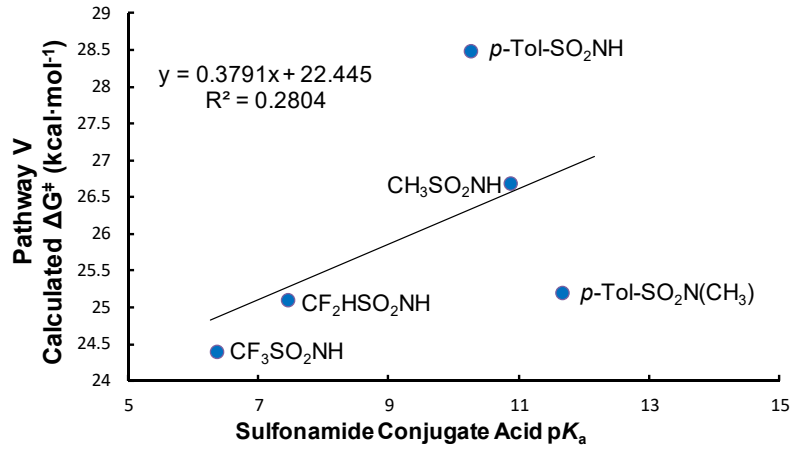

(b)

Figure A.5. (a) Calculated $\Delta G^{\ddagger}$ for pathway IV versus sulfonamide conjugate acid pK_a (b) Calculated $\Delta G^{\ddagger}$ for pathway V versus sulfonamide conjugate acid pK_a

While the lowest $\Delta G^{\ddagger}$ for C(sp^3)-N correlates with pK_a for the $MsNH^-$, $TsNH^-$, $TfNH^-$, and $CF_2HSO_2NH^-$ sulfonamides the $TsNMe^-$ sulfonamide was a clear outlier. The $TsNMe^-$ has the highest pK_a of 11.67, but one of the lowest C(sp^3)-N reductive elimination barriers ($\Delta G^{\ddagger}$ of 25.2 kcal·mol^{-1}). Taken together these data demonstrate that the predicted lowest energy pathway (either pathway IV or V) was found to vary as a function of sulfonamide structure. In terms of the specific reactivity, $TsNH^-$, and $CF_2HSO_2NH^-$ favored pathway IV, $MsNH^-$ and $TfNH^-$ favor neither pathway IV or V and were comparable in energy, and $TsNMe^-$ clearly

favored pathway V over pathway IV, 25.2 kcal·mol^{-1} versus 27.8 kcal·mol^{-1} respectively. In an effort to better understand and possibly rationalize the reactivity differences between TsNMe$^-$ and TsNH$^-$ sulfonamides we compared the TsNH$^-$ and TsNMe$^-$ oxygen bound intermediate (**5**$_{Ts}$ and **5**$_{TsMe}$), pathway V transition states (**TS12**$_{Ts}$ and **TS12**$_{TsMe}$), as well as the final product energies and conformations (**6**$_{Ts}$ and **6**$_{TsMe}$) as shown in **Figure A.6**.

Even though TsNMe$^-$ and TsNH$^-$ are similar in structure the two sulfonamides each favor a different pathway; TsNH$^-$ favors pathway IV and TsNMe$^-$ favors pathway V. We observed that the H-F interaction present in intermediate 5$_{Ts}$ (H-F length = 2.10 Å) breaks throughout transition state **TS12**$_{Ts}$ (H-F length = 3.05 Å) and is completely broken in the product **6**$_{Ts}$ (H-F length = 4.80 Å). Breaking the H-F bond during transition state **TS12**$_{Ts}$ was expected to result in an overall increase in energy of reductive elimination through pathway V (observed $\Delta G^{\ddagger}$ for TS12$_{Ts}$ = 28.5 kcal·mol^{-1}). In comparison, this H-F interaction is not possible for the TsNMe$^-$ complex; thereby, the lower observed barrier for pathway V (observed $\Delta G^{\ddagger}$ for TS12$_{Ts}$ = 25.2 kcal·mol^{-1}) reductive elimination from TsNMe$^-$ supports this explanation. Reactivity differences in these two substrates can be further rationalized through consideration of the entire of the reaction profile. The stabilizing H-F interaction in **1**$_{Ts}$ results in a notably less exergonic reaction than the N-methyl analog; a direct comparison shows that the product energy for **6**$_{Ts}$ (ΔG = -22.8 kcal·mol^{-1}) is notably higher than **6**$_{TsMe}$ (ΔG = -27.9 kcal·mol^{-1}). By the Evans-Polanyi relationship a reduced thermodynamic driving force for TsNH$^-$ is expected (and was observed) to increase the barrier for C(sp^3)-N reductive elimination. Based on these observations we concluded that the lack of H-bonding in the TsNMe$^-$ results in a comparatively lower barrier for C(sp^3)-N reductive elimination for the **1**$_{TsMe}$ complex.

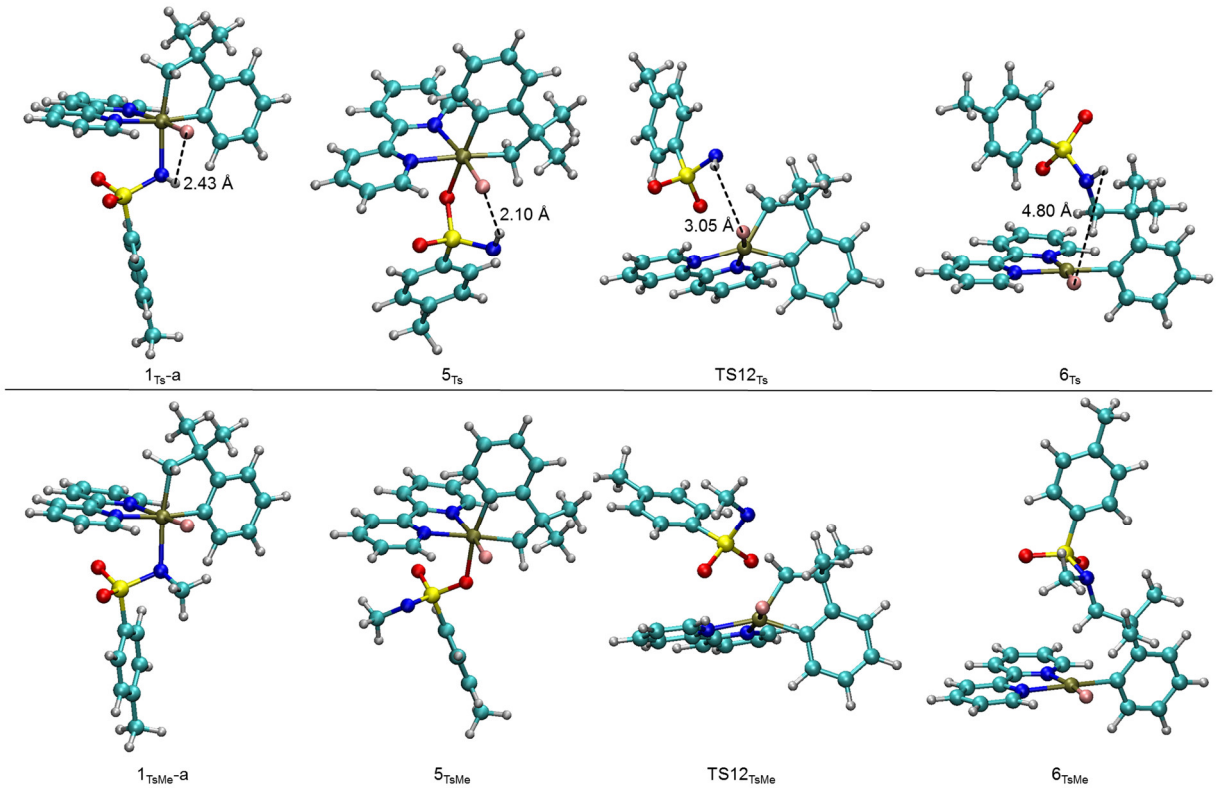

Figure A.6. Comparison of distances between sulfonamide N-R group and fluorine for $TsNMe^-$ and $TsNH^-$ substrates.

In summary, consideration of the entirety of the reaction profile, isomerization, reductive elimination and product energy, for all of the substrates involved in this study enabled the identification of key reaction features leading to a more detailed understanding of the reactivity involved with these select palladium(IV) complexes.

Summary Reductive Elimination Figures

Summary of $\mathbf{1_{Ms}}$ pathways

All summary figures highlight the lowest energy intermediate and transition state for the processes shown. Energies are referenced to **$\mathbf{1_{Ms}}$-a_withCH_3CN** whenever explicit acetonitrile is present, or to **$\mathbf{1_{Ms}}$-a** when acetonitrile is not present (similar naming and energetic references are used for all sulfonamides). For these reactions ($C(sp^3)$-N reductive elimination processes) transition states in the presence of explicit acetonitrile were identified to be significantly higher in energy as a result of having no specifically stabilizing chemical interactions along the reaction path. In cases where direct interaction between solvent and complex is necessary, using implicit and explicit solvent models together is known to increase the accuracy of the computation[11]. For instance dissociation sulfonamide at the palladium center is significantly stabilized by an explicit solvent molecule that fills the open Pd coordinate site **$\mathbf{7_{Ms}}$**. For the following figures, if CH_3CN is in the structure, than the lowest energy structure contains the CH_3CN-Pd^{IV} interaction shown. In all other cases the palladium complex is shown alone. The reference XYZ structures can be found listed by the structure name shown below. For the alternative variation, search for the structure number followed by _noCH_3CN or _withCH_3CN.

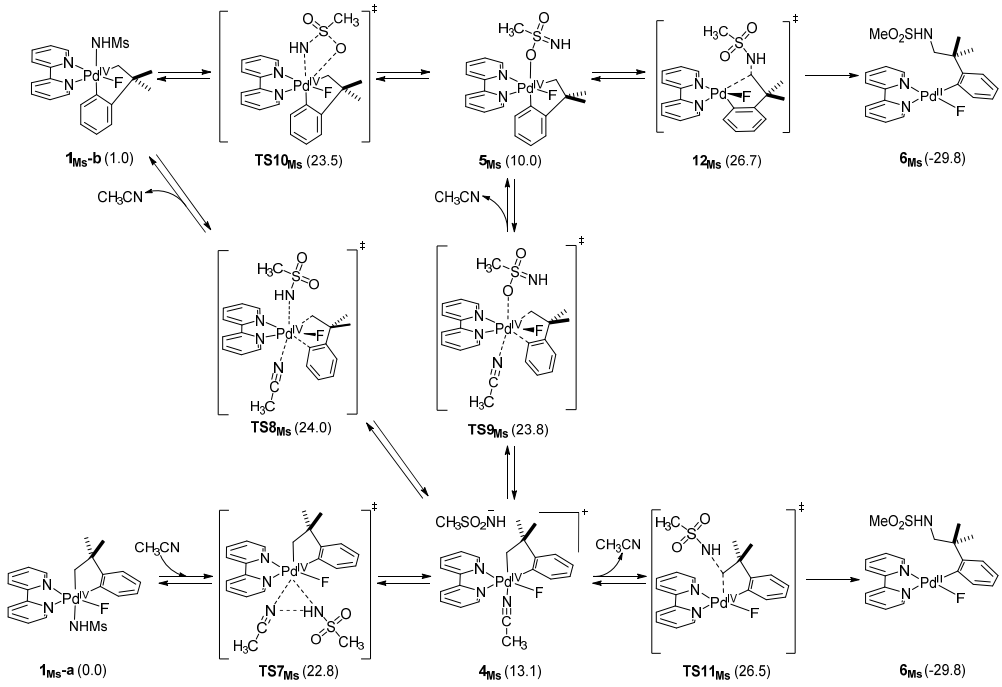

Figure A.7. Summary of $\mathbf{1_{Ms}}$ pathways

Summary of $\mathbf{1_{Tf}}$ pathways

All summary figures highlight the lowest energy intermediate and transition state for the processes shown at the same level of theory. Energies relative to **$\mathbf{1_{Tf}}$-a_withCH_3CN** where explicit acetonitrile is shown. Relative to **$\mathbf{1_{Tf}}$-a** where acetonitrile is not shown. For the following figures, if CH_3CN is in the structure, than the lowest energy structure contains the CH_3CN-Pd^{IV} interaction shown. In all other cases the palladium complex is shown without explicit solvent. The reference XYZ structures can be found listed by the structure name shown below. For the alternative variation, the structure number is followed by _noCH_3CN or -_withCH_3CN.

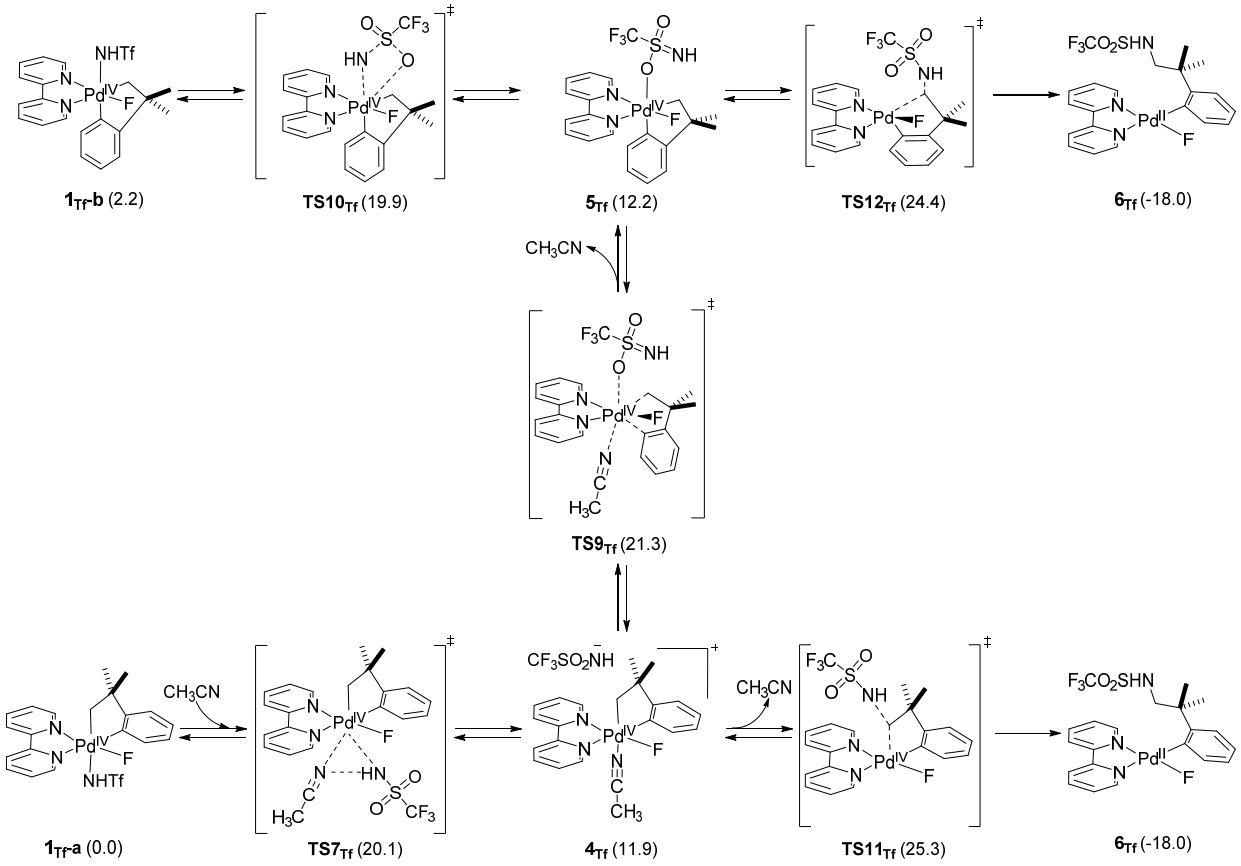

Figure A.8. Summary of $\mathbf{1_{Tf}}$ pathways

Summary of $\mathbf{1_{Ts}}$ pathways

All summary figures highlight the lowest energy intermediate and transition state for the processes shown at the same level of theory. Energies relative to **$\mathbf{1_{Ts}}$-a_withCH_3CN** where explicit acetonitrile is shown. Relative to **$\mathbf{1_{Ts}}$-a** where acetonitrile is not shown. For the following figures, if CH_3CN is in the structure, than the lowest energy structure contains the CH_3CN-Pd^{IV} interaction shown. In all other cases the palladium complex is shown without explicit solvent. The reference XYZ structures can be found listed by the structure name shown below. For the alternative variation, the structure number is followed by _noCH_3CN or -_withCH_3CN.

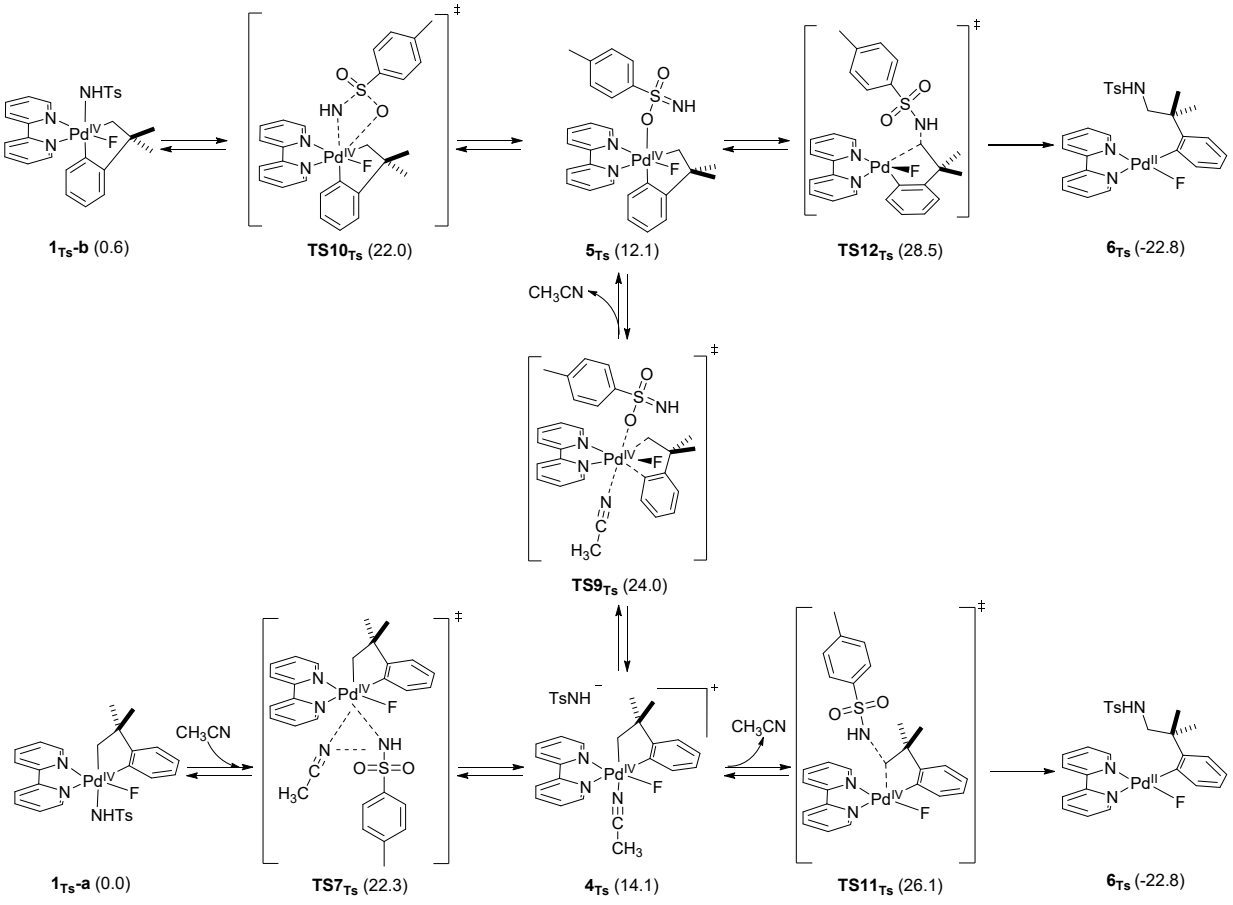

Figure A.9. Summary of $\mathbf{1_{Ts}}$ pathways

Summary of $\mathbf{1}_{\mathbf{TsNMe}}$ pathways

All summary figures highlight the lowest energy intermediate and transition state for the processes shown at the same level of theory. Energies relative to **$\mathbf{1}_{\mathbf{TsNMe}}$-a_withCH$_3$CN** where explicit acetonitrile is shown. Relative to **$\mathbf{1}_{\mathbf{TsNMe}}$-a** where acetonitrile is not shown. For the following figures, if CH_3CN is in the structure, than the lowest energy structure contains the CH_3CN-Pd^{IV} interaction shown. In all other cases the palladium complex is shown without explicit solvent. The reference XYZ structures can be found listed by the structure name shown below. For the alternative variation, the structure number is followed by noCH_3CN or -_withCH_3CN.

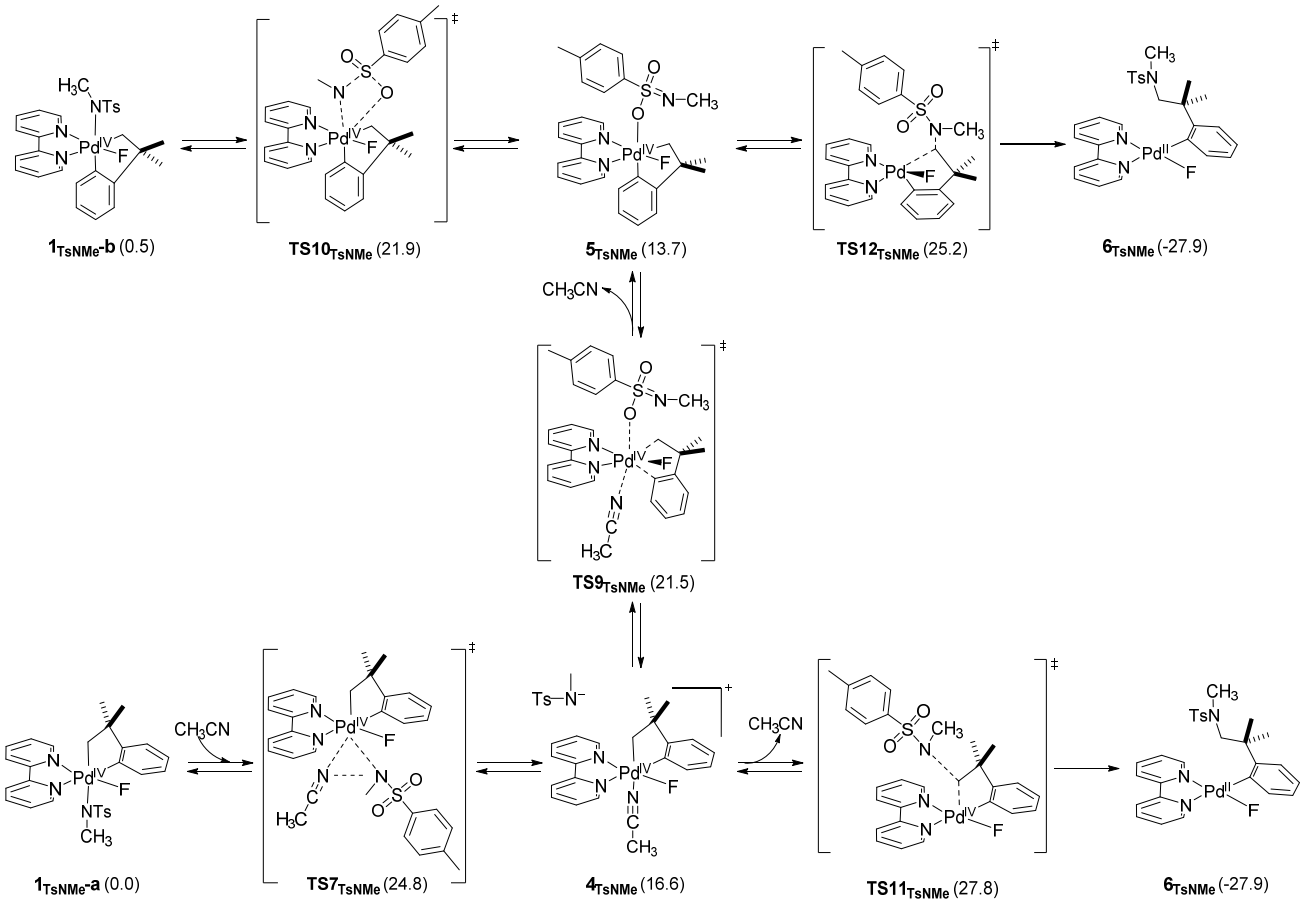

Figure A.10. Summary of $\mathbf{1}_{\mathbf{TsNMe}}$ pathways

Summary of $\mathbf{1_{CF2H}}$ pathways

All summary figures highlight the lowest energy intermediate and transition state for the processes shown at the same level of theory. Energies relative to **$\mathbf{1_{CF2H}$-a_withCH$_3$CN**} where explicit acetonitrile is shown. Relative to **$\mathbf{1_{CF2H}$-a**} where acetonitrile is not shown. For the following figures, if CH_3CN is in the structure, than the lowest energy structure contains the CH_3CN-Pd^{IV} interaction shown. In all other cases the palladium complex is shown without explicit solvent. The reference XYZ structures can be found listed by the structure name shown below. For the alternative variation, the structure number is followed by noCH_3CN or -_withCH_3CN.

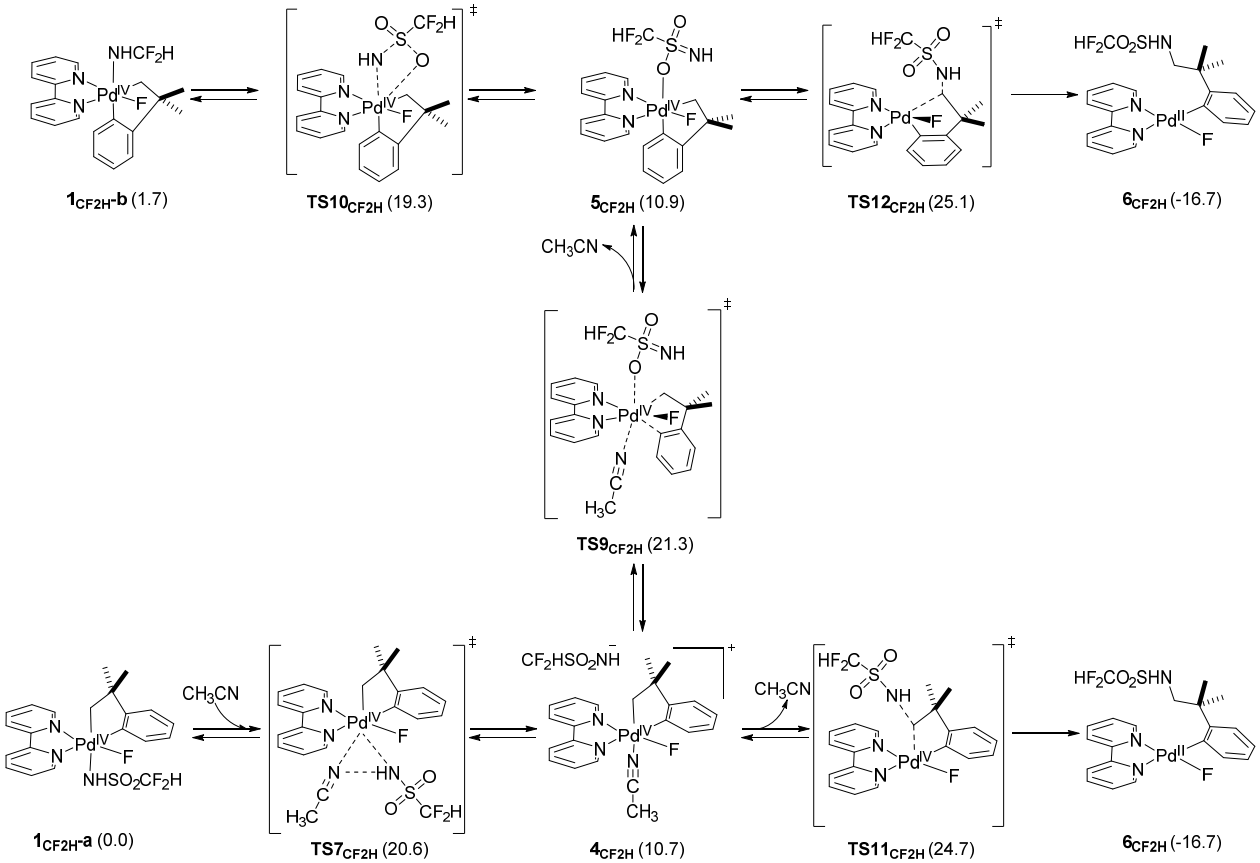

Figure A.11. Summary of $\mathbf{1_{CF2H}}$ pathways

Summary of C(sp^3)-N reductive elimination $\mathbf{1_{BisTf}}$ pathways

All summary figures highlight the lowest energy intermediate and transition state for the processes shown at the same level of theory. Energies relative to **$\mathbf{1_{BisTf}$-a_withCH$_3$CN**} where explicit acetonitrile is shown. Relative to **$\mathbf{1_{BisTf}$-a**} where acetonitrile is not shown. For the following figures, if CH_3CN is in the structure, than the lowest energy structure contains the CH_3CN-Pd^{IV} interaction shown. In all other cases the palladium complex is shown without explicit solvent. The reference XYZ structures can be found listed by the structure name shown below. For the alternative variation, the structure number is followed by _noCH_3CN or -_withCH_3CN.

Transition states for the acetonitrile **$TS7_{BisTf}$** and sulfonamide bound palladium complexes **$\mathbf{1_{BisTf}$-a**} were identified to be isoenergetic. Though the lowest C- N pathway and the C-C reductive elimination are close in energy, we rationalized the exclusive formation of C-C product based on the stable formation of **$\mathbf{14_{BisTf}$ (18)**.

(a) C-N reductive elimination from the acetonitrile bound **$\mathbf{7_{BisTF}}$**

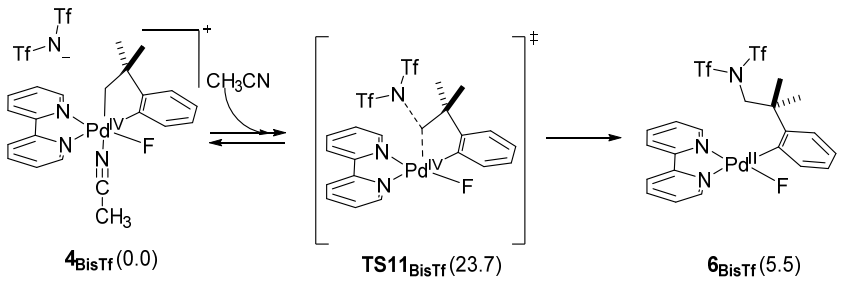

$\mathbf{4_{BisTf}}$(0.0) $\mathbf{TS11_{BisTf}}$(23.7) $\mathbf{6_{BisTf}}$(5.5)

(b) C-N reductive elimination from **$\mathbf{10_{BisTf}}$**

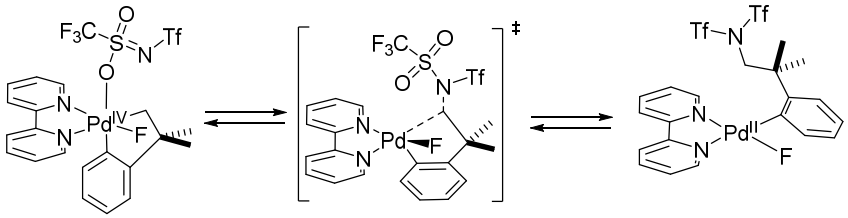

$\mathbf{5_{BisTf}}$(-0.2) $\mathbf{TS12_{BisTf}}$(26.9) $\mathbf{6_{BisTf}}$(5.5)

Figure A.12. Summary of C(sp^3)-N reductive elimination $\mathbf{1_{BisTf}}$ pathways

Summary of C(sp^3)–C(sp^2) reductive elimination from penta-coordinate palladium complex.

This instance of C–C reductive elimination is unique to the $\mathbf{1_{BisTf}}$ sulfonamide because of the isoenergetic nature of the sulfonamide and acetonitrile bound species. Since no additional stabilization interaction occurs through the binding of the sulfonamide, the C–C reductive elimination barrier (which is identical for all palladium complexes as it was found to occur from the penta-coordinate intermediate **16**) is competitive with the C–N reductive elimination barrier. The C–C reductive elimination barrier was recalculated in the absence of sulfonamide to improve upon the solvent cavitation (no explicit interaction between the sulfonamide and palladium complex was found prior or during the transition state for C–C reductive elimination). This value, obtained prior to confirmation by experiment, was found to be in close agreement to the experimentally measured 23.3 kcal mol^{-1}.

Structures **17** and **18** are referenced to penta-coordinate **16**.

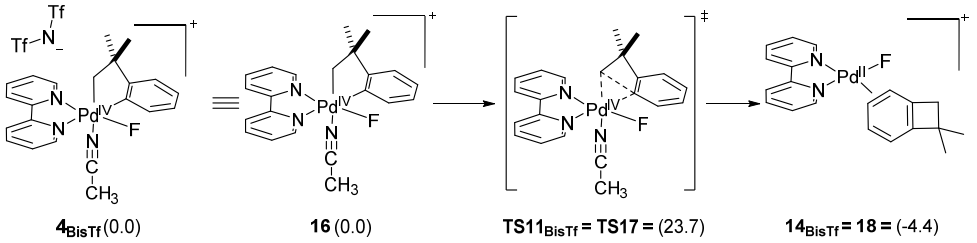

Figure A.13. Summary of C(sp^3)–C(sp^2) reductive elimination from penta-coordinate palladium complex.

Detailed Analysis of Isomerization

During isomerization, the inclusion of explicit acetonitrile is important in the steps involving dissociation of the sulfonamide anion. The following energy diagrams provide a comparison of the energy change from inclusion or absence of explicit acetonitrile. For all cases the energies in the figure are relative to the indicated **1_{Ms}-a_withCH_3CN** or **1_{Ms}-a** (no explicit acetonitrile in the calculation), shown in the title of each figure.

(a) Lowest Energy Pathways

(a) with explicit acetonitrile. (energies relative to **1_{Ms}-a_withCH_3CN**)

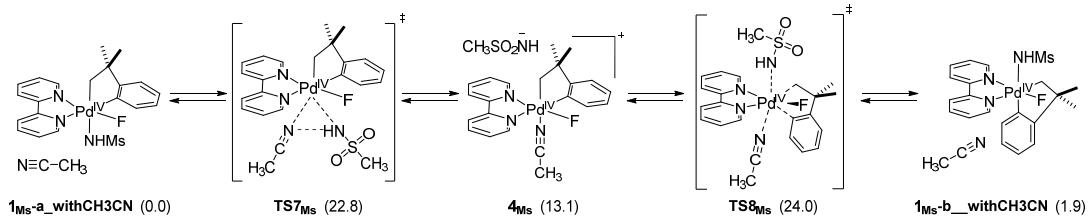

(b) without explicit acetonitrile. (energies relative to **1_{Ms}-a**)

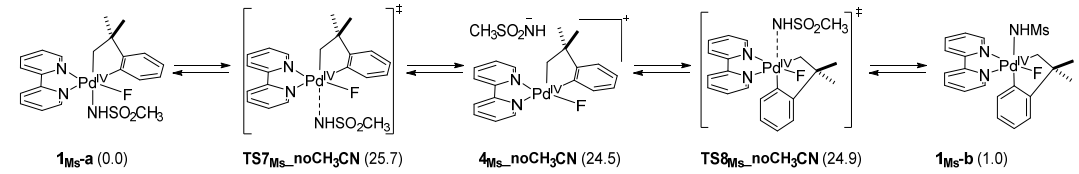

Figure A.14. Isomerization of **1_{Ms}-a** to **1_{Ms}-b (a-b)**

For all cases the energies in the figure are relative to the **1_{Ms}**-a**_withCH_3CN** or **1_{Ms}-a** (no explicit acetonitrile in the calculation). For all cases the energies in the figure are relative to **1_{Ms}**-a**_withCH_3CN** or **1_{Ms}-a** (no explicit acetonitrile in the calculation), as shown in the title of each figure.

(a) with explicit acetonitrile (Elaboration in Figure 6). (energies relative to **1_{Ms}-a_withCH_3CN**)

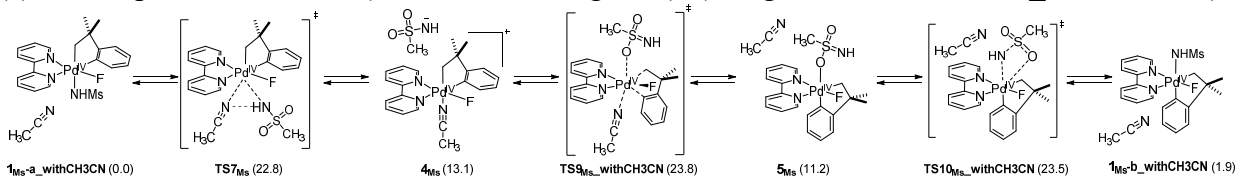

(b) without explicit acetonitrile. (energies relative to **1_{Ms}-a**)

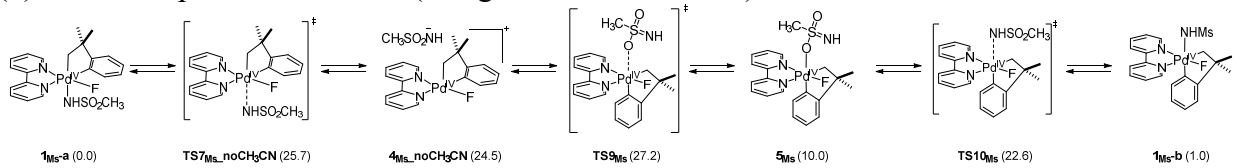

Figure A.15. Isomerization of **1_{Ms}-a to 1_{Ms}-b (a-b)**

(b) High Energy Isomerization Pathways (formation of 1_{Ms}-c through 1_{Ms}-e)

These computational data show that the isomerization processes to form **1_{Ms}-c** and **1_{Ms}-d** share a few elementary steps. In both cases, the first step is the rate determining step. For the comparison between the calculations with and without explicit acetonitrile, only the first step of the isomerization was simulated with explicit acetonitrile since it is rate-limiting. In addition to the isomerization pathways from **1_{Ms}-a**, **1_{Ms}-b** could potentially provide alternative routes to other Palladium(IV) isomers. Pathways under 40 kcal·mol^{-1} originating from **1_{Ms}-b** are outlined below. In summary, pathways leading to 1_{Ms}-c, 1_{Ms}-d, 1_{Ms}-e from 1_{Ms}-b were found to be higher in energy than those originating from **1_{Ms}-a**.

(a) **1_{Ms}-a** to **1_{Ms}-c** and **1_{Ms}-d** without explicit acetonitrile (energies relative to **1_{Ms}-a**)

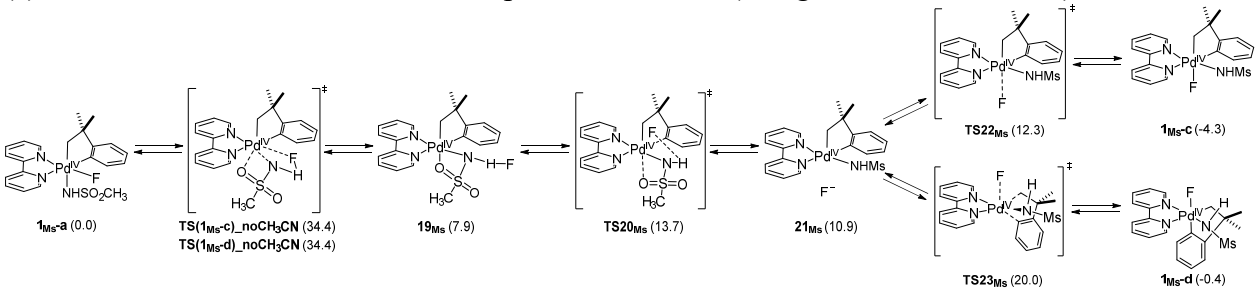

(b) rate limiting step (first step) with explicit acetonitrile (energies relative to **1_{Ms}-a_withCH$_3$CN**)

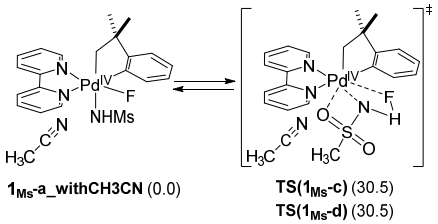

Figure A.16. Isomerization of **1_{Ms}-a** to **1_{Ms}-c** and **1_{Ms}-d (a-b)**

The first step of this process is rate limiting. Calculating the transition state with an explicit acetonitrile interaction with the palladium did not lower the barrier for this process.

(a) **1_{Ms}-a** to **1_{Ms}-e** without explicit acetonitrile (energies relative to **1_{Ms}-a**)

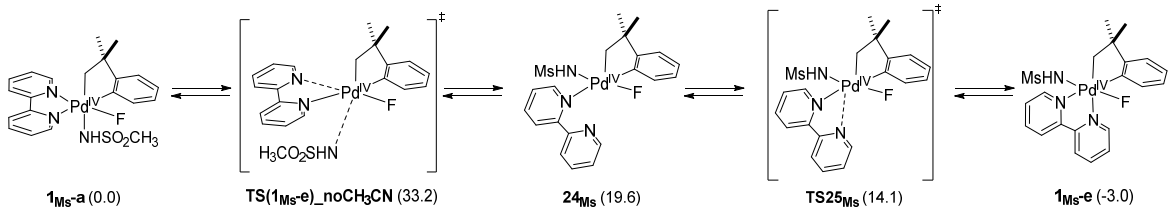

(b) **1_{Ms}-a** to **1_{Ms}-e** with explicit acetonitrile (energies relative to **1_{Ms}-a_withCH$_3$CN**)

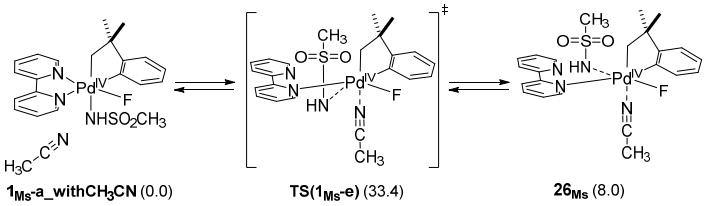

Figure A.17. Isomerization of **1_{Ms}-a** to **1_{Ms}-e (a-b)**

Elaboration on Pathways IV-V

Pathway V

Energies relative to **1_{Ms}-a**. As none of the structures shown in these diagrams are stabilized by explicit binding of acetonitrile to the palladium center, all values in the presence of explicit acetonitrile were found to be high energy.

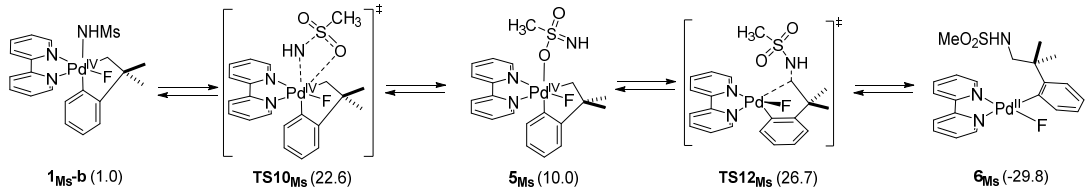

Figure A.18 Summary of results for pathway V

Pathway IV

(a) (energies relative to **1_{Ms}-a_withCH_3CN**)

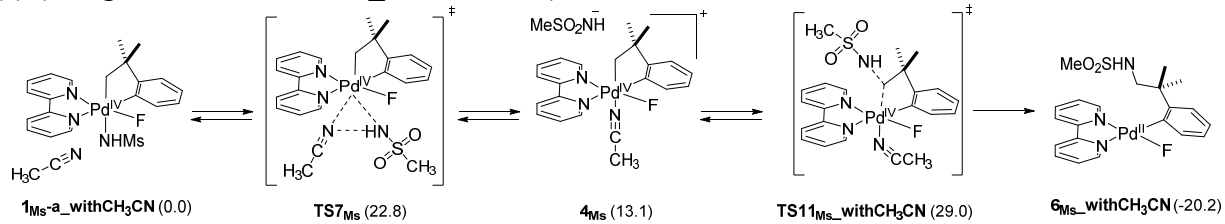

(b) (energies relative to **1_{Ms}-a**)

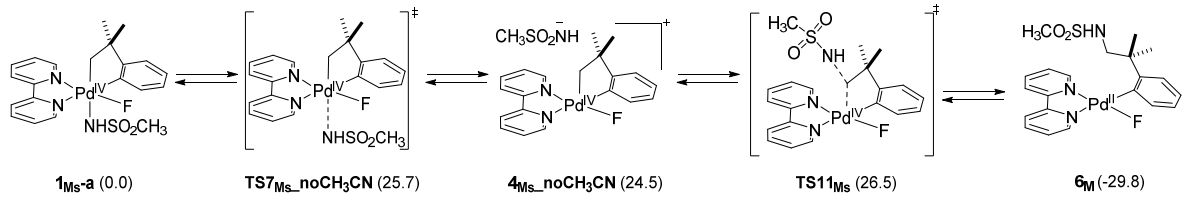

Figure A.19 Summary of results for pathway IV (a-b)

Elaboration on Additional High Energy Steps in Pathways II-III

Pathway III

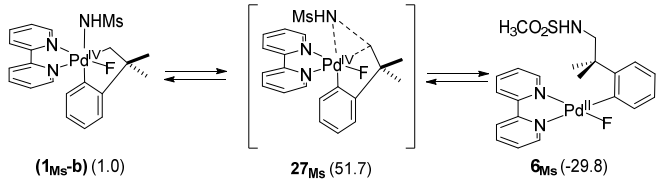

Figure A.20. Direct C-N reductive elimination from **1_{Ms}-b** (energies relative to **1_{Ms}-a**)

Pathway II: Bipyridine dissociation and related substitution steps

(a) Bipyridine dissociation pathways from 1_{Ms}-b

Figure A.21 highlights four pathways related to pathway II of the main text. In total these schemes demonstrate the dissociation of bipyridine from **1_{Ms}-b** does not lead to a viable reaction pathway for reductive elimination. In these cases the explicit acetonitrile only participates when an open coordination site is present on the palladium^{IV} center. In addition to the isomerization pathways from 1_{Ms}-a, 1_{Ms}-b could potentially provide alternative routes to other Palladium(IV) isomers. Pathways under 40 kcal·mol^{-1} originating from 1_{Ms}-b are outlined here. In summary, pathways leading to 1_{Ms}-c, 1_{Ms}-d, 1_{Ms}-e from 1_{Ms}-b were found to be higher in energy than those originating from 1_{Ms}-a.

(a) Bipyridine dissociation and simultaneous migration of sulfonamide to open coordination site. (energies relative to **1_{Ms}-a_withCH_3CN**)

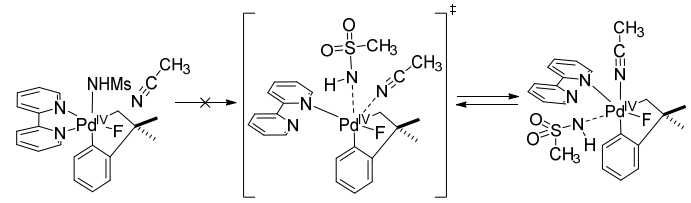

(b) N-O exchange and subsequent high energy partial bipyridine dissociation (energies relative to **1_{Ms}-**a_withCH_3CN)

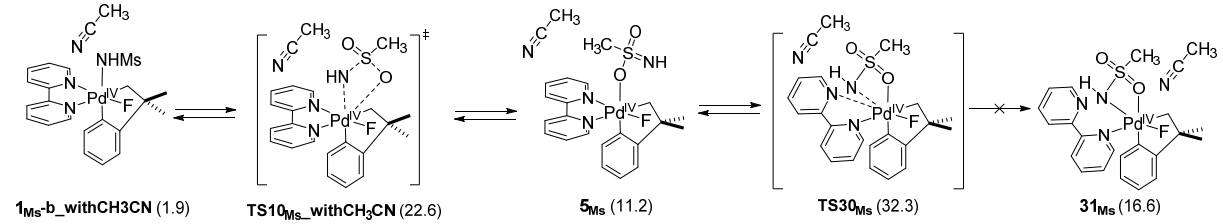

(c) Acetonitrile insertion in place of bipyridine (high energy, bipyridine completely dissociates) (energies relative to **1_{Ms}**-a_withCH_3CN)

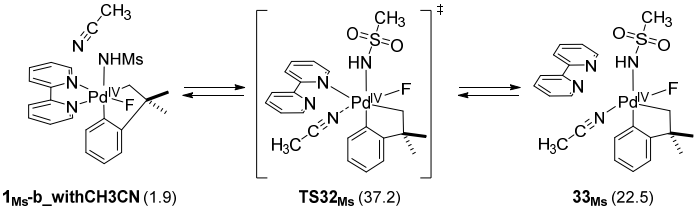

(d) Direct substitution of one arm of bipyridine with acetonitrile (energies relative to **1_{Ms}-a_withCH_3CN**)

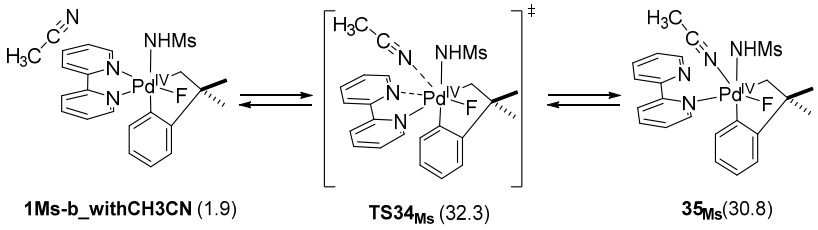

Figure A.21. Comparison of lowest energy pathways for bipyridine dissociation (a-d)

Additional High Energy Pathways

(a) Bipyridine dissociation pathways from $\mathbf{1_{Ms}}$-a

Reactions in this section offer possible alternative routes to bipyridine substitution and dissociation leading to the formation of various intermediates.

The first step of most of these process are higher energy than reductive elimination. Notably, **Figure A.22.a** has a comparable barrier to C-N reductive elimination, but produces a high energy reversible intermediate. The subsequent intermediate $\mathbf{37_{Ms}}$ is unable to undergo C-N reductive elimination as the sulfonamide is still bound. No further calculations were run to investigate additional substitution reactions from this intermediate.

Figure A.22.b and **Figure A.22.c** show high barrier substitution reactions where acetonitrile inserts in place of one arm of the bipyridine ligand. In both cases the intermediate is high energy and the barrier is too high for consideration in additional reactivity.

(a) Partial substitution of bipyridine with acetonitrile (energies relative to $\mathbf{1_{Ms}}$**-a_withCH$_3$CN**)

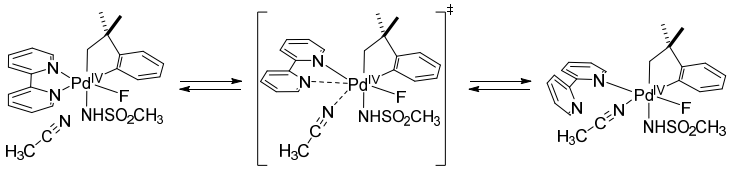

(b) Substitution of bipyridine with sulfonamide, acetonitrile inserts axially (energies relative to $\mathbf{1_{Ms}}$**-a_withCH$_3$CN**)

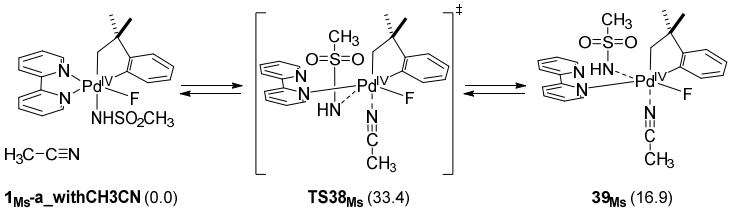

(c) Additional pathway for bipyridine substitution with acetonitrile (energies relative to $\mathbf{1_{Ms}}$**-a_withCH$_3$CN**)

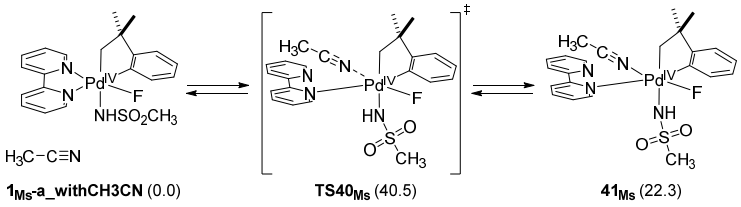

Figure A.22. Bipyridine dissociation from $\mathbf{1_{Ms}}$**-a**: alternatives to Pathways II (a-c)

Additional acetonitrile exchange processes

All additional acetonitrile exchange pathways (not included in the main text and shown here) were found to be high energy in comparison to the lowest barrier pathways determined for isomerization and reductive elimination. We were unable to find a kinetically accessible pathway leading to the (oxygen and nitrogen bound) κ^2 coordination of the sulfonamide with bipyridine dissociation, but instead found an alternative single elementary step involving generation of **53_{Ms}**, a species which has an open equatorial coordination site and the bipyridine was clearly dissociated from the palladium center.

In general, we noted that inclusion of explicit acetonitrile only substantially improved the energetics of a process when the explicit solvent molecule was directly interacting with the Pd complex. In processes where the solvent was a bystander, the energy in the transition state calculation would typically increase. Note that mechanisms presented elsewhere that fall into this category are repeated here for clarity and comparison. The two reaction paths (c-1 and c-2) were generated through analysis of acetonitrile exchange with bipyridine. While the geometries of these two reactions appear quite similar, the reaction energies are different. A closer analysis of the complete reaction path generated by the growing string method shows an additional rotation occurring at the sulfonamide for the case of **$TS46_{Ms}$**. For the sake of completeness, both of these reactions are included.

(a) Insertion of acetonitrile in place of bipyridine (partial dissociation of bipyridine)(energies relative to **1_{Ms}-a_withCH_3CN)**

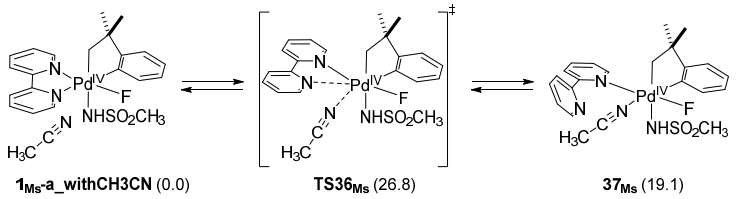

(b) Complete dissociation of bipyridine with κ^2 coordination of sulfonamide (energies relative to **1_{Ms}-a_withCH_3CN)**

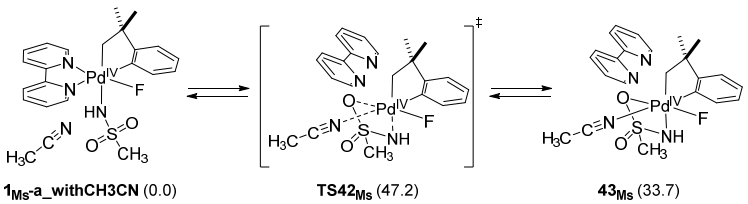

(c) Complete dissociation of bipyridine to generate penta-coordinate Pd^{IV} (energies relative to **1_{Ms}-a_withCH_3CN**)

(c-1)

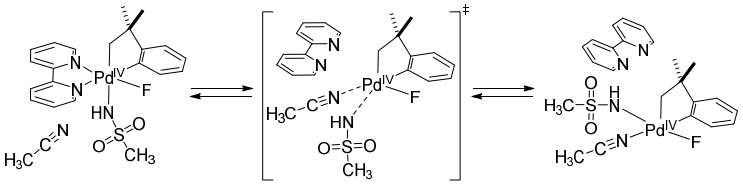

(c-2)

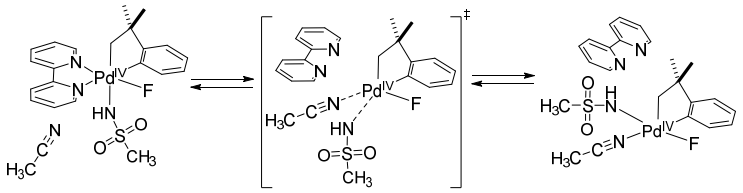

(d) Acetonitrile inserting axially, sulfonamide migration (energies relative to **1_{Ms}-a_withCH_3CN**)

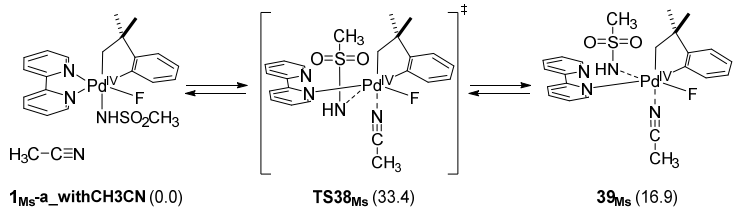

(e) Acetonitrile inserts equatorially in place of bipyridine (energies relative to **1_{Ms}-a_withCH_3CN**)

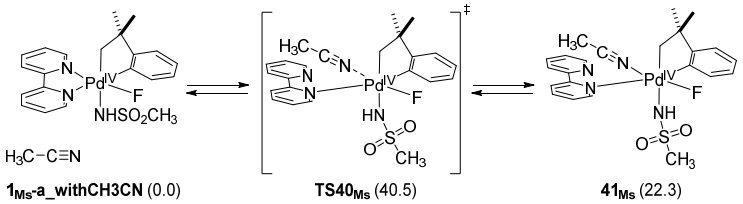

Figure A.23. Additional acetonitrile exchange pathways from **1_{Ms}-a (a-e)**

In addition to the isomerization pathways from 1_{Ms}-a, 1_{Ms}-b could potentially provide alternative routes to other Palladium(IV) isomers. Pathways under 40 kcal·mol^{-1} originating from 1_{Ms}-b are outlined here. In summary, pathways leading to 1_{Ms}-c, 1_{Ms}-d, 1_{Ms}-e from 1_{Ms}-b were found to be higher in energy than those originating from 1_{Ms}-a.

(a) Sulfonamide – acetonitrile exchange (energies relative to **1_{Ms}-a_withCH$_3$CN**)

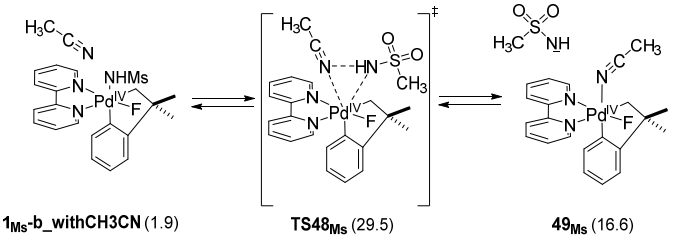

(b) Acetonitrile inserting axially, sulfonamide migration (energies relative to **1_{Ms}-a_withCH$_3$CN**)

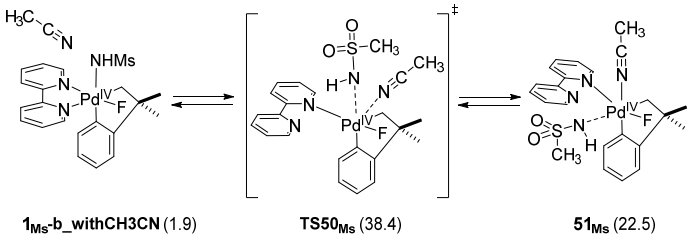

(c) Alternative Transition State: Acetonitrile insertion in place of bipyridine (high energy, bipyridine completely dissociates)

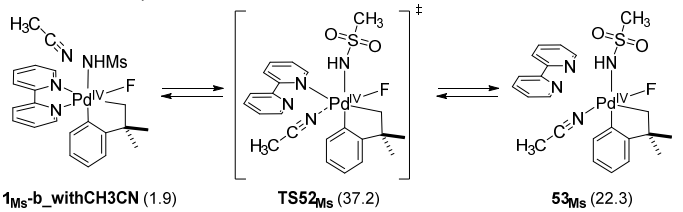

(d) Sulfonamide – acetonitrile exchange from oxygen bound sulfonamide (energies relative to **1_{Ms}-a_withCH$_3$CN**)

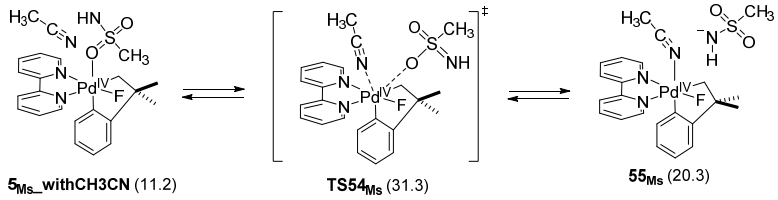

Figure A.24 Pathways from **1_{Ms}-b (a-d)**

References

(1) Pérez-Temprano, M. H.; Racowski, J. M.; Kampf, J. W.; Sanford, M. S. *J. Am. Chem. Soc.* **2014**, *136*, 4097–4100.

(2) (a) Becke, A. D. *Phys. Rev. A* **1988**, *38*, 3098–3100. (b) Becke, A. D. *J. Chem. Phys.* **1993**, *98*, 5648. (c) Lee, C.; Yang, W.; Parr, R. G. *Phys. Rev. B* **1988**, *37*, 785–789.

(3) (a) Hay, P. J.; Wadt, W. R. *J. Chem. Phys.* **1985**, *82*, 299. (b) Hay, P. J.; Wadt, W. R. *J. Chem. Phys.* **1985**, *82*, 270. (c) Hay, P. J.; Wadt, W. R. *J. Chem. Phys.* **1985**, *82*, 270. (d) Wadt, W. R.; Hay, P. J. *J. Chem. Phys.* **1985**, *82*, 284. (e) Dunning, T. H.; Hay, P. J. *Methods of Electronic Structure Theory, Volume 2*; Schaefer, H. F., Ed.; Plenum Publishing Company Limited: New York, 1977.

(4) Shao, Y.; Gan, Z.; Epifanovsky, E.; Gilbert, A. T. B.; Wormit, M.; Kussmann, J.; Lange, A. W.; Behn, A.; Deng, J.; Feng, X.; Ghosh, D.; Goldey, M.; Horn, P. R.; Jacobson, L. D.; Kaliman, I.; Khaliullin, R. Z.; Kuś, T.; Landau, A.; Liu, J.; Proynov, E. I.; Rhee, Y. M.; Richard, R. M.; Rohrdanz, M. A.; Steele, R. P.; Sundstrom, E. J.; Woodcock, H. L.; Zimmerman, P. M.; Zuev, D.; Albrecht, B.; Alguire, E.; Austin, B.; Beran, G. J. O.; Bernard, Y. A.; Berquist, E.; Brandhorst, K.; Bravaya, K. B.; Brown, S. T.; Casanova, D.; Chang, C.-M.; Chen, Y.; Chien, S. H.; Closser, K. D.; Crittenden, D. L.; Diedenhofen, M.; DiStasio, R. A.; Do, H.; Dutoi, A. D.; Edgar, R. G.; Fatehi, S.; Fusti-Molnar, L.; Ghysels, A.; Golubeva-Zadorozhnaya, A.; Gomes, J.; Hanson-Heine, M. W. D.; Harbach, P. H. P.; Hauser, A. W.; Hohenstein, E. G.; Holden, Z. C.; Jagau, T.-C.; Ji, H.; Kaduk, B.; Khistyaev, K.; Kim, J.; Kim, J.; King, R. A.; Klunzinger, P.; Kosenkov, D.; Kowalczyk, T.; Krauter, C. M.; Lao, K. U.; Laurent, A. D.; Lawler, K. V; Levchenko, S. V; Lin, C. Y.; Liu, F.; Livshits, E.; Lochan, R. C.; Luenser, A.; Manohar, P.; Manzer, S. F.; Mao, S.-P.; Mardirossian, N.; Marenich, A. V; Maurer, S. A.; Mayhall, N. J.; Neuscamman, E.; Oana, C. M.; Olivares-Amaya, R.; O'Neill, D. P.; Parkhill, J. A.; Perrine, T. M.; Peverati, R.; Prociuk, A.; Rehn, D. R.; Rosta, E.; Russ, N. J.; Sharada, S. M.; Sharma, S.; Small, D. W.; Sodt, A.; Stein, T.; Stück, D.; Su, Y.-C.; Thom, A. J. W.; Tsuchimochi, T.; Vanovschi, V.; Vogt, L.; Vydrov, O.; Wang, T.; Watson, M. A.; Wenzel, J.; White, A.; Williams, C. F.; Yang, J.; Yeganeh, S.; Yost, S. R.; You, Z.-Q.; Zhang, I. Y.; Zhang, X.; Zhao, Y.; Brooks, B. R.; Chan, G. K. L.; Chipman, D. M.; Cramer, C. J.; Goddard, W. A.; Gordon, M. S.; Hehre, W. J.; Klamt, A.; Schaefer, H. F.; Schmidt, M. W.; Sherrill, C. D.; Truhlar, D. G.; Warshel, A.; Xu, X.; Aspuru-Guzik, A.; Baer, R.; Bell, A. T.; Besley, N. A.; Chai, J.-D.; Dreuw, A.; Dunietz, B. D.; Furlani, T. R.; Gwaltney, S. R.; Hsu, C.-P.; Jung, Y.; Kong, J.; Lambrecht, D. S.; Liang, W.; Ochsenfeld, C.; Rassolov, V. A.; Slipchenko, L. V; Subotnik, J. E.; Van Voorhis, T.; Herbert, J. M.; Krylov, A. I.; Gill, P. M. W.; Head-Gordon, M. *Mol. Phys.* **2015**, *113*, 184–215.

(5) (a) Gordon, M. S.; Schmidt, M. W. *Theory and Applications of Computational Chemistry: The First Forty Years*; Dykstra, C.E., Frenking, G., Kim K. S., Scuseria, G. E., Elsevier, Philadelphia, 2005. (b) Schmidt, M. W.; Baldridge, K. K.; Boatz, J. A.; Elbert, S. T.;

Gordon, M. S.; Jensen, J. H.; Koseki, S.; Matsunaga, N.; Nguyen, K. A.; Su, S.; Windus, T. L.; Dupuis, M.; Montgomery, J. A. *J. Comput. Chem.* **1993**, *14*, 1347–1363.

(6) (a) Cammi, R.; Tomasi, J. *J. Comput. Chem.* **1995**, *16*, 1449–1458. (b) Miertuš, S.; Scrocco, E.; Tomasi, J. *Chem. Phys.* **1981**, *55*, 117–129. (c) Tomasi, J.; Mennucci, B.; Cammi, R. *Chem. Rev.* **2005**, *105*, 2999–3093. (d) Tomasi, J.; Persico, M. *Chem. Rev.* **1994**, *94*, 2027–2094.

(7) Marenich, A. V; Cramer, C. J.; Truhlar, D. G. *J. Phys. Chem. B* **2009**, *113*, 6378–6396.

(8) J.-D. Chai and M. Head-Gordon, *Phys. Chem. Chem. Phys.*, **10** (2008) 6615-20.

(9) (a) Clark, T.; Chandrasekhar, J.; Spitznagel, G. W.; Schleyer, P. V. R. *J. Comput. Chem.* **1983**, *4*, 294–301. (b) Krishnan, R.; Binkley, J. S.; Seeger, R.; Pople, J. A. *J. Chem. Phys.* **1980**, *72*, 650. (c) McLean, A. D.; Chandler, G. S. *J. Chem. Phys.* **1980**, *72*, 5639.

(10) (a) Ehlers, A. W.; Böhme, M.; Dapprich, S.; Gobbi, A.; Höllwarth, A.; Jonas, V.; Köhler, K. F.; Stegmann, R.; Veldkamp, A.; Frenking, G. *Chem. Phys. Lett.* **1993**, *208*, 111–114. (b) Roy, L. E.; Hay, P. J.; Martin, R. L. *J. Chem. Theory Comput.* **2008**, *4*, 1029–1031.

(11) (a) Bonney, K. J.; Schoenebeck, F. *Chem. Soc. Rev.* **2014**, *43*, 6609–6638. (b) Yang, X. *ACS Catal.* **2011**, *1*, 849–854. (c) Jover, J.; Fey, N. *Chem. - An Asian J.* **2014**, *9*, 1714–1723. (d) Cheng, G.-J.; Zhang, X.; Chung, L. W.; Xu, L.; Wu, Y.-D. *J. Am. Chem. Soc.* **2015**, *137*, 1706–1725. (e) Tantillo, D. J. *Angew. Chemie - Int. Ed.* **2009**, *48*, 31–32. (f) Houk, K. N.; Cheong, P. H.-Y. *Nature* **2008**, *455*, 309–313. (g) Kelly, C. P.; Cramer, C. J.; Truhlar, D. G. *J. Phys. Chem. A* **2006**, *110*, 2493–2499.

Appendix B: Supporting Data for Chapter 3

Computational Methods

This work consists of a variety of levels of theory and multiple software packages to perform calculations. An overview of the methods used is provided in **Figure B.1**.

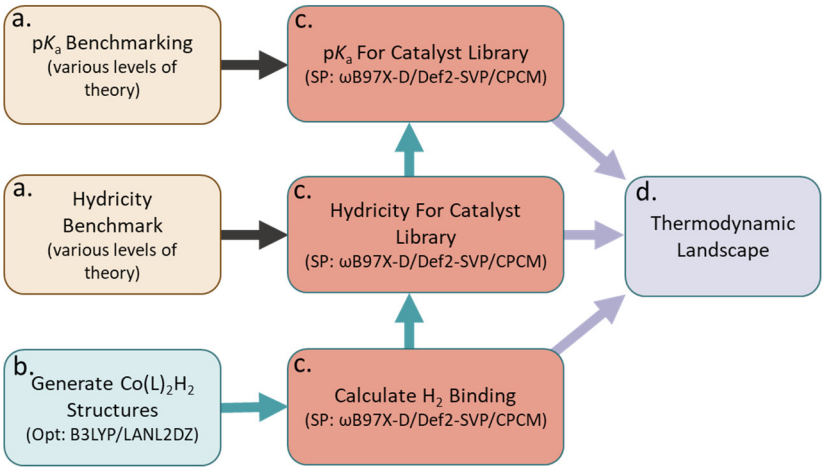

Figure B.1. Overview of this article and relevant methods for each section

Overview: a) Computational benchmark studies to assess performance of basis sets and functionals **b)** Catalyst test set structure generation using B3LYP/LANL2DZ **c)** single point calculations for hydricity, pK_a, and H_2 binding using the optimized ωB97X-D/Def2-SVP/CPCM$_{acetonitrile}$ level of theory **d)** Complete thermodynamic landscape including single point gas phase, ωB97X-D/Def2-SVP and CPCM$_{acetonitrile}$ or SMD-PCM$_{acetonitrile}$ comparisons.

All structures in this study were optimized at the B3LYP[1]/LANL2DZ[2,3] level of theory using the QChem[4] software package. Throughout the benchmark testing (Figure Xa) a variety of different levels of theory were implemented using the Orca[5] software package. Notably, Orca was highly robust, failing in less than 0.05% of all of the single points calculated using only default parameters associated with the indicated level of theory. Single point calculations for the benchmark series were performed using the B3LYP, B3P86, ωB97X-D[6] functionals as well as

DLPNO-CCSD(T)[7] in combination with the LANL2DZ[2,3], Def2-SVP[8], Def2TZVP, ma-Def2-SVP basis sets. Auxiliary basis sets were used as follows: Def2-SVP with Def2/J[9], Def2-TZVP with Def2/J, and ma-Def2-SVP with AutoAux[10]. SMD-PCM[11] and CPCM[12–14] solvation models were implemented through Orca using the default parameters for acetonitrile, dielectric constant = 20.7.

All calculations shown in the thermodynamic landscape and used for quantitative structure activity relationship (QSAR) were performed at the optimized level of theory: ωB97X-D/Def2-SVP/CPCM$_{acetonitrile}$, unless otherwise noted.

Discussion of Benchmark Calculations

Overview of Ligands

The ligands used in the benchmark calculations as well as the construction of the thermodynamic landscape are outlined in figure B.2 below. This figure also outlines the relevant acronyms used throughout discussion of the benchmark studies and assessment of the thermodynamic landscape.

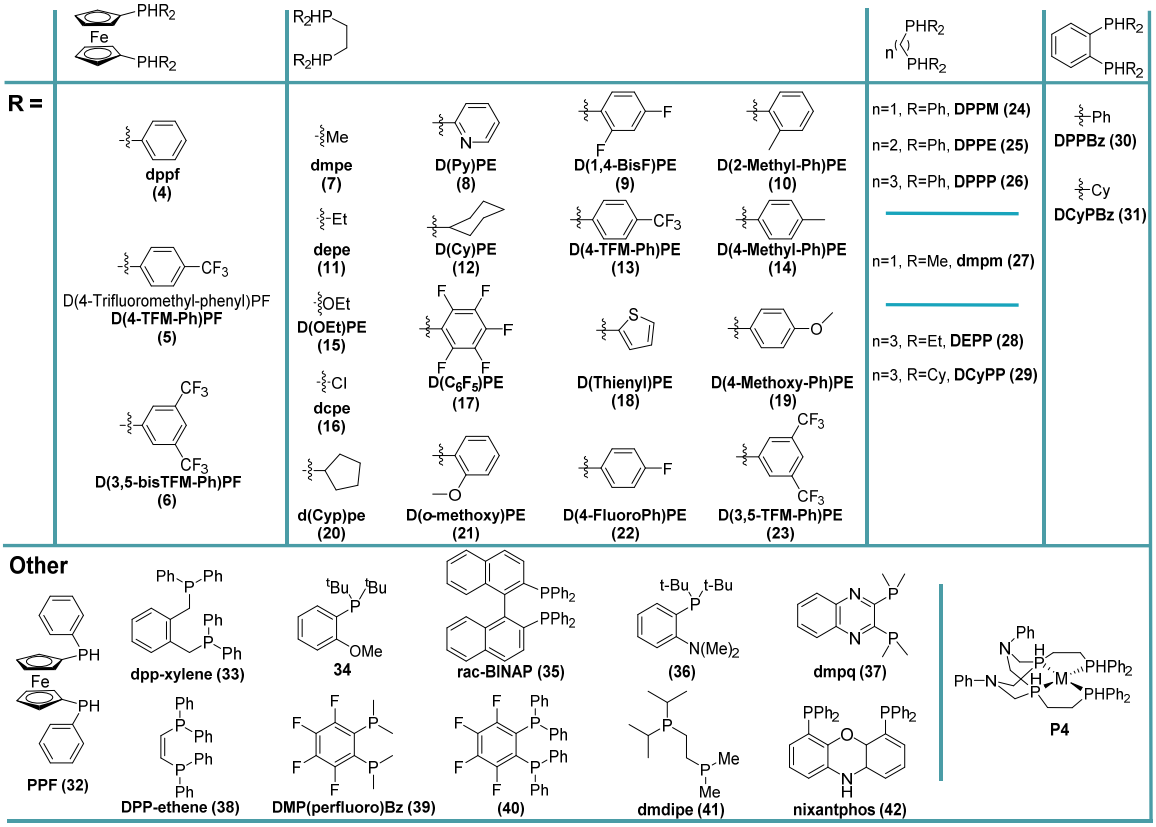

Abbreviations: Et=Ethyl, Ph=Phenyl, Cy=Cyclohexyl,1,1'-Bis(phenylphosphino)ferrocene= **PPF,** 1,2-bis((diphenylphosphanyl)methyl)benzene= **DPPMB,** 2-(2-(di-tert-butylphosphosphanyl)ethyl)pyridine= **D(tBu)PPye,** 2,3-bis(dimethylphosphino)quinoxaline= **DMPQ** 1,2-bis((dimethyl)(diisopropyl)phosphino)ethane= **DMDIPE**

Figure B.2 Overview of ligands used in benchmark calculations and thermodynamic landscape.

Benchmark calculations of M-H pK_a

Guo and coworkers in 2006 reported the most accurate method to date for the calculation of metal pK_a.[15] In their report, the authors demonstrated that geometry optimization at ONIOM(B3P86/LANL2DZ+P:HF /LANL2MB) and subsequent single point calculations at ONIOM(CCSD(T)/LANL2DZ+P:B3P86/LANL2MB) level of theory provided sufficient accuracy for calculation of pK_a. Subsequent studies have also demonstrated that organometallic pK_a values can be accurately calculated using low cost density functional theory approaches.[16–19]

Recent work on smaller organic molecules in aqueous solvent has demonstrated that explicit solvent is sometimes necessary for accurate pK_a calculations.[20–22] However, for transition metal complexes with measured pK_a in acetonitrile the participation of explicit solvent on the metal center is often not the dominant factor in accurate pK_a prediction; with no explicit acetonitrile, accurate pK_a calculations have been demonstrated[15]. Furthermore, metal species targeted for pK_a assessment in this work are strictly octahedral prior to deprotonation and are highly unlikely to coordinate with solvent.

The relative energies of the metal species are sufficient for accurate prediction of M-H pK_a without consideration of the conjugate acid; since in all cases the conjugate acid is equivalent, an exact energy in solution is unnecessary to accurately model the thermodynamic driving force for deprotonation. Using these parameters, we can use a simple, scalable model for pK_a calculation using a single reference compound, similar to work shown by Guo (1), where $\Delta\Delta E$ is the energy difference between the calculated metal complex and an experimentally measured reference complex, R is the universal gas constant in kcal·mol^{-1}·K, and T is the temperature (298 K).

$$\text{Calculated } pK_a = pK_a[NiH(depp)_2]^+ - \frac{\Delta\Delta E}{2.303RT}$$

Equation B.1. Reference calculation for pK_a

For the benchmark set we selected a subset of experimentally reported cobalt and nickel bis(diphosphine) ligated metal complexes across a wide range of pK_a values from -2.3 to 38. The starting M-H complexes and their computational and experimental pK_a values are shown in **Table 1**.

		B3LYP/LANL2DZ			LANL2DZ/SMD-PCM (Acetonitrile)			ωB97X-D/SMD-PCM (Acetonitrile)				ωB97X-D/Def2-SVP	CCSD(T)
Structure	pKa (Exptl)	Gas Phase pK_a	SMD-PCM (Acetonitrile) pK_a	SMD-PCM (Acetonitrile) + Vib. ZPE pK_a	B3LYP pK_a	B3P86 pK_a	wB97X-D pK_a	LANL2DZ pK_a	Def2-SVP pK_a	ma-Def2-SVP pK_a	Def2-TZVP pK_a	PCM (Acetonitrile) pK_a	Def2-SVP/SMD-PCM (Acetonitrile) pKa
$HCo(dppe)_2$	38.0	86.9	36.6	36.0	36.6	35.0	40.4	40.4	37.5	38.7	38.6	43.2	31.9
[*trans*-H_2-Co(P4)]$^+$	31.7	37.6	31.8	31.5	31.8	32.3	34.7	34.7	34.4	35.8	35.8	35.1	36.7
$HNi(dmpp)_2]^+$	24.0	32.0	31.0	29.0	31.0	30.5	33.3	33.3	31.5	31.8	31.5	34.0	30.2
$[HCo(dppe)_2]^+$	23.6	30.6	23.6	23.2	23.6	22.3	24.6	24.6	23.8		25.2	24.6	
*$[HNi(depp)_2]^+$	23.3	23.3	23.3	23.3	23.3	23.3	23.3	23.3	23.3	23.3	23.3	23.3	23.3
$[H_2Co(dppe)_2]^+$	22.8	28.8	22.3	21.8	22.3	22.1	22.1	22.1	22.8	24.3	25.0	23.4	26.7
$[HCo(P4)(CH3CN)]^{+2}$	16.0	-22.5	14.9	24.7	14.9	16.0	14.6	14.6	14.6	16.2	16.4	-29.0	20.5
$[HNi(depp)_2]^{2+}$	-2.3	-61.4	-12.8	-14.4	-12.8	-10.3	-16.0	-16.0	-7.0	-5.6	-4.6	-10.7	-8.0

*Reference compound for pK_a calculations.

Table B.1. Overview of calculated values for pK_a. Red represents the highest values while blue shows the lowest values.

Complexes in Table 1 are ordered from highest to lowest pK_a and were selected to cover a wide range of possible first row transition metal pK_a values. The experimentally determined pK_a values were obtained in acetonitrile and performed using two different experimental protocols. The pK_a values for $[HNi(depp)_2]^+$ (depp=diethylphosphinopropane) (23.3 ± 0.3),[23] $[HNi(dmpp)_2]^+$ (24.0 ± 0.3) (dmpp=dimethylphosphinopropane),[24] and $[H_2Co(dppe)_2]^+$ (22.8 ± 0.2)[25] were measured by equilibration with tetrametylguanidine. Values for $HCo(dppe)_2$,[25] $[H_2Co(dppe)_2]^+$,[25] [*trans*-H_2-Co(**P4**)]$^+$,[18] $[HCo(\mathbf{P4})(CH_3CN)]^{+2}$,[18] and $[Ni(depp)_2]^{2+}$,[23] were determined through analysis of complete thermodynamic cycles analyzing pK_a, $\Delta G°_{H\cdot}$, $\Delta G°_{H^-}$ based on $Co^{II/I}$, $HCo^{III/II}$, and $HCo^{II/I}$ redox couples, or $HNi^{III/II}$, $Ni^{II/I}$, and $Ni^{I/0}$ redox couples, and are associated with and error of ±2 kcal·mol^{-1}, corresponding to approximately ±1.5 pK_a units.

The computational benchmark was designed to test the accuracy of more recently developed functionals, such as ωB97X-D, in comparison to previous computational approaches for pK_a assessment of bis(diphosphine) metal complexes. Recent reports targeting pK_a for organic compounds have shown that ωB97X-D produces consistently low mean absolute error.[26]

Similar to previous findings involving organometallic pK_a, gas phase single point calculations overestimate the energetic difference between various complexes but manage to capture the correct relationship with an R^2 value of 0.9313. SMD-PCM solvation using acetonitrile results in a significantly more precise pK_a, while augmenting the method to incorporate vibrational zero-point energy corrections is deleterious to the correlation between computed and experimental values (**Figure B.3**).

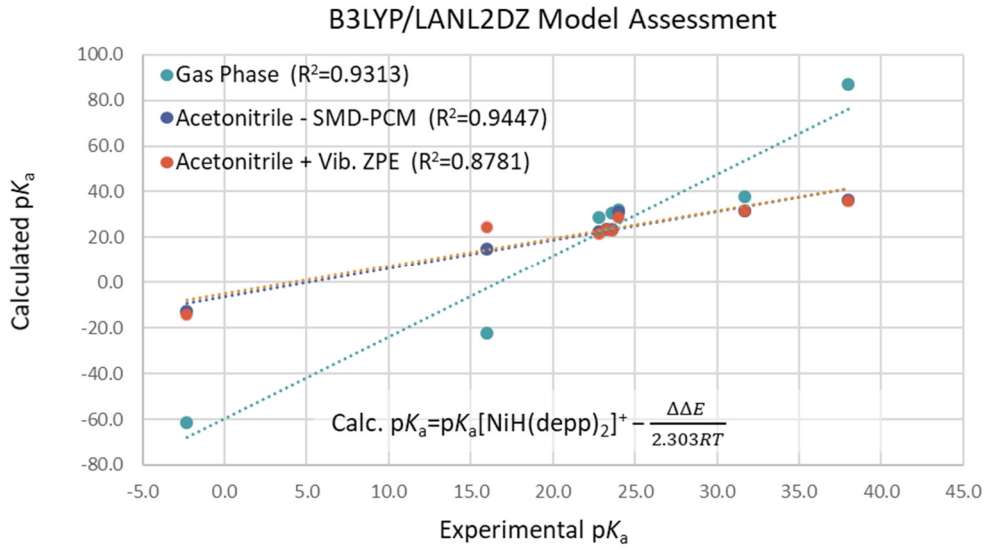

Figure B.3. Comparison of experimental and calculated pK_a values using gas phase, solvation SMD-PCM in acetonitrile, and SMD-PCM(Acetonitrile) plus vibrational zero point energy corrections at the B3LYP/LANL2DZ level of theory

Functional does not seem to have a large impact on the accuracy or precision of the calculation. Modifying the functional for the single point calculation from B3LYP, to B3P86, to wB97X-D results in minimal changes to the overall precision, with the best observed with wB97X-D (Figure B.4).

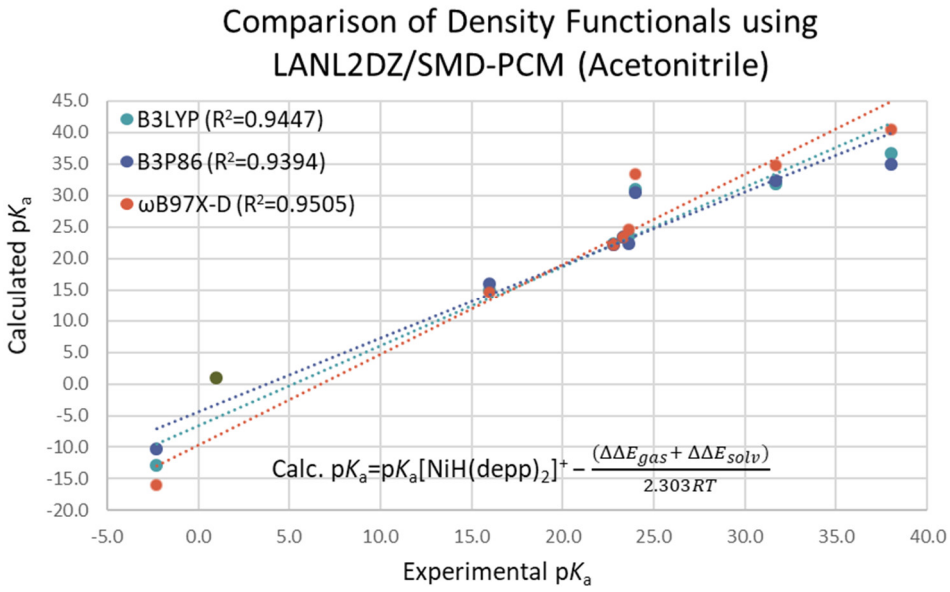

Figure B.4. Comparison of experimental and calculated pK_a values using various functionals in combination with the LANL2DZ basis set and SMD-PCM solvation model with acetonitrile

Basis set choice also has negligible impact on the overall correlation with experiment. More expensive Def2-TZVP basis set marginally improves performance over Def2-SVP, but at significant expense. Minimally augmented Def2-SVP also provides marginal correlation improvement (Figure B.5).

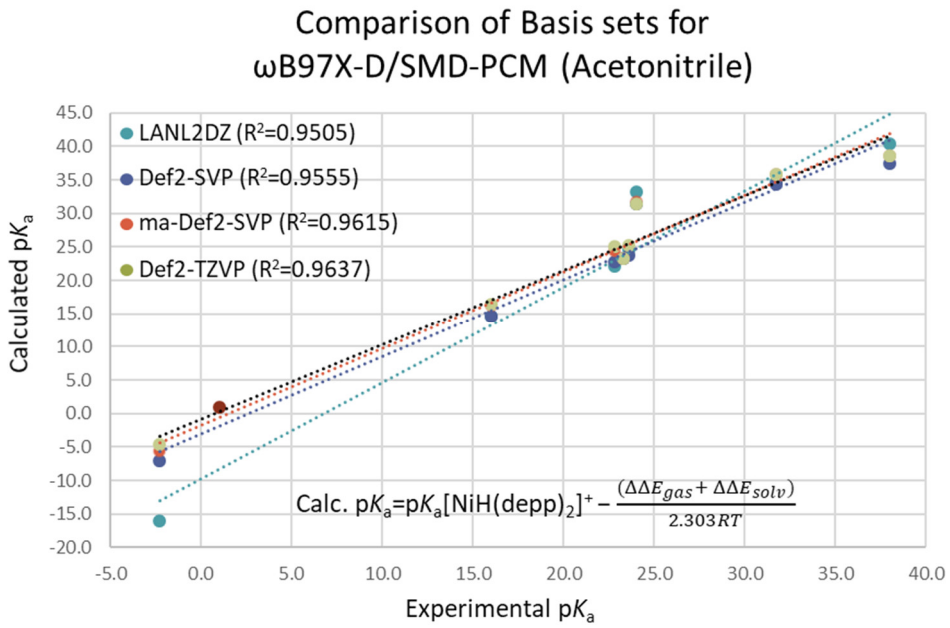

Figure B.5. Comparison of experimental and calculated pK_a values using ωB97X-D functional in combination with the various basis sets and the SMD-PCM solvation model with acetonitrile

Solvent method implementation has a small effect on calculation pK_a, with the SMD-PCM providing an R^2 value of 0.9555 and PCM providing an R^2 of 0.9581, both using acetonitrile.

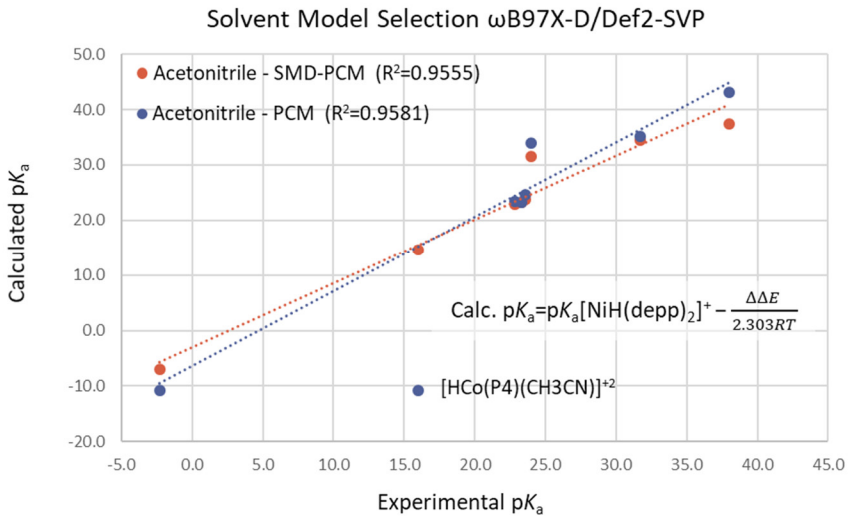

Figure B.6. Experimental and calculated pK_a values using ωB97X-D/Def2-SVP level of theory comparing SMD-PCM and PCM solvation models with acetonitrile

The consistency of results at various levels of theory seems to be the result of systematic error in DFT; comparison of CCSD(T) with wB97X-D results provides very high correlation (Figure B.7).

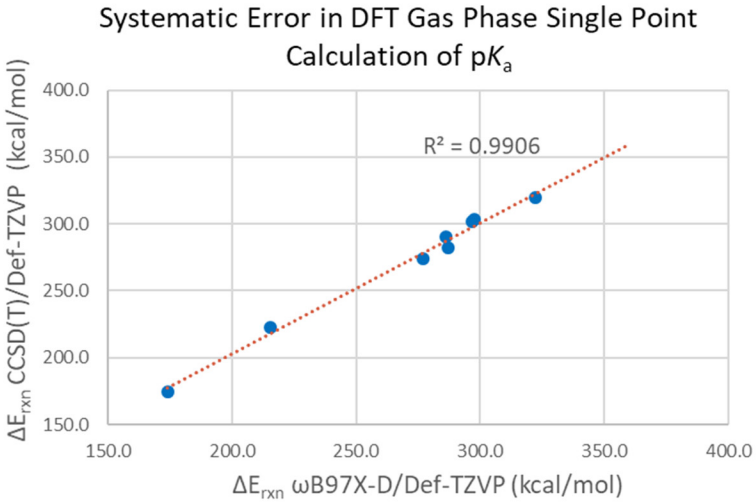

Figure B.7. Comparison of the gas phase relative acidity for the reaction of MH → M at CCSD(T) and ωB97X-D density functionals

These results indicate that using ωB97X-D/Def2-SVP/PCM$_{acetonitrile}$ would provide precise comparisons for calculating test set pK_a values.

Past work has applied linear scaling models to align the pK_a with experimental values, however, for our purposes the relative acidity is more important than absolute acidity as the relative

acidity is all that is needed to interrogate structural features that relate to the thermodynamics of the complexes. For our dataset, we were able to quantitatively reproduce experimental pK_a values by applying an additional linearly scaling model. To find the "corrected" value for pK_a one can multiply the calculated pK_a reported in this document by 1/1.18 or 0.85. We are uncertain as to the reason for the overestimation of absolute pK_a values calculated through DFT.

Benchmark calculations of M-H hydricity

M-H hydricity has been notably more challenging than pK_a calculation. Application of DFT methods for the calculation of $\Delta G°_{H^-}$ has demonstrated poor precision unless constrained to a limited number of benchmark cases. The first entry into calculation of metal hydricity was performed by Kovacs et. al using B3LYP/SDDP for geometry optimization and single points at the B3LYP/SDDP + PCM-UA0 level of theory.[27] The mean absolute deviation was reported to be in the range of 2.4-5.5 kcal·mol^{-1} depending on the substrate. Guo and coworkers visited this problem soon after demonstrating that application of a QMMM ONIOM-CCSD(T) method for pK_a calculation could not be transferred directly to calculating metal hydricity.[28] Instead they resorted to application of B3P86/LANL2DZ+p for geometry optimization adding C-PCM in acetonitrile for single point calculations. Subsequent studies have illustrated that hydride formation is strongly dependent upon solvent choice experimentally, solution pH and other factors including metal solvent interaction in some cases[27–32]. A possible solution to the limited accuracy of DFT based hydricity studies could be the systematic incorporation of explicit acetonitrile onto the pentacoordinate metal hydride. While this might seem a first to be plausible, cobalt species such as $HCo(dmpe)_2$ and $HCo(dppe)_2$ are d^8 metal centers which prefer to adopt a trigonal bipyramidal conformation[25]. Furthermore, for these complexes, the computationally forced incorporation of acetonitrile would result in the lone pairs from the acetonitrile nitrogen contributing to the antibonding d_z^2 orbital of the trigonal bipyramidal species in a thermodynamically reversible, high energy binding regime. The selected benchmark set of first row M-H bis(diphosphine) complexes is shown in table B.2.

All values in kcal·mol-1		B3LYP/LANL2DZ			LANL2DZ/SMD-PCM (Acetonitrile)		wB97X-D/SMD-PCM (Acetonitrile)		ωB97X-D/PCM		CCSD(T)/PCM	
Structure	Hyd. (Exptl)	Gas Phase Hyd.	SMD-PCM (Acetonitrile) Hyd.	SMD-PCM (Acetonitrile) + Vib. ZPE Hyd.	B3P86 Hyd.	wB97X-D Hyd.	Def2-SVP Hyd.	ma-Def2-SVP Hyd.	Def2-SVP Hyd.	Def2-TZVP Hyd.	Def2-SVP Hyd.	Def2-TZVP Hyd.
$[NiH(depp)_2]^+$	66.3	141.5	63.9	56.9	60.5	66.4	63.4	63.9	68.3	68.5	70.0	70.0
$HNi(dmpp)_2]^+$	61.2	148.7	62.7	55.9	59.2	65.2	62.3	63.2	66.9	66.1	66.6	66.6
$HCo(dppe)_2]^+$	60.5	121.2	64.4	56.9	60.0	65.4	56.5	56.9	59.7	60.3		
$HNi(dedpe)_2]^+$	60	124.8	44.5	36.6	39.3	43.2	37.9	37.7	52.6	52.6	51.8	51.8
$[HNi(dmpe)_2]^+$	50.7	142.0	52.6	46.4	48.7	52.4	46.0	47.8	51.2	51.4	52.2	52.2
$HCo(dppe)_2$	49.1	40.3	30.7	22.9	29.5	29.4	29.5	29.4	35.1	35.9	35.0	35.0
$*HCo(dppb)_2]$	48	48.0	48.0	48.0	48.0	48.0	48.0	48.0	48.0	48.0	48.0	48.0
$[HCo(P4)(CH_3CN)]^+$ (trans)	46.7	90.6	36.6	41.4	33.4	28.2	27.6	30.9	31.1	40.0	28.4	
$[HCo(P4)(CH_3CN)]$ (trans)	31.8	24.2	26.8	31.7	23.5	18.8	16.1	20.1	16.5	25.7	15.3	15.3

*Reference compound for hydricity calculations

Table B.2. Overview of calculated values for hydricity. Red represents the highest values while blue shows the lowest values.

Complexes in Table 2 are ordered from highest to lowest hydricity and were selected to cover a wide range of first row transition metal hydricity values ($\Delta G°_{H-}$) ranging from 66.3-31.8 kcal·mol^{-1}. The experimentally determined hydricity values were obtained in acetonitrile using three different experimental protocols.

Hydricity was determined to be 66.3 ± 0.4 kcal·mol^{-1} for $[HNi(depp)_2]^+$ and 50.7 kcal·mol^{-1} (no error reported) for $[HNi(dmpe)_2]^+$.[23,33] These hydricities were calculated from a thermodynamic cycle constructed from direct measurement of metal acidity and heterolytic cleavage of H_2 and solving for the value of $\Delta G°_{H-}$ through equation 2.

$$\Delta G°_{H-} = 2.303RT \log \frac{[HML_2]^+[BH]^+}{[ML_2][H_2][B]} - 2.303RT\ pK_a(BH^+) + 76.0\ \text{kcal/mol}$$

Equation B.2. Overview of experimental derivation of hydricity values for benchmark calculations.

In this equation HML_2 is the metal hydride species, BH^+ is the conjugate acid and the values of 76.0 kcal/mol is obtained from the experimentally measured value for heterolytic H_2 bond cleavage in acetonitrile. The experimental error for this calculation can be attributed to the requisite metal-H and base equilibration and ^{1}H proton NMR measurement error. While no value for hydricity experimental error is reported in the original article, using the error associated with the NMR based pK_a measurement (pKa error approximately ± 0.3) one can extrapolate to an estimated lower bound of the error as ± 0.4 kcal·mol^{-1}.

The second set of complexes were evaluated using a complete thermodynamic cycle based on equation 2 which uses the redox activity of the metal species in place of equilibration with base to probe the hydricity.

$$\Delta G°_{\mathrm{H}-} = 2.303RT\ \mathrm{p}K_a(\mathrm{MH}) + (46.1)[E°(\mathrm{II}/0)] \ + \ 79.6\ \mathrm{kcal/mol}$$

Equation B.3. Overview of second method for experimental derivation of hydricity values for benchmark calculations.

Where the M-H acidity is measured through in situ equilibrium, the value of the II/0 redox couple for Ni species (or III/I for Co) is measured through cyclic voltammetry (CV) multiplied by 23.06*2 to convert from eV to kcal·mol^{-1}, and 79.6 is equal to the free energy change through the reaction: $H^+ + 2e^- \rightarrow H^-$. This approach provides the following experimental hydricities: $[HNi(dmpp)_2]^+$ 62.1,[24] $[HNi(dedpe)_2]^+$ 60.0,[34] $[HCo(dppe)_2]^+$ 60.5,[25] $HCo(dppe)_2$ 49.1,[25] $HCo(dppb)_2$ 48.0,[35] all with the approximate associated error of 0.4 kcal·mol^{-1} and $[H(CH_3CN)Co(P4)]^+$ 46.7,[18] and $H(CH_3CN)Co(P4)$ 31.8,[18] with a reported error of ~2.3 kcal·mol^{-1} from CV measurement.

Figure B.8 demonstrates the stepwise incorporation of model parameters. Addition of SMD-PCM solvation model failed to significantly improve the computational results while incorporation of vibration zero point energy corrections resulted in worse overall performance of the model.

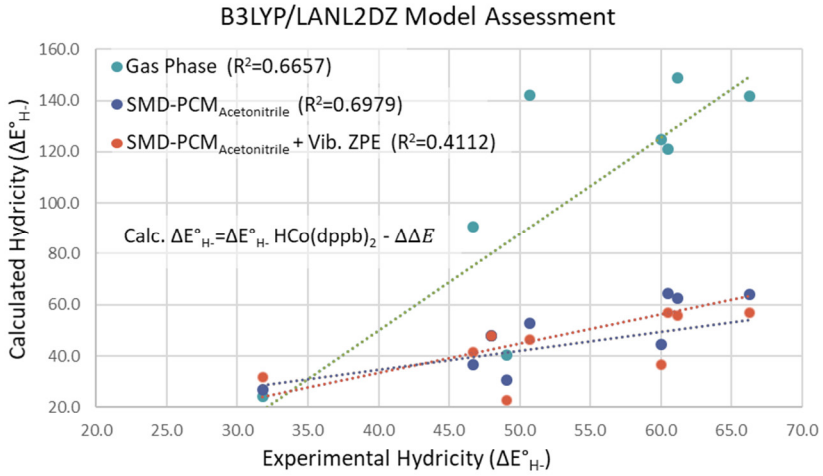

Figure B.8. Comparison of experimental and calculated hydricity values using gas phase, solvation SMD-PCM in acetonitrile, and SMD-PCM$_{\text{acetonitrile}}$ plus vibrational zero point energy corrections at the B3LYP/LANL2DZ level of theory

Density functional selection had little effect on the overall correlation, however ωB97X-D provided the best correlation with experiment (see Figure B.10).

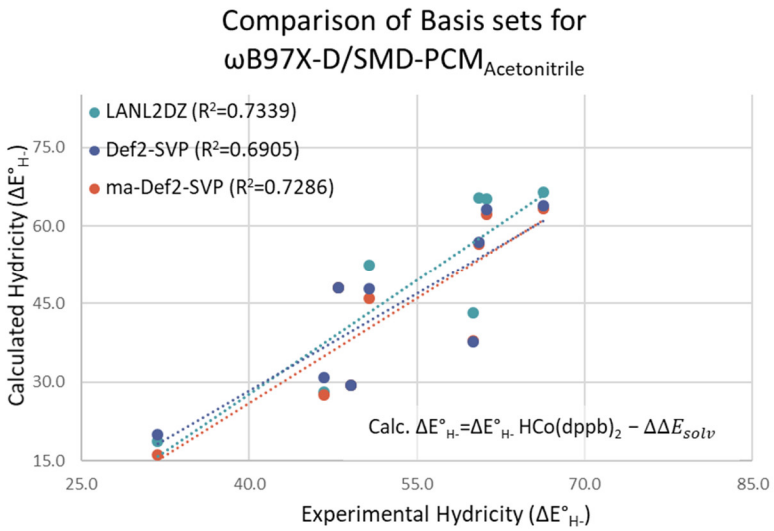

Figure B.9. Comparison of experimental and calculated hydricity values using various functionals in combination with the LANL2DZ basis set and SMD-PCM solvation model with acetonitrile.

Using the ωB97X-D functional SMD-PCM$_{acetonitrile}$ combined with various basis sets provided little improvement in overall correlation. Even though LANL2DZ and Def2-SVP provided similar correlation with experiment, Def2-SVP produced values closer to the expected experimental value with an overall slope closer to the desired1:1 (LANL2DZ=1.55, Def2=1.41).

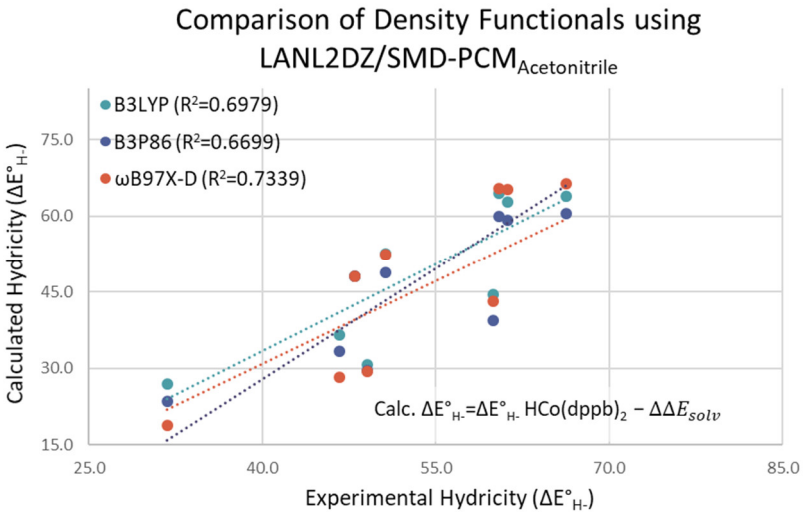

Figure B.10. Comparison of experimental and calculated hydricity values using ωB97X-D functional in combination with the various basis sets and the SMD-PCM solvation model with acetonitrile

Application of the acetonitrile CPCM solvation model improved the consistency of the hydricity value; at a similar level of theory, SMD-PCM was observed to have an R^2=0.7537 while CPCM R^2=0.8850.

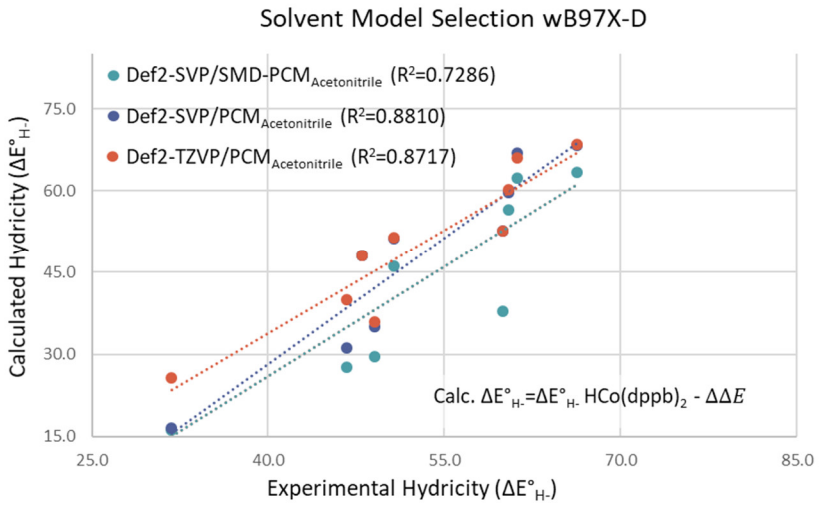

Figure B.11. Experimental and calculated hydricity values using ωB97X-D/Def2-SVP level of theory comparing SMD-PCM $_{acetonitrile}$ and PCM$_{acetonitrile}$

Employing CCSD(T) at either the Def2-SVP or Def2-TZVP basis set using the PCM solvation model failed to improve upon correlation observed in wB97X-D.

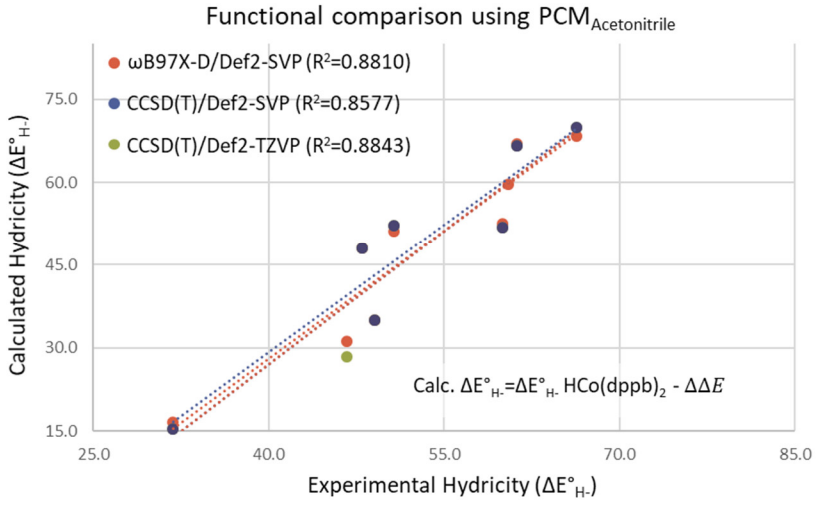

Figure B.12. Experimental and calculated hydricities using ωB97X-D and CCSD(T) with Def2-SVP/PCM$_{acetonitrile}$.

Calculations using more expensive wave function methods also did not significantly improve accuracy. Using CCSD(T)/Def2-TZVP provided a similar level of performance to the ωB97X-D/Def2-SVP level of theory. From these data we decided to use the ωB97X-D/Def2-SVP/$PCM_{acetonitrile}$ level of theory to generate the thermodynamic landscape.

Building the Thermodynamic Landscape

Computational Construction of Catalyst Complexes

Heteroleptic (mixed ligated) octahedral $Co(L)(L')H_2$ species were generated through a step-wise process starting from the homoleptic octahedral $Co(L)_2H_2$ species (Figure X). All bis-ligated structures were optimized at the B3LYP/LANL2DZ level of theory and split into L + H_2LM. The divided structures were re-combined to form all possible combinations. In cases where diastereomers of complexes were generated, the lower energy structure was manually selected. In total, 780 structurally unique complexes were generated and optimized at the B3LYP/LANL2DZ level of theory. Single point energy calculations were then performed using the benchmarked ωB97X-D/Def2-SVP/$PCM_{acetonitrile}$ level of theory. Construction of the catalysts for study in the thermodynamic landscape used a variation of the ZStruct program.[36] This particular ZStruct implementation involved the use of MOPAC[37] for calculation of chemical gradients and a modified single-ended growing string method[38] for combining the divided halves of the catalysts. An overview of this methodology is included in figure B.13.

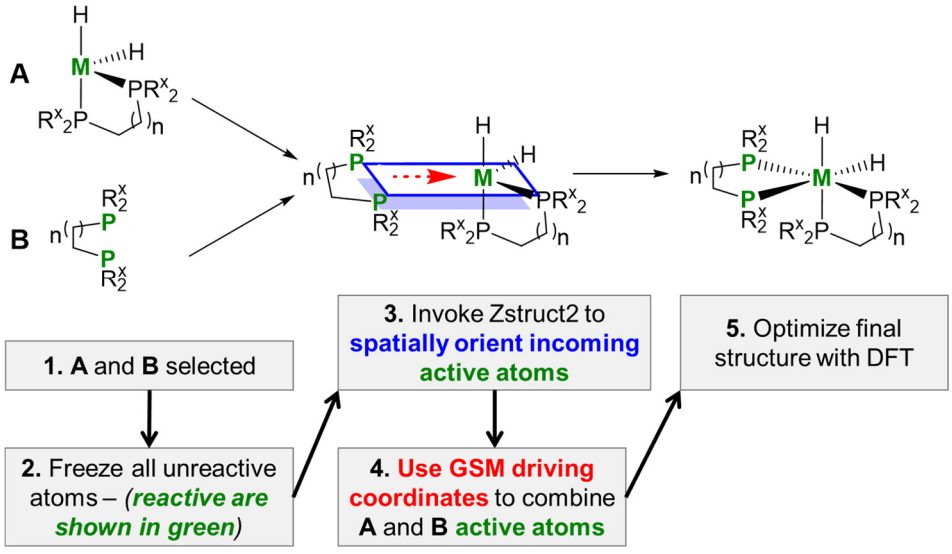

Figure B.13. Overview of catalyst construction using a modified version of ZStruct and the growing string method (GSM) to generate all possible catalyst-ligand combinations.

Though the procedure was generally automated, some complexes proved difficult to construct. Certain ligands tended to fail in construction and optimization more often than others. This method proved reliable for approximately 90% of the catalysts within the desired test set. These include ligands with large aryl groups or sterically encumbered ligand environments including: (in order of frequency): **6-D(3,5-bisTFM-Ph)PF**, **35-rac-BINAP, 36-D(tBu)PPye**, **5-D(4-TFM-Ph)PF**, **31-DCyPBz.** A graphical illustration overviewing instances of failure for constructing, optimizing and/or obtaining single point energies during assessment of H_2 binding is shown in Figure B.14.

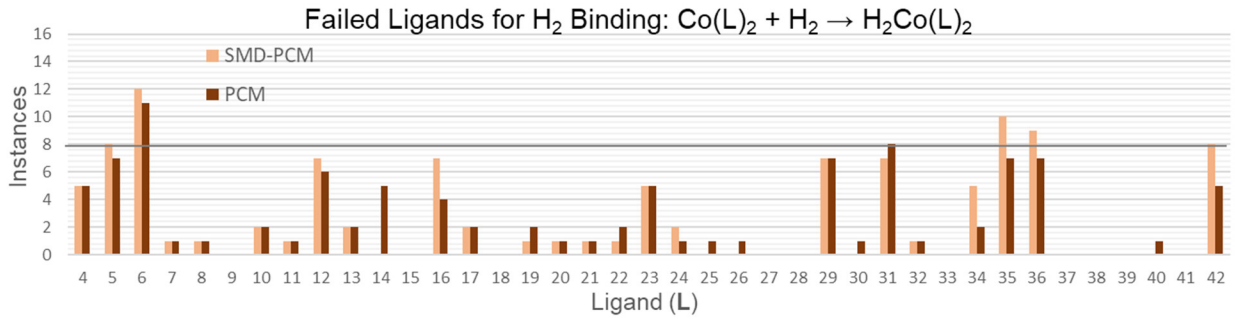

Figure B.14. Instances of failure throughout H_2 binding assessment denoted by ligand label

LASSO Feature Selection

A number of plots are referenced in the main section of the text with regards to more complex models that offer only minimal improvements while substantially increasing the number of terms in the regression. The following section overview these data and presents them for the interested reader.

The 'best' multi-term model developed for the entire landscape is shown in Figure B.15 with an observed $R^2 = 0.72$. The equation for this multi-term model is shown in equation B4, where **BL** is a term for the backbone bond length, features from this model are presented in figure 3.7 of the main text.

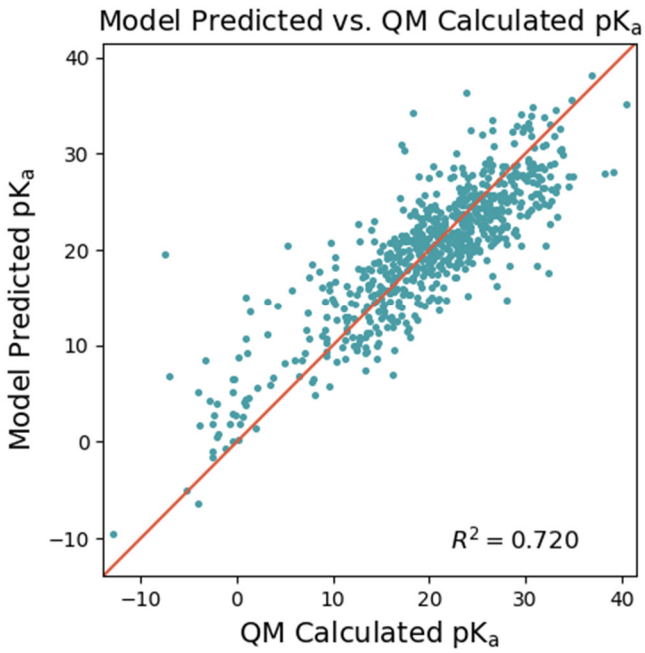

Figure B.15. QM calculated pK_a versus the equation B4 model shown for the full thermodynamic landscape including all complexes.

$$\mathrm{p}K_a = -0.98\mathbf{SVR} - 0.79\mathbf{V_b} - 0.13\mathbf{BT} - 0.37\mathbf{BL} + 0.45\mathbf{L} - 1.03\mathbf{B1} + 1.09\mathbf{B5} - 0.66\mathbf{q_H} - 0.94\boldsymbol{\tau_5} + 6.40\boldsymbol{\epsilon_{NLMO}} + 19.9$$

Equation B4. Multiterm QSAR model describing entire thermodynamic landscape describing pKa

An observed R^2 = 0.63 was the highest observed correlation between QM calculated hydricity and a ten term feature based model shown in Figure B. 16 and represented by equation B5. In both of the regressions the key term was the NLMO energy. Plotting only the NLMO against the pK_a generates a model capable of producing an observed R^2 = 0.642 where SA is the surface area of the ligand, BT is the backbone torsion and BL is the backbone bond length. The remaining features are described in figure 3.7 of the main text.

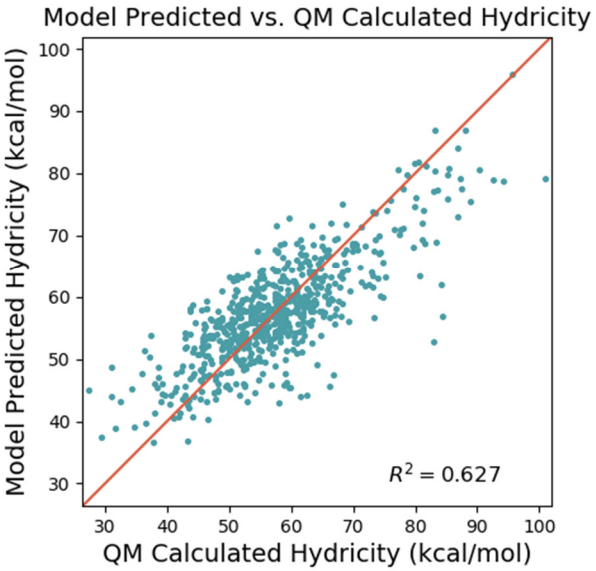

Figure B.16. QM calculated pK_a versus the equation B4 model shown for the full thermodynamic landscape including all complexes.

$$\text{Hydricity} = 2.27\mathbf{SA} + 0.91\mathbf{V_b} - 0.06\mathbf{BT} + 0.68\mathbf{BL} - 1.27\mathbf{L} - 1.75\mathbf{B5} + 0.72\mathbf{q_H} - 0.87\mathbf{q_{Co}} + 2.24\boldsymbol{\tau_5} + 1.14\boldsymbol{l_{Co-H}} - 7.62\boldsymbol{\epsilon_{NLMO}} + 57.4$$

Equation B5. Multiterm QSAR model describing entire thermodynamic landscape targeting hydricity

A plot showing only the pKa versus the NLMO provided an observed R^2 = 0.642 (figure B17, and Equation B6).

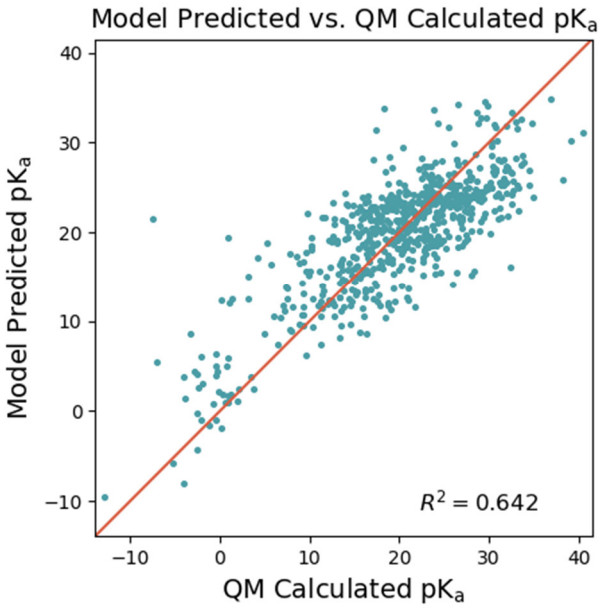

Figure B.17. Single term model shown in equation B5 versus QM calculated pK_a using NLMO

$$pK_a = 6.7\epsilon_{NLMO} + 19.9$$

Equation B6. Single term equation represented by the NLMO describing the thermodynamic landscape.

Similarly, the NLMO for the Co—H bond was the term with the largest coefficient — and thereby largest contribution — in model for hydricity. Plotting a linear regression of NLMO energy versus hydricity provided an observed $R^2 = 0.525$, indicating that a majority of information associated with the multiterm model was provided by the NLMO.

After reducing the landscape to only alkyl, aryl and alkenyl backbones regression models target a feature based description of the landscape were explored. Additionally, we observed that Co—H NLMO energy was strongly correlated pK_a providing an observed $R^2 = 0.64$. These correlations are shown in the main text. These data suggested that the NLMO is the best single feature to describe the relative thermodynamics and that including additional molecular descriptors only marginally improved correlation. For example, including up to 11 terms in the feature based model only provides an observed $R^2 = 0.784$ versus QM calculated pK_a where SA is the surface area of the ligand, V is the volume of the ligand, BT is the backbone torsion and BL is the backbone bond length as shown in Figure B18.

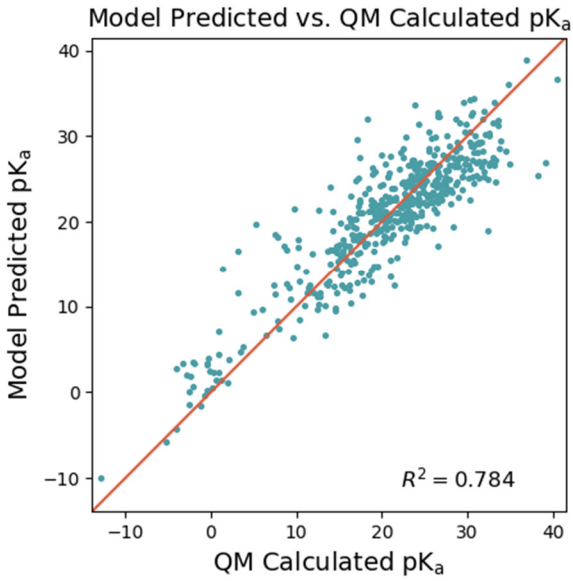

Figure B18. 12 term model shown in Equation B7 versus QM calculated pK_a

$$pK_a = -1.61\mathbf{SA} + 0.\mathbf{27V} - 0.49\mathbf{V_b} + 0.06\mathbf{BL} + 1.00\mathbf{L} - 1.53\mathbf{B1} + 1.00\mathbf{B5} - 3.21\mathbf{q_H} - 0.88\mathbf{q_{Co}} - 0.35\boldsymbol{\tau_5} - 1.49\boldsymbol{l_{Co-H}} + 5.89\boldsymbol{\epsilon_{NLMO}} + 20.9$$

Equation B7. 12 term QSAR model describing reduced thermodynamic landscape targeting pK_a

In the absence of the electronic information provided by Co—H NLMO energy and NBO populations, the models performed significantly worse. The best correlation identified was an eight term model with an observed $R^2 = 0.40$ (Figure B19 and eq. B8).

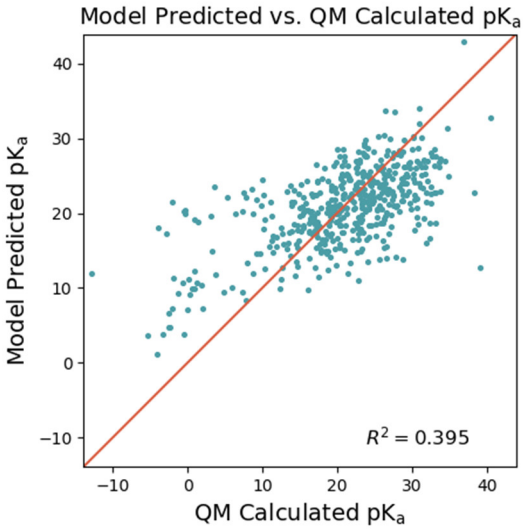

Figure B19. LASSO derived molecular feature model for pK_a versus QM calculated pK_a

The largest terms include the surface-volume ratio of the catalyst complexes, Sterimol parameters *L* and *B1*, distortion parameter Tau 5, and the length of the Co(L)(L')H Co—H bond.

$$\mathrm{p}K_a = 1.79\boldsymbol{V_b} - 6.36\boldsymbol{SVR} + 3.37\boldsymbol{L} + 1.29\boldsymbol{B1} - 0.59\boldsymbol{B5} - 1.28\boldsymbol{\tau_5} - 4.43\boldsymbol{l_{Co-H}} + 20.86$$

Equation B8. Seven term QSAR model in the absence of NBO and NLMO features describing reduced thermodynamic landscape targeting pK_a

As all features are normalized, one can approximate that larger coefficients are associated with a large predictive contribution to variance in pK_a. A reasonable interpretation of larger surface area to volume ratio is a more spherically filled outer ligand sphere is associated with more acid complexes. However, any further interpretation of the model fails to agree with commonly held chemical intuition. For instance, direct interpretation of the bond length of the metal hydride term would counterintuitively suggest that increasing the length of the Co—H bond in Co(L)(L')H is associated with increased acidity. Further analysis quickly reveals the contradictory nature between the molecular features in this model. For instance the buried volume term with a positive coefficient would seem to suggest that increasing the bulk near the metal center is associated with less acidic complexes, a direct contradiction to the surface area to volume ratio term. These poor correlations with more complex models led to the conclusion that the simple metric targeting only NLMO was the most reasonable descriptor for the thermodynamic landscape.

References

(1) Becke, A. D. Density-functional Thermochemistry. III. The Role of Exact Exchange. *J. Chem. Phys.* **1993**, *98* (7), 5648–5652.

(2) Wadt, W. R.; Hay, P. J. Ab Initio Effective Core Potentials for Molecular Calculations. Potentials for Main Group Elements Na to Bi. *J. Chem. Phys.* **1985**, *82* (1), 284–298.

(3) Hay, P. J.; Wadt, W. R. Ab Initio Effective Core Potentials for Molecular Calculations. Potentials for K to Au Including the Outermost Core Orbitals. *J. Chem. Phys.* **1985**, *82* (1), 299–310.

(4) Shao, Y.; Gan, Z.; Epifanovsky, E.; Gilbert, A. T. B.; Wormit, M.; Kussmann, J.; Lange, A. W.; Behn, A.; Deng, J.; Feng, X.; et al. Advances in Molecular Quantum Chemistry Contained in the Q-Chem 4 Program Package. *Mol. Phys.* **2015**, *113* (2), 184–215.

(5) Neese, F. The ORCA Program System. *Wiley Interdiscip. Rev. Comput. Mol. Sci.* **2012**, *2* (1), 73–78.

(6) Chai, J.-D.; Head-Gordon, M. Long-Range Corrected Hybrid Density Functionals with Damped Atom–atom Dispersion Corrections. *Phys. Chem. Chem. Phys.* **2008**, *10* (44), 6615.

(7) Liakos, D. G.; Neese, F. Is It Possible To Obtain Coupled Cluster Quality Energies at near Density Functional Theory Cost? Domain-Based Local Pair Natural Orbital Coupled Cluster vs Modern Density Functional Theory. *J. Chem. Theory Comput.* **2015**, *11* (9), 4054–4063.

(8) Weigend, F.; Ahlrichs, R. Balanced Basis Sets of Split Valence, Triple Zeta Valence and Quadruple Zeta Valence Quality for H to Rn: Design and Assessment of Accuracy. *Phys. Chem. Chem. Phys.* **2005**, *7* (18), 3297.

(9) Weigend, F. Accurate Coulomb-Fitting Basis Sets for H to Rn. *Phys. Chem. Chem. Phys.* **2006**, *8* (9), 1057.

(10) Stoychev, G. L.; Auer, A. A.; Neese, F. Automatic Generation of Auxiliary Basis Sets. *J. Chem. Theory Comput.* **2017**, *13* (2), 554–562.

(11) Marenich, A. V.; Cramer, C. J.; Truhlar, D. G. Universal Solvation Model Based on Solute Electron Density and on a Continuum Model of the Solvent Defined by the Bulk Dielectric Constant and Atomic Surface Tensions. *J. Phys. Chem. B* **2009**, *113* (18), 6378–6396.

(12) Mennucci, B.; Tomasi, J. Continuum Solvation Models: A New Approach to the Problem of Solute's Charge Distribution and Cavity Boundaries. *J. Chem. Phys.* **1997**, *106* (12), 5151–5158.

(13) Barone, V.; Cossi, M. Quantum Calculation of Molecular Energies and Energy Gradients in Solution by a Conductor Solvent Model. *J. Phys. Chem. A* **1998**, *102* (11), 1995–2001.

(14) Cancès, E.; Mennucci, B.; Tomasi, J. A New Integral Equation Formalism for the

Polarizable Continuum Model: Theoretical Background and Applications to Isotropic and Anisotropic Dielectrics. *J. Chem. Phys.* **1997**, *107* (8), 3032–3041.

(15) Qi, X.-J.; Liu, L.; Fu, Y.; Guo, Q.-X. Ab Initio Calculations of P K a Values of Transition-Metal Hydrides in Acetonitrile. *Organometallics* **2006**, *25* (25), 5879–5886.

(16) Chen, S.; Ho, M.-H.; Bullock, R. M.; DuBois, D. L.; Dupuis, M.; Rousseau, R.; Raugei, S. Computing Free Energy Landscapes: Application to Ni-Based Electrocatalysts with Pendant Amines for H 2 Production and Oxidation. *ACS Catal.* **2014**, *4* (1), 229–242.

(17) Morris, R. H. Brønsted–Lowry Acid Strength of Metal Hydride and Dihydrogen Complexes. *Chem. Rev.* **2016**, *116* (15), 8588–8654.

(18) Wiedner, E. S.; Appel, A. M.; DuBois, D. L.; Bullock, R. M. Thermochemical and Mechanistic Studies of Electrocatalytic Hydrogen Production by Cobalt Complexes Containing Pendant Amines. *Inorg. Chem.* **2013**, *52* (24), 14391–14403.

(19) Chen, S.; Raugei, S.; Rousseau, R.; Dupuis, M.; Bullock, R. M. Homogeneous Ni Catalysts for H 2 Oxidation and Production: An Assessment of Theoretical Methods, from Density Functional Theory to Post Hartree−Fock Correlated Wave-Function Theory. *J. Phys. Chem. A* **2010**, *114* (48), 12716–12724.

(20) Cunningham, I. D.; Bhaila, K.; Povey, D. C. Computational Calculation of Absolute Aqueous pKa Values for Phenols. *Comput. Theor. Chem.* **2013**, *1019*, 55–60.

(21) Gupta, K.; Giri, S.; Chattaraj, P. K. Acidity of Meta- and Para-Substituted Aromatic Acids: A Conceptual DFT Study. *New J. Chem.* **2008**, *32* (11), 1945.

(22) Thapa, B.; Schlegel, H. B. Improved P K a Prediction of Substituted Alcohols, Phenols, and Hydroperoxides in Aqueous Medium Using Density Functional Theory and a Cluster-Continuum Solvation Model. *J. Phys. Chem. A* **2017**, *121* (24), 4698–4706.

(23) Curtis, C. J.; Miedaner, A.; Ellis, W. W.; DuBois, D. L. Measurement of the Hydride Donor Abilities of [HM(diphosphine) 2] + Complexes (M = Ni, Pt) by Heterolytic Activation of Hydrogen. *J. Am. Chem. Soc.* **2002**, *124* (9), 1918–1925.

(24) Berning, D. E.; Noll, B. C.; DuBois, D. L. Relative Hydride, Proton, and Hydrogen Atom Transfer Abilities of [HM(diphosphine) 2]PF 6 Complexes (M = Pt, Ni). *J. Am. Chem. Soc.* **1999**, *121* (49), 11432–11447.

(25) Ciancanelli, R.; Noll, B. C.; DuBois, D. L.; DuBois, M. R. Comprehensive Thermodynamic Characterization of the Metal−Hydrogen Bond in a Series of Cobalt-Hydride Complexes. *J. Am. Chem. Soc.* **2002**, *124* (12), 2984–2992.

(26) Matsui, T.; Shigeta, Y.; Morihashi, K. Assessment of Methodology and Chemical Group Dependences in the Calculation of the P K a for Several Chemical Groups. *J. Chem. Theory Comput.* **2017**, acs.jctc.7b00587.

(27) Kovács, G.; Pápai, I. Hydride Donor Abilities of Cationic Transition Metal Hydrides from DFT-PCM Calculations. *Organometallics* **2006**, *25* (4), 820–825.

(28) Qi, X.-J.; Fu, Y.; Liu, L.; Guo, Q.-X. Ab Initio Calculations of Thermodynamic Hydricities of Transition-Metal Hydrides in Acetonitrile. *Organometallics* **2007**, *26* (17), 4197–4203.

(29) Elgrishi, N.; Kurtz, D. A.; Dempsey, J. L. Reaction Parameters Influencing Cobalt Hydride Formation Kinetics: Implications for Benchmarking H 2 -Evolution Catalysts. *J. Am. Chem. Soc.* **2017**, *139* (1), 239–244.

(30) Glezakou, V.-A.; Rousseau, R.; Elbert, S. T.; Franz, J. A. Trends in Homolytic Bond Dissociation Energies of Five- and Six-Coordinate Hydrides of Group 9 Transition Metals: Co, Rh, Ir. *J. Phys. Chem. A* **2017**, acs.jpca.6b11655.

(31) Tsay, C.; Livesay, B. N.; Ruelas, S.; Yang, J. Y. Solvation Effects on Transition Metal Hydricity. *J. Am. Chem. Soc.* **2015**, *137* (44), 14114–14121.

(32) Connelly, S. J.; Wiedner, E. S.; Appel, A. M. Predicting the Reactivity of Hydride Donors in Water: Thermodynamic Constants for Hydrogen. *Dalt. Trans.* **2015**, *44* (13), 5933–5938.

(33) Connelly Robinson, S. J.; Zall, C. M.; Miller, D. L.; Linehan, J. C.; Appel, A. M. Solvent Influence on the Thermodynamics for Hydride Transfer from Bis(diphosphine) Complexes of Nickel. *Dalt. Trans.* **2016**, *45* (24), 10017–10023.

(34) Berning, D. E.; Miedaner, A.; Curtis, C. J.; Noll, B. C.; Rakowski DuBois, M. C.; DuBois, D. L. Free-Energy Relationships between the Proton and Hydride Donor Abilities of [HNi(diphosphine) 2] + Complexes and the Half-Wave Potentials of Their Conjugate Bases. *Organometallics* **2001**, *20* (9), 1832–1839.

(35) Price, A. J.; Ciancanelli, R.; Noll, B. C.; Curtis, C. J.; DuBois, D. L.; DuBois, M. R. HRh(dppb) 2 , a Powerful Hydride Donor. *Organometallics* **2002**, *21* (22), 4833–4839.

(36) Zimmerman, P. M. Automated Discovery of Chemically Reasonable Elementary Reaction Steps. *J. Comput. Chem.* **2013**, *34* (16), 1385–1392.

(37) Stewart, J. J. P. MOPAC2016.

(38) Zimmerman, P. M. Single-Ended Transition State Finding with the Growing String Method. *J. Comput. Chem.* **2015**, *36* (9), 601–611.